Studies on generation and characterization of high current beams from microwave ion source

by

ANURAAG MISRA
(Enrollment No: ENGG04201004001**)**

VARIABLE ENERGY CYCLOTRON CENTRE

Kolkata-700064, India

A thesis submitted to the

Board of Studies in Engineering Sciences

in partial fulfillment of requirements

for the Degree of

DOCTOR OF PHILOSOPHY

of

HOMI BHABHA NATIONAL INSTITUTE

November, 2015

STATEMENT BY AUTHOR

This dissertation has been submitted in partial fulfillment of requirements for an advanced degree at Homi Bhabha National Institute (HBNI) and is deposited in the Library to be made available to borrowers under rules of the HBNI.

Brief quotations from this dissertation are allowable without special permission, provided that accurate acknowledgement of source is made. Requests for permission for extended quotation from or reproduction of this manuscript in whole or in part may be granted by the Competent Authority of HBNI when in his or her judgment the proposed use of the material is in the interests of scholarship. In all other instances, however, permission must be obtained from the author.

ANURAAG MISRA

DECLARATION

I, hereby declare that the investigation presented in the thesis has been carried out by me. The work is original and has not been submitted earlier as a whole or in part for a degree / diploma at this or any other Institution / University.

ANURAAG MISRA

List of Publications arising from the thesis

Journal Publications:-

1. V.S. Pandit, P.Sing.Babu, A. Goswami, S. Srivastava, **A. Misra**, M. Chatterjee, P.Y. Nabhiraj, et.al., "Development of microwave ion source and low energy beam transport system for high current cyclotron", Nucl. Instrum. Methods Phys. Res. B **317**, 434 (2013).
2. **Anuraag Misra** and V.S. Pandit, "Studies on the coupling transformer to improve the performance of microwave ion source", Rev. Sci. Instrum. **85** 063301 (2014).
3. **Anuraag Misra**, A. Goswami, P.Sing. Babu, S. Srivastava and V.S. Pandit, "Studies on space charge neutralization and emittance measurement of beam from microwave ion source", Rev. Sci. Instrum. **86** 113301 (2015).

Conference Publications:-

1. **Anuraag Misra**, V.S. Pandit, G. Pal, H.K. Pandey, "Design and development of a double ridged waveguide for a 2.45 GHz microwave ion source", InPAC-2011 , New Delhi.
2. **Anuraag Misra** , V.S. Pandit and G. Pal, "Design of high current bunching system and fast faraday cup for high current LEBT at VECC ", Proceedings of International Workshop on accelerator-driven subcritical systems and thorium utilization, 2011, Mumbai.
3. V.S. Pandit, G. Pal, S.K. Thakur, P.S. Babu, A. Goswami, M. Chatterjee, R.C. Yadav, S. Srivastava, S. Bhattacharya, S. Roy, C. Nandi and **A. Misra** "Microwave Ion source and injection system for a high current compact cyclotron", Proceedings of International Workshop on accelerator-driven subcritical systems and thorium utilization, 2011, Mumbai.

4. V.S. Pandit, R.C. Yadav, G. Pal, C. Nandi, A. Goswami, P.S. Babu, S. Srivastava, **A. Misra**, "Vaccum system of the ion source and injection line of a high current compact cyclotron.", Journal of Physics Conference Series 11/2012; 390(1): 2066.
5. **Anuraag Misra**, S. Srivastava, V.S. Pandit, "Effect of coupling transformer on the performance of microwave ion source: simulation and experiment", Proceedings of Indian National Particle Accelerator Conference 2013, pp. 317.
6. **Anuraag Misra**, P.Sing. Babu, A. Goswami, S. Srivastava, V.S. Pandit, "Characterization of high intensity beam from 2.45 GHz microwave ion source", Proceedings of Indian National Particle Accelerator Conference 2013, pp. 314.
7. **Anuraag Misra** and V.S. Pandit, "Development of high current microwave feeding system for high current ion source", Proceedings of IEEE Applied Electromagnetics Conference 2013, 978-1-4799-3267-2/13.

ANURAAG MISRA

Dedicated to my parents

COL. (Retd.) *Chandra Nath Misra*

Smt. *Bitan Misra*

ACKNOWLEDGEMENTS

First I would like to express my sincere gratitude to Dr. V.S. Pandit for his valuable guidance, supervision and constant encouragement throughout my thesis work. His broad experience and knowledge of many areas of science were extremely helpful. Working with him was a pleasant and exciting experience.

I would like to sincerely thank Shri C. Mallik (Ex-Head, APG), Dr. P.Y. Nabhiraj, Dr. Alok Chakrabarti and Dr. D.K. Srivastava (Director, VECC, Kolkata) for their continuous support to continue my work.

I express my thanks to Dr. P.Sing Babu and Dr. A. Goswami for many valuable and fruitful discussions we had on the topic of intense beam transport, and the helpful suggestions they offered from time to time. I could not have completed my thesis without the support and encouragement from them.

I tender my grateful thanks to Smt. Mou Chatterjee and Shri Saurabh Srivastava for their help in the data acquisition of the ion source.

I am grateful to Shri G. Pal, Shri C. Nandi, Shri S. Roy, Shri S. Bhattacharya, Shri R.C. Yadav and Shri S.K. Thakur for their assistance during the installation of ion source and beam transport line. Numerous scientific, engineering, technical and office staff members from VECC, Kolkata offered helpful suggestions throughout the course of my thesis work. I thank all of these people for their time and effort.

I am thankful to my wife, Smt. Shweta Misra, for her love and support. Her understanding and care were so important to me in my work and every-day life. I am eternally grateful to my parents and sister for their love and care, for everything what they have done for me in my life.

CONTENTS

Page No.

Synopsis 1

List of Figures 9

List of Tables...12

List of Abbreviations...13

1. Introduction..15

 1.1. Background...15

 1.2. Research motivation..15

 1.3. Contribution of the thesis..18

2. Basics of ion sources and ion beam characteristics...19

 2.1. Plasma physics..20

  2.1.1 Definition of plasma...20

  2.1.2. Density..20

  2.1.3. Electron temperature...21

  2.1.4. Debye length...21

  2.1.5. Plasma oscillations..22

  2.1.6. Ion generation..……...22

  2.1.7. Electron impact ionization...23

  2.1.8. Magnetic confinement...23

 2.2. Waves in plasma..24

  2.2.1. Wave propagation in unmagnetized plasma..24

  2.2.2. Wave propagation in magnetized plasma...25

 2.3. Definition of ion source...26

 2.4. Ion beam formation and transport...27

  2.4.1. Introduction..27

2.4.2. Child-Langmuir law....28

2.4.3. Plasma boundary formulation....29

2.4.4. Beam quality....30

2.4.5. Sigma matrix....32

2.4.6. Statistical beam emittance....32

2.4.7. Emittance of beam from ion source....34

2.5. Ion sources for accelerators....34

2.5.1. Microwave ion sources....35

2.5.1. 1.Working principle....36

2.5.1.2. Microwave ion source components....37

2.6. Summary....39

3. Ion source and low energy beam transport line....40

3.1. Introduction....40

3.2. Description of the 2.45 GHz microwave ion source....41

3.2.1. Plasma chamber and gas feeding system....42

3.2.2. Microwave system....43

3.2.3. Magnetic system....45

3.2.4. Extraction system....46

3.3. Low energy beam transport system....48

3.4. Beam diagnostic elements....49

3.4.1. Faraday cup....49

3.4.2. Beam viewer....51

3.4.3. Direct-current current transformer....52

3.4.4. Water cooled x-y slit....53

3.4.5. Non-interceptive beam profile monitor....54

3.5. Experimental measuremnts....56

3.5.1. Optimization of the operation parameters of ion source....57

3.5.1.1Variation of gas pressure..57

3.5.1.2Variation in drain current..60

3.5.1.3Variation in magnetic field...61

3.5.2. Effect of water addition...62

3.5.3. Effect of different diameter plasma chamber...64

3.6. Summary...66

4. Optimization of microwave coupling in ion source..68

4.1. Introduction...68

4.2. Design and analysis of binomial matching transformer...69

4.2.1. Analytical approach..70

4.3. Optimization with HFSS..74

4.4. Experimental results..80

4.5. Summary...84

5. Space charge compensation and beam emittance measurement..85

5.1. Introduction...85

5.2. Self fields of ion beams..86

5.3. Space charge compensation...89

5.4. Space charge compensation and beam profile measurement......................................90

5.5. Emittance measurement..94

5.6. Simulation..100

5.7. Summary..103

6. Conclusions and future works...104

6.1. Conclusions...104

6.2. Future works..106

Bibliography...108

Synopsis

The Microwave Ion Sources are used to produce intense beams of H^+, D^+ and H_2^+ for various scientific projects such as, spallation neutron sources, accelerator-driven subcritical systems (ADSS), radioactive ion beam production, development of neutrino factory for CP-violation studies etc. These sources offer several advantages in terms of high stability, efficiency, brightness, reproducibility and quite low emittance. The microwave ion sources working with hydrogen gas mainly produces proton and molecular ions like H_2^+, H_3^+ etc. The transport of molecular ions in the beam transport line gives rise to beam halo that severely affects the performance of accelerators with large beam load. These issues make the design of ion source and low energy beam transport (LEBT) very challenging. It becomes essential to characterize and optimize the ion source together with low energy beam transport system to achieve, low transverse emittance at the location of the upstream accelerator and negligible beam halo formation throughout the beam transport line.

At the Variable Energy Cyclotron Centre (VECC) we have taken up a program to develop a 2.45 GHz microwave ion source along with a beam transport system to study the production and transport of proton beam with a current in the range of (10-15) mA and energy of ~100 keV. This beam will be finally used to study the injection and acceleration related issues in a high current compact cyclotron. The present development of high intensity ion source and cyclotron is a part of the larger activity of the Department of Atomic Energy undergoing in the field of high intensity accelerators for Accelerator driven subcritical system (ADSS). The ion source consists of a 2.45 GHz microwave generator, microwave power delivery system, water cooled double walled plasma chamber, a high precision gas flow system, two movable solenoids and their power supplies, triode ion extraction system with adjustable gaps etc., all placed on a high voltage deck floating at ~ 100 kV. At present the ion source is routinely producing ~ 12 mA of beam current with 400 W of microwave power with a maximum proton fraction of ~ 70 %. A well collimated (by 10 mm x 10 mm) beam of ~ 6 mA has been transported to three meters from the ion source using two focusing solenoid magnets. The normalized rms beam emittance of 0.05 mm-mrad is measured for a space charge compensated 75 keV, 5mA proton beam using a non-interceptive beam profile monitor based on a residual gas fluorescence technique.

In this thesis, we describe the optimization results of different ion source components and parameters to improve the performance of microwave ion source. Here, we also present a non-interceptive technique to characterize the high current proton beam and measure its beam emittance under space charge compensation regime.

The organization of thesis is as follows: At first the introduction and motivation for the research is discussed in **Chapter 1**. Thereafter, the basic concepts of plasma physics necessary to understand the key plasma processes taking place in the ion source are introduced in **Chapter 2**. A plasma source becomes an ion source after the ion beam is extracted from the plasma. This extracted ion beam possesses certain properties, which are important for the transport and matching of ion beams to the upstream accelerator. These ion beam properties are also described in this chapter. In **Chapter 3,** a detailed description of Microwave Ion Source at VECC, low energy beam transport line and various diagnostic devices installed in the beam transport line is presented. In addition, results of the experiments to improve the performance of Microwave Ion Source in terms of extracted beam current and proton fraction are also described. The design optimization of matching transformer and its application to achieve improvement in the performance of Microwave Ion Source is described in **Chapter 4**. The experiments related with the characterization of high current proton beam by the point of view of the beam emittance with space charge compensation is described in **Chapter 5**.

Finally, in **Chapter 6**, some general conclusions on the performance improvement of the ion source are given and perspectives for future work are outlined.

The microwave coupling to the plasma plays an important role in the production of high current proton beam from a Microwave Ion Source. The optimum coupling requires matching between waveguide impedance and plasma impedance, as well as a high electric field in the plasma chamber for a given input power. This efficient coupling results in the production of high axial plasma density which finally yields a high current output from the ion source. In this thesis, we outline an analytical method to design a multi-section binomial matching transformer. Using this method, the matching transformers with four sections and different ridged widths were designed and optimized to transform the WR 284 waveguide impedance to the equivalent plasma impedance Z_L. Furthermore, detailed simulations in HFSS were performed to study their characteristics. Simulation results with HFSS indicate that the reflection and transmission coefficients of the matching transformer are more sensitive, particularly to the gap between the ridges as compared to the length and width of the ridges of the last two sections. The simulation results of good impedance match between plasma and waveguide has been confirmed by performing experiments using matching transformers with different ridge widths. A double ridged waveguide matching transformer improves the microwave coupling efficiency and increases the extracted beam current from the ion source by a substantial amount as compared to the WR 284 waveguide under real plasma load conditions. This confirms that high electric field offered by a double ridged waveguide matching transformer is responsible for the high current output from the Microwave Ion Source. Transformers with larger ridge width proved to be advantageous in terms of producing relatively higher electric field and subsequently, yielding more extracted beam current output from the ion source.

A common figure of merit for the performance of high current proton source is the total extracted beam current and proton fraction. Therefore, we conducted several experiments to optimize the operating parameters of the ion source with an objective to reach a high extracted beam current (10 mA - 15 mA) having a proton fraction as high as possible. In these experiments, the parameters like gas pressure, microwave power, magnetic field were varied and the total extracted beam current and proton fraction was recorded as a function of microwave power.

In order to improve the performance of high current proton sources, it is necessary to understand the main factors that influence the plasma density and proton fraction. One of the important factors is the diameter of the plasma chamber. It is a well known fact that radius of the plasma chamber should not be less than the value of the cutoff wavelength λ_c (for TE_{11} mode in the cylindrical cavity) divided by π for the microwave transmission inside the plasma chamber. Considering this criterion, the minimum diameter of plasma chamber should be kept ~ 72 mm corresponding to a microwave frequency of 2.45 GHz. This implies that the plasma cannot be initiated in a plasma chamber with a diameter less than the cutoff value; however, several researchers have already demonstrated that high density plasma can be produced within a plasma chamber of a diameter less than the cutoff value. But the dependence of ion source performance on the plasma chamber diameter is still under investigation. We have performed experiments with the two different aluminium cylinders of inner diameter 35 mm and 45 mm, inserted one at a time into the plasma chamber. The objective of this study was to find out the influence of different diameter aluminium cylinders on the total extracted beam current and proton fraction. For the case of each aluminium cylinder, the total beam intensity as well as the proton fraction was measured. The measurement was done with microwave power upto 200 W. The maximum extracted beam current and proton fraction was obtained for a plasma chamber diameter of 35 mm. There was no measurable beam current for the chamber of 20 mm diameter, which is a signature of microwave cutoff in the plasma.

The main limitation of Microwave Ion Source in getting more beam current is the electromagnetic cutoff, which decides the maximum value of the plasma density which can be reached at a given frequency. In order to increase the electron density beyond this limit the active and passive materials are introduced in the plasma chamber. In the passive technique, a dielectric disc with high secondary electron emission coefficient like Boron nitride (BN) or Alumina disc is located at two extremities of the plasma chamber. Due to high secondary electron emission coefficients of these dielectrics, the electron density in the plasma chamber is enhanced leading to increased dissociative ionizations of the hydrogen atoms and molecules. The secondary electrons can either return towards the central plasma or neutralize the ions near the walls and subsequently reduce the ambipolar electron drain. In both cases they improve the electron density in the ion source.

The proton fraction can also be enhanced by controlling the generation of minority ion species of H_2^+ and H_3^+ by introducing a catalyzing agent into the plasma such that the presence of the agent causes only atomic neutral species of hydrogen to exist in the plasma. To extract pure proton beams, the catalyzing agent is water (H_2O). Essentially this technique involves the addition of catalyzing agents to the ion discharge. Effective catalysts include H_2O, O and SF_6. The most effective being water (H_2O). The addition of small quantities of water (H_2O) to hydrogen plasma will create conditions in the plasma such that essentially only atomic species (H) are present and from which only atomic ionic species (H^+) can be generated and extracted, thus producing pure proton beams.

A series of experiments was carried out to enhance the plasma density and proton fraction in the Microwave Ion Source. First, a 2 mm thick BN disc was fixed on the plasma electrode. The microwave power was changed from 100 W to 200W, at a fixed gas flow. The total extracted beam current was measured using a DCCT (Direct-Current Current Transformer). The beam was transported in the LEBT line with the help of two solenoid magnets and the H^+ was selected out of a mixture of H_2^+ and H_3^+ with a water cooled x-y slit located between the two solenoid magnets. Solenoid field focuses the proton at the x-y slit location, whereas the other ion species get defocused and dumped on the x-y slit jaws. The selected proton beam current was measured by a pneumatically actuated faraday cup located after the water cooled x-y slit. The proton fraction was estimated by taking a ratio of the beam current measured by the faraday cup and DCCT. Finally, the plasma chamber was loaded with some trace amount of water along with the 2 mm BN disc and the previous experiment was repeated.

It is observed from the above experiments that loading the plasma chamber with water along with BN disc provides approximately 30% higher extracted beam current with lower ripple as compared to the case of without water in the plasma chamber.

The transport of low energy intense beam over a long distance is difficult to achieve, due to the presence of space charge effects that can result in beam blow up or deterioration in the beam quality. In addition, these effects also promote the formation of beam halo, which can result in severe degradation of beam quality under large beam load. The most widely used technique to overcome this problem is to exploit the space charge compensation by injecting a heavier gas (typically Ne, Ar, Kr, Xe etc.) in the beam-line. The gas is ionized by the incoming beam. The ejected electrons are trapped in the beam potential, whereas the residual gas ions are repelled in the transverse direction by the beam potential. This phenomenon neutralizes the space charge effect associated with the beam at minimum loss in the beam current.

The transverse beam profile is the main parameter which needs to be measured for beam monitoring, beam quality, beam halo formation prevention and minimization of beam losses. Generally, the interceptive techniques like multi-wires chambers, wire scanner etc. are used for measurement of transverse profiles. However, in the case of high current beams, particularly under continuous beam operation, interceptive monitors such as traditional multi-wire chambers and wire scanners are not preferred due to the destruction of the sensor and associated electronics as well as production of unwanted radiations. Therefore, the non-interceptive diagnostics such as beam induced fluorescence monitor, ionization profile monitor etc. are the only way by which one can characterize the high current beam.

In order to characterize the beam from the Microwave Ion Source, we have installed a diagnostic box in the beam line between the second solenoid and beam dump cum Faraday cup. This diagnostic box contains a pneumatically actuated water cooled alumina plate and a glass viewing window. A precise leak valve is used to introduce neon gas inside the diagnostic box. A CCD camera installed in front of the glass viewing window is used to capture the image of beam induced fluorescence. The captured image is analysed to estimate the rms size of the beam at the location of measurement.

We have measured the profile of 75 keV, 5 mA proton beam by varying the neon gas pressure in the diagnostic box. We recorded the beam induced fluorescence and then beam spot on the water cooled alumina plate using the CCD camera at different settings of gas pressure.

In the measurements with the water cooled alumina plate, there was very little change in the core of the beam, however the beam halo surrounding the core of the beam was found to shrink gradually with the increase in the pressure of the gas upto $3 \cdot 10^{-4}$ mbar. Above this pressure, there was a rapid decrease in the beam current, which may be due to the scattering of beam particles with the gas molecules. Initially we observed a blue color fluorescence, which is a signature of dominant residual gas, nitrogen and hydrogen, in the beam-line.

However, the fluorescence color changed to pink as soon as the neon gas was injected into the beam line.

We have also estimated the emittance of proton beam by varying the gradient of solenoid magnet and acquiring the beam profile with the non-interceptive profile monitor based on residual gas fluorescence. It is well known that this method cannot be directly used in the presence of space charge effect; however, this method is valid for space charge compensated beams because in the case such beams the strength of space charge force becomes negligible. Moreover, as the beam transport and matching will be done to the subsequent accelerator only with space charge compensated beam, it is practical and more important to know the beam emittance under the condition of space charge compensation. The estimation of beam emittance is done using well known sigma matrix method formulation based on thin as well as thick lens approximation of the solenoid magnet. We obtained a normalized rms emittance of 0.05 mm-mrad for a 75 keV, 5 mA proton beam.

List of Figures

2.1. Elementary ion source scheme consisting of plasma source, extraction system and ion beam……………………………………………………………..………………… 28

2.2. Different shapes of plasma boundary…………………………………………… 30

2.3 Beam ellipse……………………………………………...…………………… 31

2.4. Schematic sketch of a Microwave Ion Source..…………………………………… 38

3.1. Layout of the microwave ion source and LEBT…………………………………… 40

3.2. 3D CAD schematic of 2.45 GHz Microwave Ion Source at VECC………………. 41

3.3. 3D CAD schematic of the microwave injection system………………………….. 43

3.4. Photograph of fabricated microwave coupling transformer……………………… 44

3.5. Photograph of the magnetic system of the ion source…………………………..… 45

3.6. The measured axial magnetic field along the axis of the plasma chamber……..… 46

3.7. 3D CAD schematic of triode extraction system…………………………………… 46

3.8. Photograph of the installed Microwave Ion Source at VECC…………………..… 47

3.9. Photograph of the installed low energy beam transport line……………………… 48

3.10. Photograph of the pneuamatically actuated Faraday cup………………………… 50

3.11. Photograph of the Faraday cup cum beam dump………………………………… 51

3.12. Photograph of the water cooled beam viewer……………………………………. 51

3.13. Photograph of the DCCT sensor head mounted on a vacuum chamber…………. 53

3.14. Photograph of the water-cooled x-y slit………………………………….……. 54

3.15. Photograph of the non-interceptive beam profile monitor……………….……. 55

3.16. Variation of extracted beam current and proton fraction η as a function of microwave power at four different gas pressures (in mbar) ………………………….……. 58

3.17. Variation of extraction efficiency η_{ex} as a function of microwave power at four different gas pressures (in mbar) ………………………………………….……..…… 61

3.18. (a) Variation of extracted beam current with the change in I_inj. (b) Variation of extracted beam current with the change in I_ex………………………….…….…… 62

3.19. Variation of extracted beam current and proton fraction as a function of microwave power for the case of water addition in the 90 mm diameter plasma chamber…… 63

3.20. Photograph of aluminium liner inserted into the plasma chamber 1. Plasma chamber, 2. aluminium liner of 45 mm diameter…………………………….……..…….. 64

3.21. Variation of extracted beam current and proton fraction as a function ofmicrowave power for the case of 35 mm and 45 mm inner diameter cylinder…..……..……. 65

4.1. Schematic of the four section matching transformer with its dimensional parameters………………………….…….……………………….…….……. 70

4.2. Equivalent circuit of the matching transformer…..…………………….…….….…. 72

4.3. Comparison of $|S_{11}|$, $|S_{21}|$ and Z_{P2} obtained withanalytical calculations and simulation performed with HFSS for matching transformer with ridge width s = 24 mm.…. 75

4.4. Plots of $|S_{11}|$ and $|S_{21}|$ of matching transformer versus frequency for different ridge widths…………………………….…….……………………….…….…..…. 76

4.5. Variation of the reflection coefficient of the matching transformer with change in the dimension of different parameters by ±1 mm from the design value.…….….…. 77

4.6. A typical electric field profile produced in the plasma chamber by an optimized matching transformer with ridge width s = 48 mm at an input microwave power of 500 W…………………………….…….……………………….…….…..…. 78

4.7. Axial variation of the electric field in the plasma chamber for different ridge widths…………………………….…….……………………….…….…..…. 79

4.8. Variation of the peak electric field E_{pk} at the centre of the plasma chamber and transformed impedance Z_{P2} as a function of ridge width s………….…….……..… 80

4.9. Comparison of measured and simulated $|S_{11}|$ and $|S_{21}|$ of the matching transformer with ridge width s = 24 mm……….…….…………………….…….…..…. 81

4.10. Photograph of Fabricated waveguide and matching transformer. (a) WR 284 waveguide (b) matching transformer with $s = 24$ mm (c) matching transformer with $s = 48$ mm…………………………….…….……………………….…….…..….… 82

4.11. Measured extracted beam current (DCCT) and the reflected power as a function of input microwave power with different transformers. The gas pressure, current in the solenoid coils of the ion source, extraction voltage etc., were kept at the same value during the experiment………………………..……..………………………..……. 83

5.1. Photograph of the LEBT section where non-interceptive beam profile measurement was performed…………………………..……..……………………….…….…..…. 90

5.2. Beam induced fluorescence of 75 keV, 5 mA proton beam : (a) at 4.5×10^{-5} mbar, (b) under neutralized conditions in the presence of Ne gas at 3.0×10^{-4} mbar, and (c) a typical beam spot on water cooled gridded (5mm×5mm) alumina plate..……. 92

5.3. Analysed beam induced fluorescence profiles at two different gas pressures in the beam line………………………..……..……………………….…….…..…. 92

5.4. Profiles of the beam at different residual gas pressure measured with residual gas fluorescence monitor ($2x_{rms}$ represents the rms width of the profile) and the beam spot on the water cooled alumina beam viewer. The grid size is 5mm$\times$5mm………………………..……..……………………….…….…..…. 94

5.5. Variation of the measured $<x^2>$, square of half rms width of the beam profile as a function of the current in the solenoid magnet. The full curves represent the least square fit to the measured data. Here $\tilde{\chi}^2$ represents the reduced chi square value obtained from the fit. (a) Solenoid magnet is considered as a thin lens and distance *L* is measured from the middle of the solenoid of length *l*. (b) Solenoid is considered as hard edge magnet of length *l* and the distance *L* is measured from the end of the solenoid………………………..……..……………………….…….…...…. 98

5.6. Orientation of the beam phase ellipses at the entry of the solenoid and at the profile monitor location for current setting corresponding to waist…….……….…… 99

5.7. Schematic of LEBT indicating the space charge compensation (SCC) region, Viewing port (VP), Faraday cup (FC) and solenoids S1 and S2. Evolution of rms beam envelops at *f* = 0.2 and *f* = 0.8 are also shown………………….…….…….…. 101

5.8. Variation of simulated $< x^2 >$ as function of solenoid current for different *f* values………………………..……..……………………….…….…...…. 102

List of Tables

2.1. The beam fraction enclosed in a given area for Gaussian and uniform distribution. 33

2.2. The specifications of various 2.45 GHz microwave ion sources..................................... 36

4.1. Parameters of the matching transformer for *s* = 24 mm……... 74

5.1. Beam size at different gas pressures……..98

List of Abbreviations

ADSS………………………….…….….……………...Accelerator Driven Subcritical System

LEBT………………………..…….….…………….….….……Low Energy Beam Transport

VECC.….….…………….………….………….……….…...Variable Energy Cyclotron Centre

DCCT….….…………….………….………….……….….…Direct Current Current Transformer

BN…..….…………….………….………….………….………….………….….…Boron Nitride

CCD….….…………….………….………….………….……….….….…...Charge Coupled Device

ESS….….…………….………….………….………….………….……....European Spallation Source

IFMIF….….……………….………….……….…International Fusion Materials Irradiation Facility

MYRHHA….….……….…...Multipurpose Hybrid Research Reactor for High-tech Applications

DAEδALUS….…….…….….…Decay at Rest Experiment for δcp studies At the Laboratory for
….……….…….….……………….………….…….………….…….……….…..Underground Science

ECR…………………………..…….……………………..….……Electron Cyclotron Resonance

UHR……………………….…….….…………………..….…………Upper Hybrid Resonance

SILHI….….………….………….…………………..Source of Light Ions with High Intensities

TRIPS….….…………….………….………….….……..…TRASCO Intense Proton Source

PSI….….………….………….………….……….………….………….……….…Paul Scherr Insititute

PKUNIFTY….……………….……….……….…. .…Peking University Neutron Imaging Facility

VIS….….…………….………….………….………….……….………….……….. Versatile Ion Source

CPHS….….…………….………….………….……….….….. Compact Pulsed Hadron Source

AlN….….…………….………….………….……….……….………….……... Aluminium Nitride

SCCM….….…………….………….………….….….…..Standard Cubic Centimeters per Minute

CAD….….…………….………….………….……………….……….….…..Computer Aided Design

FC….….…………….………….………….……….………….………….…….……….…Faraday Cup

CF….….…………….………….………….……….……….………….……….…..….Conflat Flange

BNC….….……….….…….……….….…..……………….……….….….Bayonet Navy Connector

YAG…….………….…………..……….….……….….….………...Yttrium Aluminium Garnet

ZnS…….……….….……….….….……….….……….….……….…….…...Zinc Sulphide

DC…….……….……….…..…….……….…….…….….……….….……...Direct Current

AC…….……….……….…..…….……….…….……….…….……….…....Alternating Current

MPCT…….………….…….……….….…….………Modular Parametric Current Transformer

DB…….……….……….…..…….……….…….……….……….…….……Distribution Box

TE…….……….……….…..…….……….…….……….……….…….……..Transverse Electric

RFQ…….………….…….……….…….……….…….………Radio Frequency Quadrupole

SCC…….………….…….……….…….……….…….………..…Space Charge Compensation

CW…….……….……….…..…….……….…….……….……….…….……...Continuous Wave

KV…….……….……….…..…….……….…….……….……….….… Kapchinsky Vladimirsky

RGF…….………….…….……….…….……….…….………….…Residual Gas Fluorescence

Chapter 1

Introduction

1.1 Background

The high current beams have been extensively utilized in various areas of science and technology and many new applications are expected in the coming years. The industrial applications includes ion implantation and ion beam lithography for semiconductor device fabrication, food sterilization, industrial polymerization and thin film deposition using focussed ion beam technology. The scientific applications are mainly based on various existing and upcoming research projects like, European Spallation Source (ESS) for neutron based research [1], specially designed neutron generator, IFMIF to provide material irradiation data for fusion experiments [2], DAEδALUS to search CP violation in neutrino oscillations [3,4] and MYRRHA to develop efficient technologies for the realization of an Accelerator Driven Subcritical System (ADSS) [5]. These research projects require H^+, D^+ and H_2^+ ion beams with energies of several hundreds of keV and currents in the range (5-125) mA. Moreover, at the same time, the rms normalized emittance must be kept less than 0.2 mm-mrad at the input of first accelerating section to reduce beam losses.

1.2 Research motivation

To produce high current and low emittance beans as mentioned in Sec 1.1, microwave ion sources have become a popular choice due to its several advantages in terms of low emittance, high microwave efficiency, high reliability, and flexibility to operate in various duty cycles with low maintenance. However, microwave ion sources designed to produce protons also generates a reasonable amount of molecular (H_2^+, H_3^+) ions. The ratio of atomic to molecular ions varies based on the setting of different ion source parameters like, for instance, microwave power, gas pressure, magnetic field profile, plasma chamber diameter etc. Moreover, the molecular ions after being extracted from the ion source contribute only towards the beam loss and can induce degradation of the beam quality leading to a poor performance of the accelerator. This critical issue gave us a strong motivation to perform a study of different ion source parameters which affects the performance of ion source.

Another critical issue in the transport and acceleration of high intensity beams is the space charge associated with the high current beam, which is mainly responsible for the deterioration of beam quality and formation of beam halo, which finally lead to the beam loss. Therefore, the space charge effect must be controlled to avoid transverse emittance growth at the input of upstream accelerator, in our case, a compact cyclotron. Additionally, the profile and emittance of the space charge compensated beam should be measured preferably through non-interceptive methods. As these methods provide the true information about the beam quality degradation if any, this is generally lost in the case of interceptive diagnostics of the beam. These issues motivated us to develop a non-interceptive beam profile monitor with a provision of space charge compensation in the beam line.

At Variable Energy Cyclotron Centre (VECC), a research facility providing a low energy high current proton beam has been developed and commissioned to investigate the physics and technological issues associated with the generation and characterization of intense proton beams. This facility is an R&D effort towards the development of accelerators for accelerator driven subcritical systems program of Department of Atomic Energy [6].

This facility consists of a 2.45 GHz microwave ion source, two solenoid lens based beam transport system, a water cooled x-y slit to reject the undesired ion species in the beam and a non-interceptive beam profile monitor to characterize the space charge compensated high current proton beam. After the characterization of high current beam it will be finally injected into a compact cyclotron through a spiral inflector.

In order to improve the performance of microwave ion source different techniques have been applied to it. As a first step, an optimized matching transformer based on a double ridged waveguide was designed and tested with the ion source. For the design of matching transformer an analytical method is proposed. It is shown that the transmission and reflection characteristics obtained from this approach are in good agreement with the result obtained though finite element codes. The proposed method provides a faster way of estimating the reflection and transmission characteristics as compared to finite element codes. In the experiments with the ion source, it has been demonstrated that optimized matching transformer results into a higher extracted beam current output from the ion source as compared to other coupling transformers and WR 284 waveguide.

For the high current injector the most important parameters are the maximum beam current and the proton fraction. Therefore, the total extracted beam current and the proton fraction was studied as a function of different operating parameters of the ion source like, for instance, microwave power, gas flow rate, magnetic field etc. Next, an experiment was carried out with the ion source by introducing water into the plasma chamber. It resulted into an increment of extracted beam current of ~ 30%. Finally, another experiment was performed with the ion source to study the effect of plasma chamber diameter on the proton fraction and total extracted beam current. It is clearly understood from the experimental results that proton fraction depends on the plasma chamber diameter and reduces in comparison to the case of 90 mm diameter plasma chamber at approximately similar levels of microwave power.

The space charge effect on the beam characteristics is studied through the measurement of profile and emittance of space charge compensated 75 keV, 5 mA proton beam at the end of low energy beam transport line (LEBT). These measurements were performed through a non-interceptive residual gas fluorescence monitor under the influence of a Neon gas injected into the LEBT line. The measured value of beam emittance is quite reasonable and within the requirements of our high current injector cyclotron and for most of the high power proton accelerator projects currently under development or planned in the near future.

1.3 Contribution of the thesis

The novelty of the research work presented in this thesis is the formulation of a unique analytical method for the design of double ridged waveguide based matching transformer and generation of higher extracted beam current from the 2.45 GHz microwave ion source with the usage of optimum matching transformer. This thesis also presents a non-interceptive measurement of profile and emittance of a 75 keV, 5 mA proton beam by exploiting the advantages of space charge compensation through external gas injection into the LEBT line. The uniqueness of this method is that it provides real information about the beam characteristics (profile and emittance) as compared to interceptive methods, where the characteristics of the beam is generally modified by the presence of a conducting slit or aperture.

Chapter 2

Basics of ion sources and ion beam characteristics

The physics of the ion source is mostly based on the fundamental concepts of plasma physics. The correlation of ion source performance with the variation in different plasma parameters requires a detailed understanding of the key elements of plasma physics. In this chapter the basic concepts and terminology of plasma physics relevant to the Microwave Ion Sources are briefly discussed.

The plasma is generated through ionization of the injected gas atoms or solids by the energetic electrons. The energy required to ionize the neutral gas atoms is gained by the electrons through the incident electromagnetic wave into the plasma chamber. The ion beam formation from an ion source takes place due to the extraction of ions from the plasma. A proper ion beam characteristics at the entry of the first accelerating section is required to achieve sufficient beam acceleration together with a high beam transmission through the accelerator. The beam characteristics important for the beam transport and acceleration are discussed in this chapter.

In this chapter, we describe the elements of plasma physics in Sec. 2.1. The wave propagation in plasma is discussed in Sec. 2.2. The definition of ion source is introduced in Sec. 2.3. The ion beam formation and different ion beam parameters are described in Sec. 2.4. A general description about the different ion sources for accelerators with a particular focus on Microwave Ion Sources is described in the Sec. 2.5.

2.1 Plasma Physics

The properties of the ion beam are largely dependent on the different plasma parameters and the design of extraction system. The extracted beam current from the ion source is related to the different plasma parameters, main among them are the density and temperature of the electrons in plasma. Moreover, the extracted beam current is also dependent on the extraction voltage, and configuration of the extraction system. Another ion beam property of utmost importance in the ion source community is the beam emittance, which is mainly dependent on the plasma parameters like ion temperature and density distribution. In this section the key concepts and terminology of plasma physics, generally used in the Microwave Ion Sources, are discussed.

2.1.1 Definition of plasma

Plasma is the fourth state of matter and its composition consists of oppositely charged particles with neutrals. There is a large collection of plasma sources available in the nature, such as ionosphere, solar corona, solar wind etc. However, a large number of man-made plasmas in the form of, neon signs, plasma displays, and fluorescent lamps also exist on the earth. These have become an indispensable part of the modern world. The two main parameters that define plasma are the density and temperature of the particles in the plasma.

2.1.2 Density

The density corresponding to the electrons, ions and neutrals in plasma are defined as n_e, n_i and n_n. The electron density is the key parameter that decides the performance of a plasma based ion source. For ion source plasmas, the typical electron density is in the order of 10^{18} m^{-3}.

2.1.3 Electron temperature

The plasma temperature is a measure of the energy associated with the constituent particles of plasma. Usually, the plasma temperature is defined in units of electron Volts, (eV) , where, 1eV = 11,600 K. Within the plasma, the ion temperature T_i and the electron temperature T_e can have different values. For example, in the case of microwave plasma the ion temperature is in the range of (0.5-1) eV while the electron temperature is in the vicinity of 15 eV. However, in the case of ECR (Electron Cyclotron Resonance) plasma the difference between ion and electron temperature is several hundreds of keV. For the case of plasma in an anisotropic magnetic field, the plasma temperature can have different components ($T_{e\perp}$ and $T_{e\parallel}$) depending on the motion of charged particles with respect to the magnetic field.

2.1.4 Debye length

The fundamental property of plasma is to screen out the externally applied electric fields. This shielding of external electric fields happens in plasma due to the coulomb interaction between the electrons and ions. The high mobility electrons are repelled from neighbouring electrons and get attracted towards the low mobility ions. Due to the distribution of electrons around the ions, the electric fields of ions are cancelled out by the fields of electrons. The distance over which the distribution of electron occurs for the screening of externally applied fields is known as the Debye length, λ_D and is given by:

$$\lambda_D = \sqrt{\frac{\varepsilon_0 k T_e}{n_e e^2}} \,. \tag{2.1}$$

where, ε_0 is the electric permittivity in vacuum, k is the Boltzmann constant, e is the charge of an electron, T_e is the temperature of the electrons, n_e is the density of electrons. The property of quasineutrality is gained by the plasma due to the Debye length effect. Due to the virtue of this property, the plasma limits the distance in which the externally applied electric field can penetrate inside the plasma. The condition of quasineutrality is given by:

$$\sum q_i n_i = n_e \,. \tag{2.2}$$

The main criterion for the plasma to become quasi-neutral is that the $\lambda_D << L_P$, where L_P is the dimension of the plasma. It can be seen from Eq. (2.3) that this condition needs a high enough electron density in the plasma. Alternatively, a large number of particles are required in the Debye sphere. The number of particles N_D inside the Debye sphere is given by:

$$N_D = \frac{4}{3}\pi n_e \lambda_D{}^3 \,. \tag{2.3}$$

A criterion to consider an ionized gas as plasma is $N_D >> 1$.

2.1.5 Plasma oscillations

Numerous modes of oscillations exist in the plasma. The main oscillation is linked with the electron plasma frequency. It is commonly denoted as ω_{pe} and is given by:

$$\omega_{pe}^2 = \frac{e^2 n_e}{\varepsilon_0 m_e} \quad , \tag{2.4}$$

where, m_e is mass of the electron. The frequency of oscillations related with the ions is called ion plasma frequency, which is denoted as ω_{pi} and is given by:

$$\omega_{pi}^2 = \frac{Q^2 e^2 n_i}{\varepsilon_0 m_i}, \tag{2.5}$$

where, Q is the ion charge state and m_i is the mass of ion. Usually the frequency ω_{pe} lies in the microwave range and ω_{pi} in radio frequency range.

2.1.6 Ion generation

There are different ionization processes in which neutrals can be ionized to form plasma. These processes include electron impact ionization, photo-ionization, field-ionization, surface ionization, etc. The electron impact ionization is described in this section as it is the key process which creates the plasma in a microwave ion source.

2.1.7 Electron impact ionization

In the electron impact ionization process [7], the ionization of atoms takes place when an electron gains sufficient energy from the applied electric field and collides with a neutral atom. The ionization of neutral atoms occurs, if the energy of the electron is more than the ionization potential of the neutral atoms, which is the energy required to eject the outermost bound electron to the neutral atom. As a result of ionization, the ions and secondary electrons are created, which can also gain energy from the electric field and ionize the neutral atoms. In addition to the ionization process there is a recombination of ions and electrons which leads to the formation of neutral atoms. Under the equilibrium between these two processes plasma is sustained.

2.1.8 Magnetic confinement

The high temperature plasmas diverge because of the pressure exerted by the plasma particles. In order to confine the plasma an external pressure greater than the pressure of plasma particles is needed. The external pressure is applied to the plasma by inhomogeneous magnetic field generated with electromagnets or permanent magnets. The ions and electrons revolve in a circular orbit perpendicular to the direction of magnetic field, with a cyclotron frequency, which is given by

$$\omega_c = \frac{|q|B}{m_e} \quad , \tag{2.6}$$

where q (= $Q.e$) is the charge of particle and B is the magnetic field.

The velocity of the charged particles remains unchanged in the direction parallel to the magnetic field. As a result, the charged particles follow a helical orbit around the magnetic field lines. The 2.45 GHz microwave ion source described in this thesis, is generally used to produce singly charged ion beams. Therefore, the applied magnetic field does not aim to obtain the electron confinement time of more than 10^{-5} s. However, the presence of magnetic field makes the plasma anisotropic and as a result, the incoming microwave power is efficiently absorbed by the plasma.

2.2 Waves in plasma

The interaction of electromagnetic wave with the plasma is of paramount importance in Microwave and ECR ion sources, as it greatly influences the key characteristics of plasma like electron density and electron temperature. The absorption and reflection of the electromagnetic waves from the plasma depends on the permittivity of plasma, which is again a function of static electric or magnetic fields applied to the plasma. The plasma becomes an anisotropic medium, if an external magnetostatic field is applied to it. This type of plasma is referred to as magnetized, while the one with no magnetic field is called as unmagnetized. Plasmas of Microwave and ECR ion sources are the typical example of anisotropic plasmas. In this section the electromagnetic wave propagation in magnetized and unmagnetized plasmas under cold plasma approximation are briefly described with specific focus on the mechanisms related with the microwave power absorption in Microwave Ion Sources.

2.2.1 Wave propagation in unmagnetized plasma

If the plasma is unmagnetized, then it becomes an isotropic medium with an electric permittivity ε, which is given by the relation

$$\varepsilon = \varepsilon_0 \left(1 - \frac{\omega_{pe}{}^2}{\omega^2} \right) \quad , \tag{2.7}$$

where, ω is the electromagnetic wave frequency. It can be seen from Eq. (2.7) that, for ε to be a positive quantity, the electromagnetic wave frequency ω should be greater than the plasma electron frequency ω_{pe}. As a result the electromagnetic waves are unable to propagate in un-magnetized plasmas with a density above a particular value, known as the critical density (n_c), which is given by

$$n_c = \frac{m\varepsilon}{c^2} \omega_{pe}{}^2 . \tag{2.8}$$

Due to the wave cutoff, the unmagnetized plasmas cannot achieve densities more than n_c. There are two categories of plasmas depending on plasma density. The one with $n_e > n_c$ is called overdense plasma, while the other with $n_e < n_c$ is known as underdense plasma.

2.2.2 Wave propagation in magnetized plasma

If the plasma is magnetized then it becomes an anisotropic medium. As a consequence, the components of the electric permittivity have different values. This means that the propagation of waves in plasma depends on the angle Φ between propagation vector $\vec{k}$ and externally applied magnetic field $\vec{B}_{ex}$. For a particular direction of wave propagation the magnetized plasma supports ordinary and extraordinary waves having different refractive indices. The ordinary wave consists of two types of waves, the L-wave and O-wave. The index of refraction associated with both the waves does not show any resonant behaviour. Furthermore, the ordinary wave is left-hand circularly polarized and it does not transfer energy to the electrons gyrating in the magnetic field. Therefore, the ordinary wave is not of much importance from the point of view of microwave and ECR ion sources. The other type of wave in magnetized plasma is the extraordinary wave that can be classified into R-wave or X-wave depending on the value of Φ. The X-wave propagates in the plasma, if Φ = 90°. The index of refraction n_X associated with X wave is given by the relation :

$$n_X{}^2 = 1 - \frac{\omega_{pe}{}^2}{\omega^2} \frac{\omega^2 - \omega_{pe}{}^2}{\omega^2 - \left(\omega_{pe}{}^2 + \omega_{ce}{}^2\right)} \quad . \tag{2.9}$$

It is quite evident from Eq. (2.9) that X-wave resonates at an angular frequency of $\sqrt{\omega_{pe}{}^2 + \omega_{ce}{}^2}$. This resonance is called as upper hybrid resonance (UHR). These types of resonances are important for the electrostatic wave heating based plasma ion sources. For Φ = 0° the R-wave propagates into the plasma. The refractive index n_R associated with the R wave is given by the relation :

$$n_R{}^2 = 1 - \frac{\omega_{pe}{}^2}{\omega\,(\omega - \omega_{ce})} \quad , \tag{2.10}$$

where, ω_{ce} is the electron cyclotron frequency. The R wave is right-hand circularly polarized. This implies that the R wave electric field rotates in a clockwise manner, which is in the same direction of motion as that of electrons in the magnetic field. At a condition, $\omega = \omega_{ce}$ the index of refraction n_R becomes infinite, which implies a resonance between the wave angular frequency and electron cyclotron frequency. This resonance is called electron cyclotron resonance (ECR). At ECR resonance the direct transfer of energy from electromagnetic wave to the electron occurs and it is the main mechanism for the microwave power absorption in microwave and ECR ion sources.

2.3 Definition of ion source

The injection system of a particle accelerator generally consists of an ion source together with a suitable low energy beam transport system. Over the last few decades several types of ion sources have been developed with an aim to achieve low emittance, high brightness, greater reliability and availability of the extracted beams from the ion source. The majority of the existing ion sources are based on a plasma source.

It is worth pointing out here that sometimes the researchers replace the term "*ion source*" by a "*plasma source*", and vice-versa. However, a plasma source is different than an ion source. In a plasma source the ions are immersed in the plasma and have almost negligible energy as compared to the average thermal energy of the ions. As a consequence, in the plasma source there is no directed drift of ions. However, the ions in an ion source drift in a defined direction because they possess large directed energy by the application of an external electric field in comparison to their average thermal energy. In the ion beam formation process, the ions in a plasma source are extracted by means of an extraction system consisting of multiple electrodes biased to different potentials. The extraction system accelerates the ions which come out from the plasma source and thus an energetic ion beam is formed [8]. Thus an ion source is a combination of a plasma source and an extraction system as shown in figure 2.1.

2.4 Ion beam formation and transport

2.4.1 Introduction

In order to form the ion beam and accelerate a beam extraction system is used which consists of a series of electrodes. The minimum number of electrodes is two (diode system). This includes the plasma electrode, which is in contact with the ion source plasma and has a hole, the extraction aperture, through which the beam can exit the source. The plasma electrode is at the same potential as the source itself.

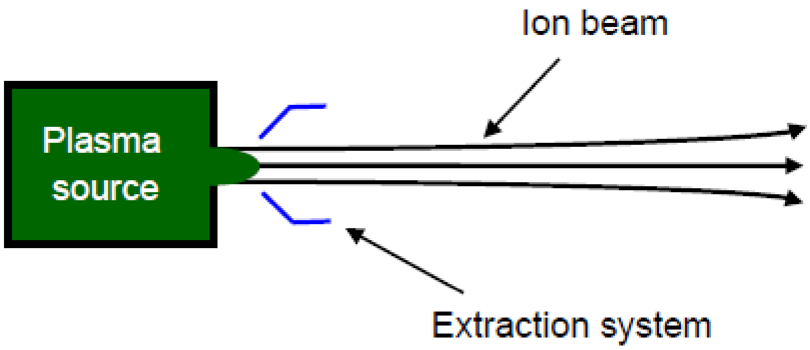

Figure 2.1: A general scheme of ion source consisting of plasma source, extraction system and ion beam.

The next electrode is often referred to as the extraction electrode. The distance between plasma electrode and the extraction electrode is usually called extraction gap. The design of plasma and extraction electrodes are guided by specific required parameters of ion beam like beam diameter, divergence angle etc. In the design of high current ion beam extraction systems, a puller electrode is added in between to the simple two electrode extraction system. The puller is biased to a negative potential with respect to ground. This helps to restrict electrons created at the ground electrode from back-streaming into the ion source. This also provides space charge compensation of the high current ion beam and also improves source stability. The simplest system including such a puller electrode consists of three electrodes and is called accel-decel triode system. More flexible designs with more than three electrodes (tetrode system) and individually adjusted voltages on them are also widely used in the ion source community. A detailed discussion on physics and technology of ion beam extraction is given in [9].

2.4.2 Child-Langmuir law

An ion beam is an ensemble of charged particles. Due to space charge associated with these ions a high enough electric field is generated, which causes the ion beam to diverge.

The maximum ion current density j_{sc} that can be extracted from a planar diode geometry area under space charge limiting conditions is given by the Child-Langmuir law [10, 11].

$$j_{sc} = 1.72\left(\frac{q}{A}\right)^{1/2} \frac{V_{acc}{}^{3/2}}{d_e{}^2} \qquad [\text{ mA/cm}^2\,] \qquad , \tag{2.11}$$

where, V_{acc} denotes the voltage applied between the electrodes of the diode system and d_{e} is the gap between the electrodes. This relation gives an upper limit on the extracted current density as imposed by the space-charge of the beam. It is only valid provided the plasma is able to produce necessary current and the level of vacuum between the electrodes is very good, so that a high enough voltage is applied and sustained between the electrodes. The current density j_{p} that can be delivered by the plasma is given by :

$$j_p = 4.91 \cdot 10^{-13} n_i \left(\frac{q}{A}\right)^{1/2} T_i^{1/2} \qquad [\text{mA/cm}^2] \quad . \tag{2.12}$$

2.4.3 Plasma boundary formation

The surface between the plasma and the vacuum region into which ions are extracted is referred to as the plasma boundary. The plasma boundary plays a vital role in determining the ion beam characteristics. The shape of the plasma boundary depends on various parameters like plasma density, the design of the plasma and extraction electrodes, the diameter of the extraction aperture, and the effective electric field in the extraction region [12]. The shape of the plasma boundary has a deep influence on the quality of the extracted ion beam and is, therefore, very important for the design of ion beam extraction systems. In the ideal case, an ion beam with parallel trajectories can be extracted from a plasma ion source, when the plasma boundary is planar. This happens for the condition $j_{sc} \approx j_p$. For the condition $j_p > j_{sc}$ the plasma boundary is convex resulting into a divergent ion beam.

However, for the condition $j_p < j_{sc}$ the plasma boundary is concave producing a convergent ion beam from the ion source. Figure 2.2 shows the different plasma boundary shapes and their corresponding ion trajectories in the extracted beam.

In the case of microwave ion sources, we have typically $j_p < j_{sc}$ i.e. the space charge limited extractable current is more than the ion generation in the plasma. This condition produces a convergent ion beam. The focal point of the ion beam can be optimized by variation of the electric field between extraction and puller electrode. During the transport of ion beam through a beam line, it will diverge due to its defocusing space charge forces. Therefore, electric and magnetic focusing elements like einzel lenses, solenoid and quadrupole magnets are normally used to transport low energy high current beams to the upstream accelerator.

2.4.4 Beam quality

The efficient beam transport and injection into the upstream accelerator with minimum losses depends on the beam quality from the ion source. In the community of accelerator physics the beam quality is generally defined in terms of beam emittance.

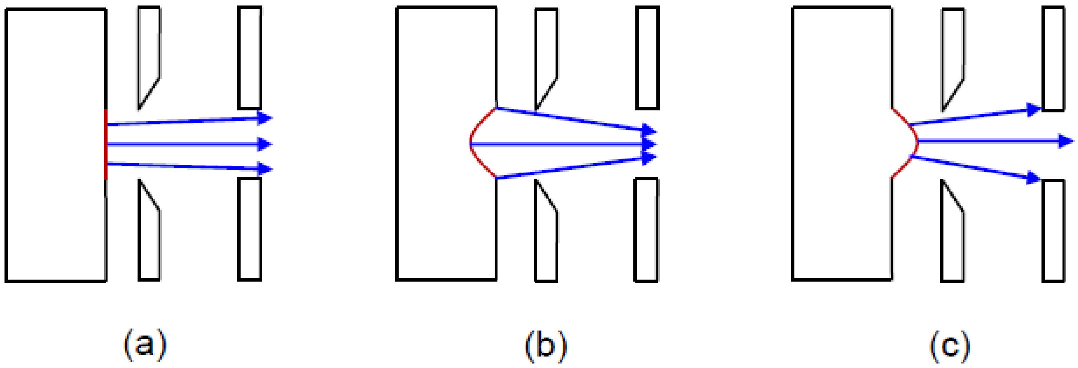

Figure 2.2: Different shapes of plasma boundary

In the theory of beam physics, the particles in a beam are usually represented by a six dimensional phase space (*x-x*', *y-y*', *z-z*'), where *x*, *y*, and *z* are the coordinates of the particle position and *x*', *y*' and *z*' are the corresponding particle angles. According to Liouville's theorem [13], the occupied phase space area remains constant under the influence of restoring forces, provided that there is no inter-plane coupling. The area occupied by the beam in phase space is given by $\pi\varepsilon$, where ε is the beam emittance. In case of beam acceleration, the Liouville theorem is not applicable and as a result emittance does not remain conversed. However, the quantity $\beta\gamma\varepsilon$, known as the normalized emittance is constant during the acceleration of beam. It is a common practice to report the beam emittance of accelerated beam. The transverse emittance in a particular direction (conventionally taken as '*x*' direction) satisfies the equation.

$$\gamma x^2 + 2\alpha x x' + \beta x'^2 = \varepsilon \quad . \tag{2.13}$$

where, α, β, γ are the well known Courant-Snyder or Twiss parameters.

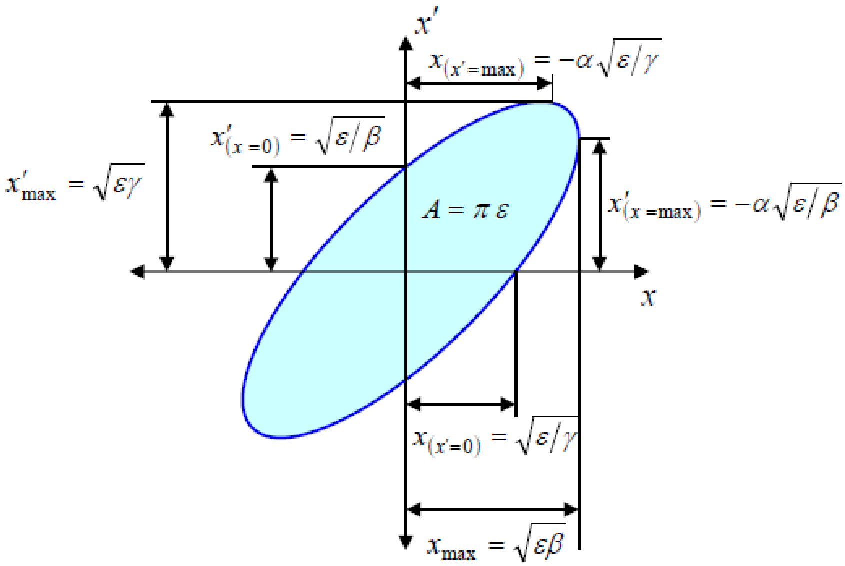

Figure 2.3: Beam ellipse

It is easy to observe that Eq. (2.13) defines an ellipse of area $\pi\varepsilon$ in two dimensional phase space. The ellipse is generally plotted in the *x*-*x*' phase space and the Twiss parameters α, β, γ are derived from the intercepts ellipse on the *x*-*x*' axes as shown in figure 2.3.

2.4.5 Sigma matrix

The phase space ellipse can also be described with a symmetric two dimensional sigma matrix **σ**

$$\boldsymbol{\sigma} = \begin{bmatrix} \sigma_{11} & \sigma_{12} \\ \sigma_{21} & \sigma_{22} \end{bmatrix} \quad . \tag{2.14}$$

Using Eq. (2.13) the following relations can be obtained between the Twiss parameters, and the sigma matrix.

$$\sigma = \begin{bmatrix} \sigma_{11} & \sigma_{12} \\ \sigma_{21} & \sigma_{22} \end{bmatrix} = \varepsilon \begin{bmatrix} \beta & -\alpha \\ -\alpha & \gamma \end{bmatrix} \quad . \tag{2.15}$$

$$\varepsilon = \sqrt{\sigma_{11}\sigma_{12} - \sigma_{22}{}^{2}} \quad . \tag{2.16}$$

2.4.6 Statistical beam emittance

The beam emittance in terms of occupied phase space area can be clearly defined only for an ideal hard-edged (uniform distribution) beam. In case of a non uniform beam distribution, that does not have a well defined cutoff, the number of particles enclosed by the phase space area will vary, resulting into a ambiguous definition of the beam emittance. This discrepancy in the definition of beam emittance was resolved through the introduction of the rms emittance by Chasman and refined by Lapostolle. The rms emittance is defined in terms of statistical parameters of the beam distribution in phase space. A beam distribution of *N* particles in two dimensional phase space (*x*, *x*') can be defined by its statistical moments as given in [14,15].

$$\langle x \rangle = \frac{1}{N}\sum_{i=1}^{N} x_i \quad . \tag{2.17}$$

$$\mathrm{var}(x) = \frac{1}{N}\sum_{i=1}^{N}\left(x_i - \langle x \rangle\right)^2 \quad . \tag{2.18}$$

$$\mathrm{cov}(x, x') = \frac{1}{N}\sum_{i=1}^{N}\left(x_i - \langle x \rangle\right)\left(x'_i - \langle x' \rangle\right) \quad . \tag{2.19}$$

for the mean, variance and covariance, a covariance matrix $\boldsymbol{\sigma}$ describing the particle distribution is given by

$$\boldsymbol{\sigma} = \begin{bmatrix} \mathrm{var}(x) & \mathrm{cov}(x, x') \\ \mathrm{cov}(x', x) & \mathrm{var}(x) \end{bmatrix} \quad . \tag{2.20}$$

With mean values $\langle x \rangle$ and $\langle x' \rangle$ equal to zero, the sigma matrix can be written as

$$\boldsymbol{\sigma} = \begin{bmatrix} \langle x^2 \rangle & \langle xx' \rangle \\ \langle x'x \rangle & \langle x'^2 \rangle \end{bmatrix} = \begin{bmatrix} \sigma_{11} & \sigma_{12} \\ \sigma_{21} & \sigma_{22} \end{bmatrix} \quad . \tag{2.21}$$

The rms beam size σ_x is defined as $\sqrt{\langle x^2 \rangle} = \sqrt{\sigma_{11}}$. The covariance matrix is the same the sigma matrix defined in the earlier section. The statistical emittance is known as the rms emittance and is defined by

$$\varepsilon_{rms} = \sqrt{\langle x^2 \rangle \langle xx' \rangle - \langle x'^2 \rangle} \quad . \tag{2.22}$$

In the case of a known beam distribution, the rms emittance can be related to the phase space area. Table 2.1 shows the fraction of particles encompassed into the given phase space area.

Table 2.1: The beam fraction enclosed in a given area for Gaussian and uniform distribution.

Area	Gaussian	Uniform
$\pi\varepsilon_{rms}$	39 %	25 %
$4\pi\varepsilon_{rms}$	86 %	100 %

It is important to note here, that a phase space area of $6\pi\varepsilon_{rms}$ contains ~ 95 % of the particles for a Gaussian distribution and the emittance corresponding to this area is often specified as $\varepsilon_{95\%}$.While for a uniform distribution the phase space area of $4\pi\varepsilon_{rms}$ contains 100% of the particles and emittance corresponding to it is called as $\varepsilon_{100\%}$, which is defined as $\varepsilon_{100\%} = 4\varepsilon_{rms}$.

2.4.7 Emittance of beam from an ion Source

In general, there are two major factors which contribute to the emittance of beam extracted from the ion sources as mentioned in [16]. The first is the thermal motion of ions, which occurs due to the ion temperature in the plasma and can be estimated by assuming Maxwellian velocity distribution of ions [17], the other one is due to the presence of falling magnetic field in the extraction zone, which causes the beam rotation [18]. Adding the two contributions, the normalized rms emittance can be estimated theoretically by:

$$\varepsilon_{n-rms} = 0.016\, R_{ex}\sqrt{\frac{k_B T_i Q}{M}} + 0.032\, R_{ex}^2 B_{ex}\frac{Q}{M} \quad \text{mm-mrad} \quad , \tag{2.23}$$

where, $k_B T_i$ is the ion temperature in eV, R_{ex} the radius of the extraction aperture in mm. Q the charge state of the ions, M the ion mass in atomic mass units and B_{ex} the magnetic at the extraction aperture in Tesla. It is easy to verify that at low ion temperature (< 1eV) the major contributor to the emittance is the presence of magnetic field [19, 20].

2.5 Ion sources for accelerators

The accelerators demand a wide variety of ion beams for various scientific and medical applications, like cancer therapy treatment using PET and SPECT [21]. For this purpose the ion sources are required to provide singly charged to multi-charged ion beams of varying intensities.

In order to satisfy the requirements of accelerators several types of ion sources with different characteristics have been built. The development of ion sources started in the beginning of the last century with the construction of electron impact ionization sources for mass spectroscopy applications [22]. The Penning ion sources came into existence with the invention of Cyclotron in the year 1930 [23, 24]. The invention of tandem accelerators triggered the research on negative ion sources. In the seventies, a major breakthrough took place in the field of ion sources with the development of the Electron Cyclotron Resonance Ion Sources (ECRIS) [7] and the Electron Beam Ion Sources (EBIS) [19, 25], followed by the invention of Microwave Ion Sources (MIS) in the mid eighties [26]. Nowadays, ECRIS and MIS are widely used and most preferred choice for the modern accelerator facilities, as they can produce sufficient amount of high charge state ions and intense singly charged ions as compared to the other type of ion sources. In the next section, a brief description of the working principle and different components of the Microwave Ion Source will be introduced.

2.5.1 Microwave ion sources

The Microwave Ion Sources operating at 2.45 GHz were first developed about 35 years ago mainly for the industrial use [26, 27]. These sources have also been extensively utilized in various scientific projects, due to its several advantages like, high stability, flexibility to operate in CW or pulsed mode and low transverse emittance.The most innovative design of a 2.45 GHz microwave ion source intended to produce intense beam of protons for injection into a RFQ accelerator was proposed at Chalk River National Laboratory [30, 31]. Based on this design, many 2.45 GHz microwave ion sources along with some improvements are being used throughout the world for various high power accelerator projects.

Table 2.2: The specifications of various 2.45 GHz microwave ion sources.

Facility/ Ion Source	Beam current (mA)	Beam pulse (ms)	Duty factor (%)	Normalized rms emittance (mm-mrad)	Extraction voltage (kV)	Microwave Power (W)
SILHI	108	CW	100	0.15	95	900
TRIPS	54	CW	100	0.07	80	1000
PSI	12	CW	100	0.045	60	600
ESS	40	2.84	4	0.3	50	700
PKUNIFTY	50	CW	100	0.18	35	700
VIS	35	CW	100	0.19	60	700
CPHS	70	0.5	2.5	0.18	50	600

As an example, some of 2.45 GHz microwave ion sources used in different scientific projects are listed in Table 2.2. In the next sub-section we will briefly outline the working principle and key components of the Microwave Ion Sources.

2.5.1.1 Working Principle

The working principle of the Microwave Ion Sources is based on the electron heating through the absorption of incident electromagnetic wave in the presence of a non-minimum magnetic field. When an electromagnetic wave is launched into the plasma chamber of Microwave Ion Source, the free electrons absorb a significant portion of the wave energy and impinge on the neutral atoms of the injected gas, leading to the ionization and subsequent formation of plasma. Finally, the ions are extracted from the plasma with the help of an electrostatic extraction system.

In Microwave Ion Sources, the magnetic field aids in the ionization process. It makes the electrons to move in a spiral orbit around the magnetic field lines. This process effectively increases the electron lifetime. Because of the quasineutral nature of the plasma, the ion lifetime is also increased, thus increasing the rate of ionization in the plasma. A confining type of magnetic field configuration is not required for the Microwave Ion Sources, as it is used to produce only singly charged ions. However, a high plasma density is desirable to produce high extracted beam current.

Generally, two different types of microwave ion sources working at a frequency of 2.45 GHz can be found based on the magnetic field profile. In the first type of ion sources, the magnetic field profile is almost flat in the plasma chamber. In this case, the magnetic field is designed in such a way so that resonance magnetic field occurs at entry and exit of the plasma chamber. Herein, the magnetic field is maintained at off-resonance in the central part of the plasma chamber, resulting into the formation of an overdense plasma i.e $n_e > n_c$.

A majority of the microwave ion sources operating at 2.45 GHz are of off-resonance type with a typical magnetic field of 0.1 T in the central part of the plasma chamber. In the other type of ion sources, the operating magnetic field is kept below the resonance magnetic field throughout the plasma chamber. In this case, the incident wave is not directly absorbed, but through the excitation of Bernstein waves. These waves can propagate inside the plasma without any density cut-off and can be absorbed at sub-multiples of the resonance magnetic field. Although this type of ion sources can achieve densities higher than the critical density n_c, but the plasma formed in this case is turbulent and non-uniform. It is due to this reason that they are not preferred as ion sources in the presently operating high current accelerators.

2.5.1.2 Microwave ion source components

The main components of the Microwave Ion Source common in almost all the designs are briefly explained in this section. Figure 2.4 shows a schematic sketch of the Microwave Ion Source. A short description about the different components of the ion source is described below. In some of the design of Microwave Ion Source, its components like, microwave generator, gas feeding system, magnet power supplies, and control system are biased to a high voltage potential (indicated by the dotted region in figure 2.4). Alternatively a waveguide break is introduced in the microwave line to keep all the components at the ground potential, except the plasma chamber [28].

Plasma chamber

It is a vacuum chamber specially designed with water cooling facility in which the plasma is generated and maintained. The gas and microwaves are also introduced into this chamber. The incident microwaves energize the electrons which ionizes the neutral gas atoms in this chamber to produce plasma. The generated ions in the plasma are then pulled out through an extraction aperture in the plasma chamber, thus producing an ion beam.

Microwave coupling system

The efficient transfer of electromagnetic wave energy from the microwave generator to the plasma is very crucial to achieve high ionization efficiency. Generally, the microwaves are guided to the plasma chamber through a waveguide matching transformer to obtain a progressive impedance match between the waveguide and plasma.

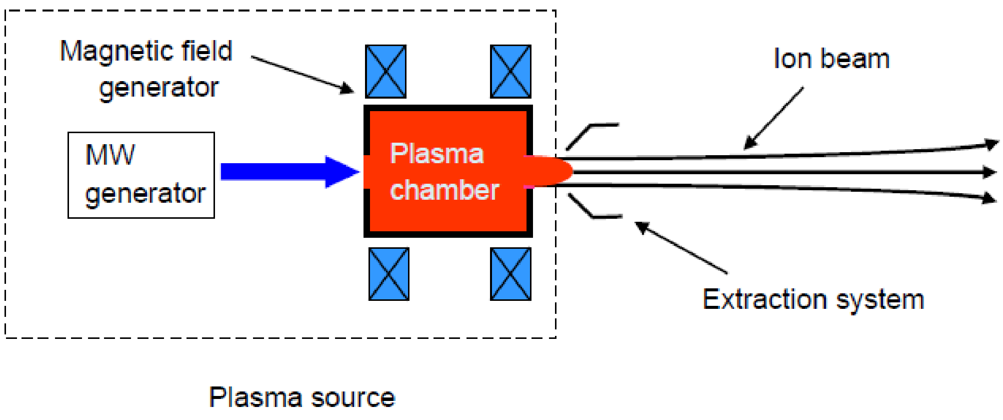

Figure 2.4: Schematic sketch of a Microwave Ion Source.

This transformer also helps to achieve a high electric field in the plasma chamber as compared to a simple rectangular waveguide. A detailed description about the design and performance of the waveguide matching transformer will be discussed in Chapter 4.

Magnetic field system

In the Microwave Ion Source generally the off-resonance type of magnetic field profile is maintained in the plasma chamber. The magnetic field is generated by electromagnets or permanent magnets. In some of the sources, there is a provision to move the magnets in the axial direction to optimize the magnetic field profile online, which results in the optimum ion source performance.

Extraction system

Most of the ion sources typically use a two or three electrode extraction system to extract the ions from the plasma. The electrodes in the extraction system are biased to different potentials for the ion beam formation from the plasma. For the extraction of positive ions from the plasma the ion source is biased to a positive potential with respect to the first electrode, which is maintained at the ground potential.

2.6 Summary

In this chapter, we have introduced the different plasma parameters and concepts of wave propagation in plasma that are related to the Microwave Ion Sources. Furthermore, a general discussion of ion beam characteristics crucial for the beam acceleration is discussed. Finally, an overview of different ion sources used in particle accelerators is presented with a specific focus on the physics and technology of Microwave Ion Sources.

Chapter 3

Ion source and low energy beam transport line

3.1 Introduction

This chapter gives a brief overview of the 2.45 GHz Microwave Ion Source and low energy beam transport (LEBT) system developed at VECC. Floor plan of the ion source and LEBT is shown in figure 2.1 together with the exact positions of different components.

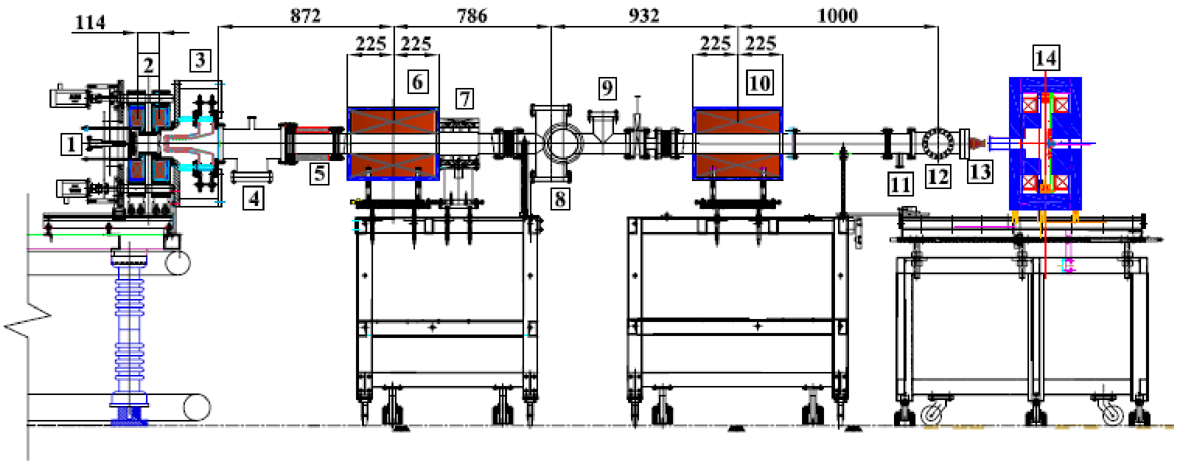

Figure 3.1: Layout of the microwave ion source and LEBT. 1. Water cooled double ridged waveguide, 2. Injection and extraction coils of ion source, 3. Two-segment ceramic insulators (Al_2O_3) column, 4. Port for vacuum pump and gauge, 5. DCCT assembly, 6. Beam line Solenoid-1, 7. Steering magnet, 8. Port for X-Y slit system, 9. Port for faraday cup, 10. Beam line Solenoid-1, 11. Port for gas feeding, 12. Diagnostic chamber with beam viewer port, 13. Faraday cup cum beam dump, 14. Dipole magnet to study beam inflection. All the distance between the components is expressed in mm.

This chapter is organized as follows: In Sec. 3.2, the 2.45 GHz microwave ion source along with its different sub-systems are described; while the LEBT line of ion source along with the various beam diagnostic devices installed in it are described in Sec. 3.3 and Sec. 3.4, respectively. In Sec. 3.5 the measurements results of total extracted beam current and atomic ion fraction as a function of different ion source operating parameters are described. The chapter concludes with a summary in Sec. 3.6.

3.2 Description of the 2.45 GHz microwave ion source

The ion source at VECC is an off-resonance type Microwave Ion Source. It has been designed and constructed to produce ~ 15 mA of beam current in CW (continuous-wave) mode at beam energy of ~100 keV. In the ion source hydrogen atoms are ionized by the electron impact ionization in a specially designed water cooled plasma chamber. The energy required for the ionization of atoms is gained by the electrons through an electric field setup in the plasma chamber by the incoming microwave power from a magnetron source at frequency of 2.45 GHz.

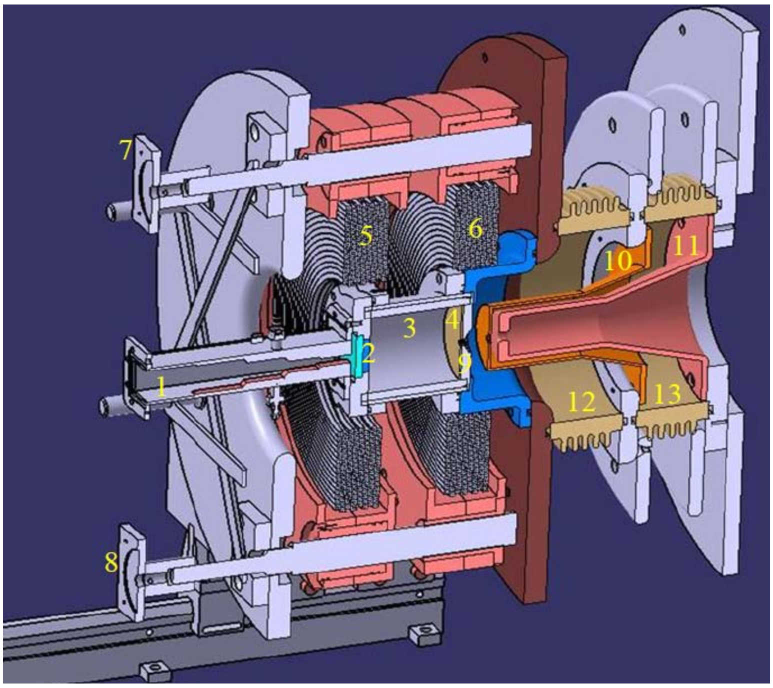

Figure 3.2: 3D CAD schematic of 2.45 GHz Microwave Ion Source at VECC. 1. Microwave coupling transformer, 2. Boron Nitride and Aluminium Nitride window, 3. Plasma chamber, 4. Boron Nitride disc, 5. Injection magnet coil, 6. Extraction magnet coil, 7, 8. Motorized shafts, 9. Plasma electrode, 10. Suppressor electrode, 11. Ground electrode. (12,13). Alumina ceramics for high voltage isolation and electrode support.

The microwave power is transferred from the generator to the plasma chamber through a series interconnection of rectangular waveguides, three stub tuners, auto tuner, waveguide bends and other impedance matching elements. The diode sensor continuously monitor the forward and reflected power and inhibit the magnetron high voltage power supply, if the reflected power exceeds 40 W. The chamber is immersed in an axial non-confining magnetic field configuration produced by two motor controlled adjustable solenoid coils fed with independent regulated dc power supply. Finally, the ions generated in the plasma are extracted from the plasma chamber through an orifice in the plasma electrode by applying suitable voltages to the electrodes of the extraction system. A sectional view of ion source assembly indicating the position of solenoid coils and extraction system is shown in figure 3.2. The main subsystems of ion source are described in the following sub-sections.

3.2.1 Plasma chamber and gas feeding system

The ion source has a double wall plasma chamber made of stainless steel grade 304L. The chamber is 90 mm in diameter and 100 mm long. The longitudinal channels are made on the outer surface of the inner wall of the plasma chamber for water cooling. In order to limit the high flux of back streaming electrons coming from the plasma into the microwave coupling transformer, a series combination of Aluminium nitride (AlN) and Boron Nitride (BN) plate is used at the entry of the plasma chamber. The BN plate is chosen to be placed in front of the plasma, supported on AlN plate, which has high thermal conductivity and low coefficient of thermal expansion. Due to the virtue of this property, AlN plate can easily sustain the heat load generated due to the back streaming electrons, without fracture. Another BN plate is fixed on the plasma electrode of the ion source to provide a high enough population of secondary electrons into the plasma, leading to a sufficiently high plasma density, resulting into a high beam current from the ion source. A controlled flow of hydrogen gas is introduced into the plasma chamber, through an adjustable leak valve EVR 116 [29]. The gas flow is kept in the range of 0.4 - 1 sccm (standard cubic centimetres per minute) depending on the operating conditions of the ion source. The plasma chamber and extractor region are evacuated by two sets of scroll and turbo-molecular pumps, each of 500 l/s pumping capacity. This pumping configuration gets a pressure of ~10^{-3} mbar in the plasma chamber and ~ $4\cdot10^{-7}$ mbar in the extraction region without the gas flow.

3.2.2 Microwave System

The microwave line of the ion source is shown in figure 3.3. The microwave power at a frequency of 2.45 GHz is generated by a 1.2 kW water cooled Magnetron and guided ahead through a WR 340 rectangular waveguide, operating in the TE_{10} dominant mode. A dual-directional coupler with a 60 dB coupling factor and a directivity of 30 dB with two individual diode detector is installed to record forward and reflected power arising due to the impedance mismatch between the waveguide and plasma.

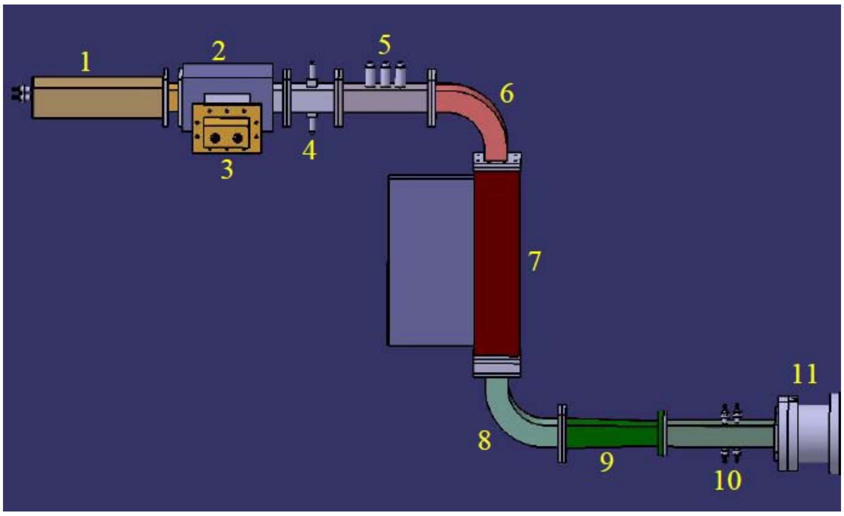

Figure 3.3: 3D CAD schematic of the microwave injection system. 1. Magnetron, 2. Circulator, 3. Dummy load, 4. Dual directional coupler, 5. Three stub tuner, 6. E-plane bend, 7. Automatic tuner, 8. E-plane bend, 9. WR 340 to WR 284 transition, 10. Microwave coupling transformer, 11. Plasma chamber.

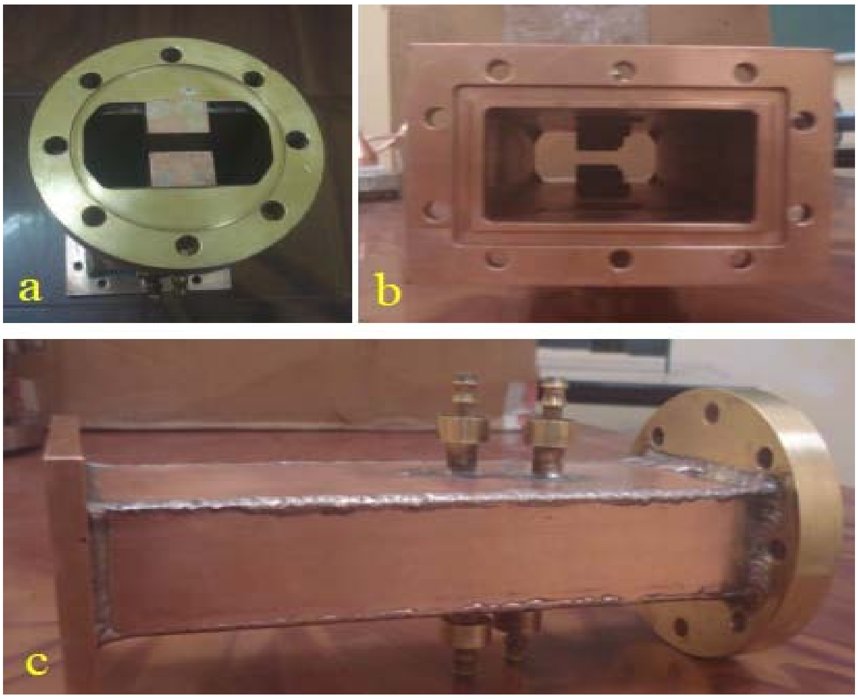

Figure 3.4: Photograph of fabricated microwave coupling transformer. a. plasma side, b. air side, c. side view, the cooling lines are visible in the photograph.

A combination of manual 3-stub tuner and a four stub automatic tuner is used to adjust the amplitude and phase of the waveguide impedance to that of plasma impedance. A tapered WR 340 - WR 284 waveguide adapter is used to match the input impedance of microwave coupling transformer to the WR 340 waveguide section of the microwave line. Finally a water cooled microwave coupling transformer based on a four-step double ridged waveguide is connected at the entry of the plasma chamber. This design objective of this transformer is to match the dominant mode impedance of WR 284 waveguide with the equivalent plasma impedance and at the same time it should also concentrate the electric field in the centre of the plasma chamber, leading to an efficient ionization of the injected gas atoms in the plasma chamber. Figure 3.4 shows the different views of the water cooled microwave coupling transformer. The detailed design, simulation and performance of the microwave coupling transformer with the ion source will be described in Chapter 4.

3.2.3 Magnetic System

The magnetic system of the ion source is composed of two identical water cooled solenoid coils positioned at a distance *d* from each other, as shown in figure 3.5. Each solenoid coil is constructed from a square copper conductor of 6 mm in dimension with a 2.5 mm diameter central hole for water cooling. The coil has an outer diameter of 352 mm, inner diameter of 170 mm and an axial length of 60 mm. A motor controlled drive is used to change the distance *d* between the coils to obtain an off-resonance magnetic field profile prior to the operation of the ion source and also it is ensured that the resonance field of 87.5 mT occurs at the location of two dielectric windows [30-32].

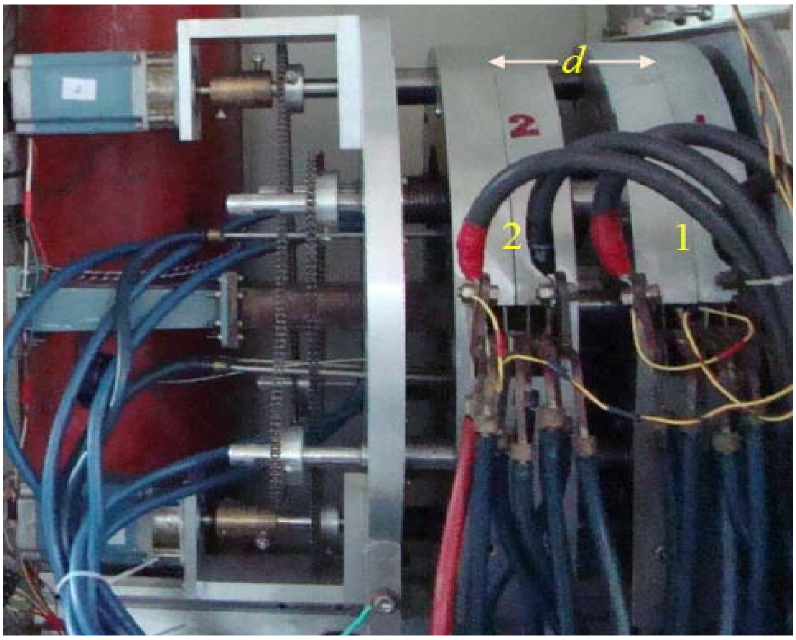

Figure 3.5: Photograph of the magnetic system of the ion source, 1. Extraction coil, 2. Injection coil, 3. *d* is spacing between the coils.

The magnetic field profile obtained in the ion source at a dc current of 103 A in each coil with a distance *d* of 128 mm between the coils is shown in figure 3.6. This magnetic field profile is used in most of the experiments described in this thesis, unless stated otherwise. It can be seen from the plot that the magnetic field profile is almost flat and exceeds the resonance field along the complete length of plasma chamber, except at its two extremes.

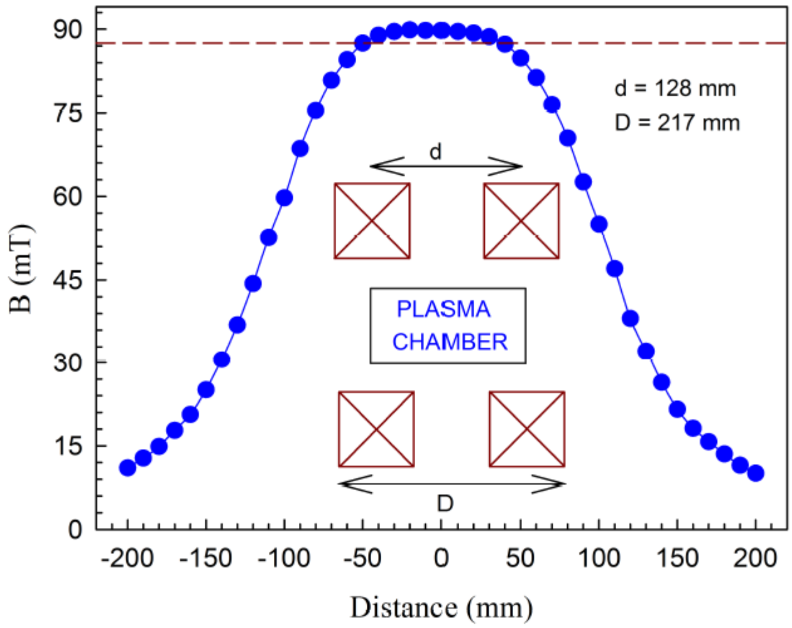

Figure 3.6: The measured axial magnetic field along the axis of the plasma chamber.

3.2.4 Extraction system

The ion beam extraction system of the Microwave Ion Source is based on a standard triode configuration as shown in figure 3.7. This configuration has three electrodes, i.e. plasma, acceleration and ground electrodes. All electrodes are made of stainless steel.

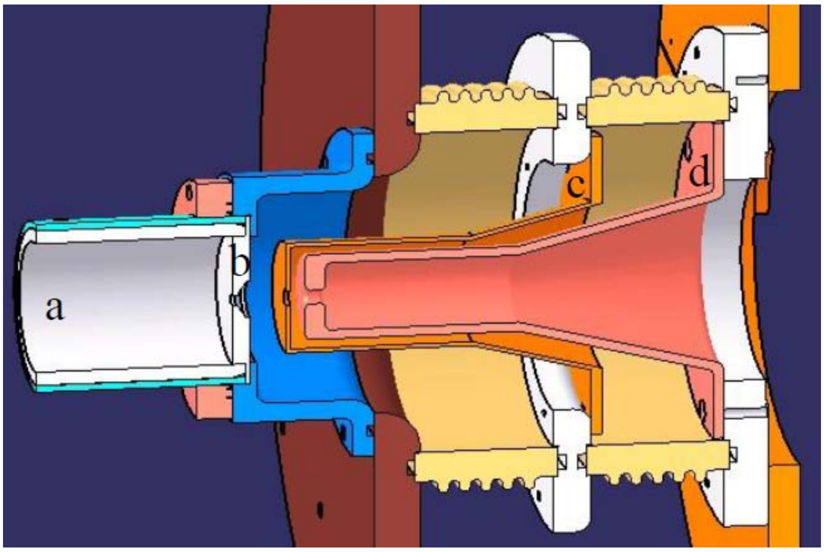

Figure 3.7: 3D CAD schematic of triode extraction system. a: plasma chamber, b: plasma electrode, c: acceleration electrode, d: ground electrode.

The insulators are made of 99.5 % pure alumina ceramic. They are used to support the acceleration electrode as well as to isolate the high voltage deck from the beam line, which is at the ground potential. The ion beam is extracted from plasma chamber through a hole of 6 mm in diameter in the centre of the plasma electrode. The acceleration electrode with an aperture diameter of 8 mm and length of 177 mm is placed at a distance of 16.5 mm from the plasma electrode. It is biased to a potential of ~ -2 kV during ion source operation. This negative potential repels the low energy secondary electrons produced in the beam line and prevents them to enter into the extraction region. The ground electrode is at zero potential. It is located at a distance of ~ 5.8 mm behind the acceleration electrode with an aperture diameter of 8 mm and a length of 235 mm. Figure 3.8 shows a photograph of assembled ion source and its components on the high voltage deck showing the microwave feeding system, the solenoid coils, the hydrogen gas feeding system, and the extraction system.

Figure 3.8: Photograph of the installed Microwave Ion Source at VECC. 1. Isolation transformer, 2. 2.45 GHz water cooled magnetron, 3. Magnetron power supply and control unit, 4. Circulator and dummy load assembly, 5. Dual directional coupler and diode detector, 6. Four stub auto tuner, 7. H_2 gas cylinder, 8,9. AC synchronous motor, 10. Water cooled double ridged waveguide, 11. Injection magnet coil, 12. Extraction magnet coil, 13. Extraction system, 14. High voltage deck.

3.3 Low energy beam transport system

Figure 3.9: Photograph of the installed low energy beam transport line. 1. Direct-Current Current Transformer, 2. Solenoid Magnet-1 (S1), 3. Steering Magnet, 4. Water-cooled x-y slit, 5. Pneumatically actuated Faraday cup, 6. Solenoid Magnet-2 (S2), 7. Neon gas cylinder, 8. Gas dosing valve, 9. Diagnostic Chamber, 10. Faraday cup cum beam dump.

The extracted beam from the ion source is focussed, mass selected and characterized in the LEBT system shown in figure 3.9. LEBT consists of two solenoid magnets (S1 and S2), steering magnet, vacuum equipments, water-cooled x-y slit and several other diagnostic equipments for ion beam characterization. The extracted ion beam from the ion source primarily consists of H^+, H_2^+ and H_3^+ ions. The total extracted beam current is measured by a Direct-Current Current Transformer (DCCT) installed just after the extraction region. This current is denoted as $I_{\_DCCT}$ throughout the thesis. In order to focus protons and reject molecular ions out of a mixture of ions coming from the ion source, a solenoid magnet (S1) with a peak field of 0.4 T and effective length 0.4 m followed by a water cooled x-y slit is installed in the LEBT line. The current in S1 magnet is setup in such a way so that protons gets focussed at the location of water cooled x-y slit with an square aperture of 10 mm.

Due to the dependence of solenoid lens focal length on the velocity of ions, the molecular ions diverge at the slit location and collide with the x and y jaws of slit [33]. The selected proton beam current is measured by a water cooled faraday cup with electric suppression, installed just after the slit. The beam is focussed and transported in the LEBT line by a solenoid magnet S2, which has identical parameters as that of magnet S1. Furthermore, beam characteristics like beam spot, beam emittance and beam profile are measured in the diagnostic chamber installed at a distance of 0.8 m after the S2 magnet. Finally, a water cooled tapered faraday cup is installed at the end of beam transport line to record the transported proton beam current. It also acts as a beam stopper.

3.4 Beam diagnostic elements

The ion beam transmission from the ion source to the end of LEBT line is dependent on different parameters of the ion source and LEBT system. In order to quantify the dependence of ion beam properties on these parameters different diagnostic devices like, DCCT, slits, Faraday cups, and a beam profile monitor are installed in the LEBT line of Microwave Ion Source. In this section, we briefly describe the different beam diagnostic devices installed in the LEBT line.

3.4.1 Faraday Cup

Faraday cup (FC) is the most popular diagnostic tool for beam current measurement [34-36]. In the LEBT line of Microwave Ion Source, two water cooled FC are installed. The first one is a standard FC with 1 kW power dissipation capability and is installed just after the slit. Figure 3.10 shows the photograph of FC. The FC is inserted into the beam path to measure the beam current and is retracted out of the beam line to transport the beam ahead.

The movement of the FC is made with the pneumatically actuated and electrically controlled solenoid valve. The readout of the FC position is obtained by two micro switches provided on the water-cooled actuator assembly. The beam is stopped in a water-cooled cup installed at the bottom of the FC assembly. The beam stopper cup is electrically isolated and thermally conductive to the FC body. The maximum acceptable beam diameter of FC is fixed by an aperture plate installed in front of the beam stopper. The first aperture plate is followed by a bias aperture plate. It is negatively biased and reflects back the secondary electrons coming from the FC towards itself. The electrical connection to the beam stopper cup and bias aperture is realized outside the vacuum through individual ceramic feed through. Finally, the FC signal is dropped across a precision resistor and developed voltage is readout, which is displayed on the graphical user interface of LEBT line. An in-house developed water cooled FC is shown in figure 3.11. It is installed at the end of LEBT line. It is a fixed FC without any actuation mechanism. The beam stopper of FC is a tapered conical cup with longitudinal water cooling channels. It is mounted on a DN100 CF flange and isolated from the beam line with a Teflon block. The current readout of this FC is obtained in a similar way as that of previous FC.

Figure 3.10: Photograph of the pneumatically actuated Faraday cup. 1. Water cooled cup with aperture plate, 2. Pneumatic cylinder, 3, 4. Limit switches, 5. Flange with BNC connector for current readout and electron suppression bias supply.

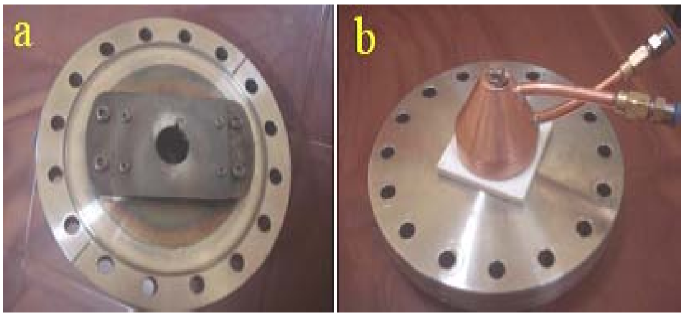

Figure 3.11: Photograph of the Faraday cup cum beam dump. a. Vacuum side, with an aperture plate of 20 mm diameter, b. Air side, with a water cooled conical beam stop.

3.4.2 Beam viewer

The primary method to acquire an image of the beam cross-section is the use of scintillating screens, where the scintillation produced by the impinging beam on the screen is captured through a video camera. Usually, this arrangement is known as beam viewer. The choice of a scintillating material depends on factors like light output, sensitivity and life time. The YAG: Ce and ZnS scintillators are generally used for low beam currents, while for high power ion beams, doped alumina ceramics are used [37, 38]. Figure 3.12 shows the photograph of an in-house developed beam viewer together with the pneumatic actuation. It is installed in the diagnostic chamber of the LEBT line after the S2 solenoid.

Figure 3.12: Photograph of the water cooled beam viewer. 1. Alumina disc with x and y grid lines, 2. Vacuum bellow, 3. Pneumatic actuator, 4. Water cooling line.

In the beam viewer, a 2 mm thick and 70 mm diameter alumina ceramic disc is used as a scintillating screen. This screen is marked with horizontal and vertical lines each spaced at a uniform distance of 5 mm. The alumina ceramic disc is mounted on a water cooled plate made of copper, which is attached to a pneumatic actuator. The beam viewer is brought in the beam path by the actuator to capture the beam cross-section on the screen, as and when required.

3.4.3 Direct-current current transformer

A DCCT is an indispensable diagnostic device for the non-intrusive measurement of dc beam current in high intensity machines. The DCCT works on the principle of zero flux detection combined with active feedback circuit [39, 40]. The DCCT consists of two cores, which are driven in anti phase to saturation region by a modulation current. The excitation of these cores to saturation region causes distortions in their modulation current waveforms. These distortions give rise to odd-harmonics in the frequency content of the modulation current waveform. However, due to opposite phase excitation of the two cores, the difference between their modulation current is zero, provided the cores have identical B-H characteristics. A DC current flowing through the cores magnetizes them with the same polarity and as a result both the cores do not reach saturation at the same time. As a result, the difference between the modulation current of the cores is not zero, which gives rise to a second harmonic component of the modulation frequency. This second harmonic component is detected by a synchronous detection circuit. In order to increase the DCCT bandwidth, the signal proportional to the AC component of the beam current obtained from an AC current transformer is combined with the second harmonic detector output. The two signals are combined to produce a compensating current, which passes through both the cores and generates a magnetic flux that is intended to cancel the flux produced by the beam current. In this way the compensating current is always equal in magnitude to the beam current. The voltage developed across a high precision resistor by the flow of compensating current through it is taken as the DCCT output.

In the Microwave Ion Source, the total extracted beam current is measured by a modular parametric current transformer (MPCT) from Bergoz company [41]. The sensor head of DCCT mounted on a beam pipe is shown in figure 3.13. A shielded cable connects the DB15 connector on the sensor head to the electronics box of DCCT. The electronics box is provided with circuits of modulation, sense and feedback required for the operation of DCCT. Three selectable ranges with a full scale value of 10mA, 20 mA and 30 mA are also provided on the electronics box for beam current measurement. The output voltage of DCCT is ± 5V, corresponding to the full scale value of beam current in the all the ranges. The calibration of DCCT is done by passing a known value of current through it and recording its value on a current meter. During the regular operation of the ion source, the DCCT readout is recorded and displayed on a 3.5 digit digital panel meter.

3.4.4 Water cooled x-y slit

The beam defining slit used in the ion source is a combination of horizontal and vertical slits, with water cooling and maximum power dissipation capability of 1 kW.

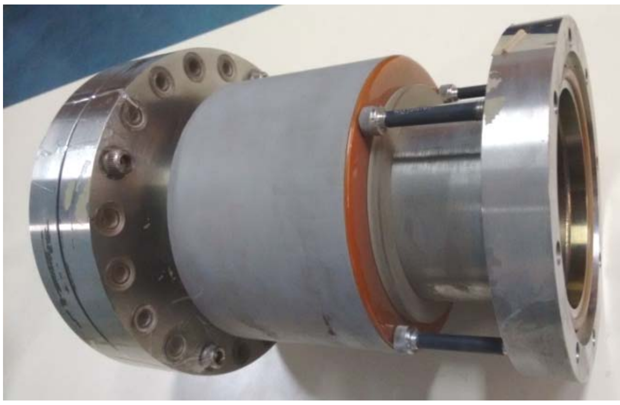

Figure 3.13: Photograph of the DCCT sensor head mounted on a vacuum chamber.

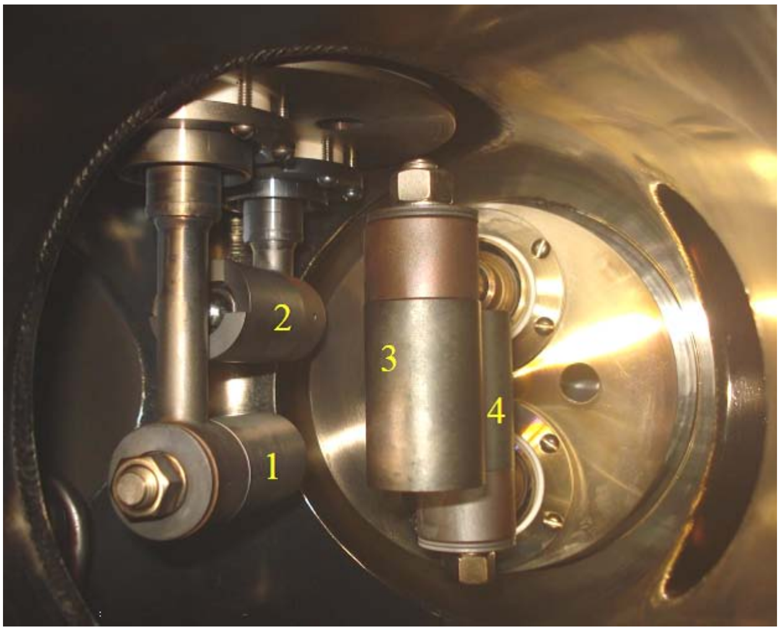

Figure 3.14: Photograph of the water-cooled x-y slit. 1,2. Vertical jaws, 3,4. Horizontal jaws.

Each slit consists of two cylindrical jaws made of tantalum. The two slits are individually positioned with the help of a motorized drive implemented using a combination of gear box and AC synchronous motors. The position readout of the two slits is obtained with their corresponding multi-turn potentiometers and current readout of the individual jaws is obtained through four BNC connectors mounted in a set of two, on the horizontal and vertical slit mounting flanges. During the ion source operation, the position of the slits is adjusted as per the requirement. The horizontal jaws and vertical jaws are shown in figure 3.14. During the ion source operation the current readout of the individual slit jaws are recorded and equalized using the steering magnet just after the solenoid magnet S1.

3.4.5 Non-interceptive beam profile monitor

A non-interceptive beam profile monitor is used to measure the beam profile of the high current beam extracted from the Microwave Ion Source. The high current proton beam produces fluorescence in the visible region of the light spectrum due to the excitation of residual gas molecules in the LEBT line. In order to capture the image of the beam induced

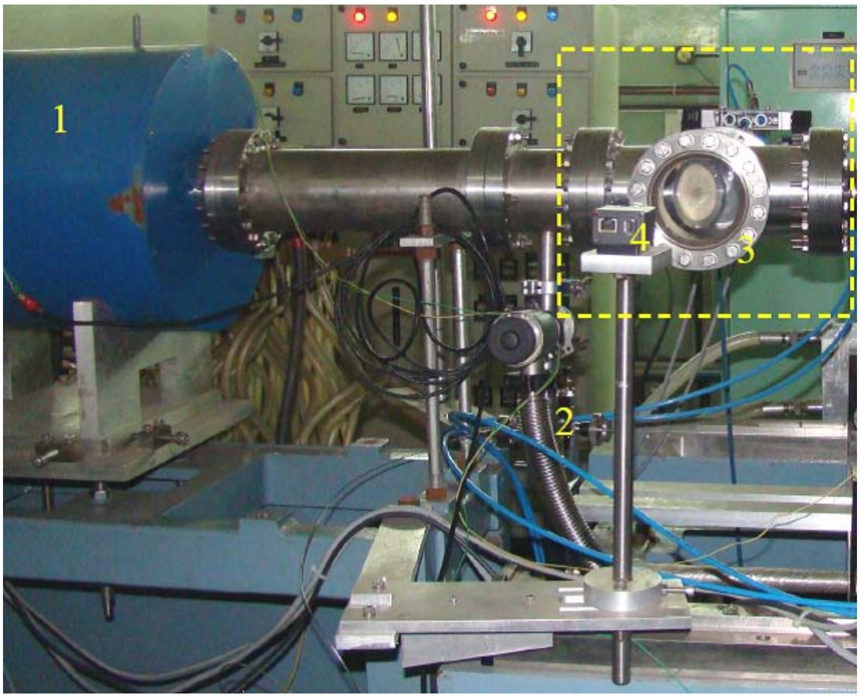

Figure 3.15: Setup for non-interceptive beam profile measurement. 1. Solenoid magnet (S2), 2. Gas dosing valve , 3. Glass viewing window, 4. CCD camera.

fluorescence a four port diagnostic chamber with viewing window and water cooled beam viewer is installed in the LEBT line as shown in the dotted region of figure 3.15.The image of the beam induced fluorescence produced by the high current proton beam is captured through a CCD camera, installed in front of the viewing window. The captured image is analyzed and the beam profile is obtained by an algorithm implemented in a MATLAB program [42]. Moreover, the beam profile of space charge compensated proton is also obtained with the injection of a Neon gas into the LEBT line. The gas injection is done by a gas dosing valve, UDV 146 located just before the diagnostic chamber. This monitor is also used to estimate the beam emittance of the space charge compensated 75 keV, 5 mA proton beam. A detailed discussion about the beam emittance and space charge compensation measurements will be described in Chapter 5.

3.5 Experimental Measurements

The beam extracted from the ion source consists of different ionic species of the injected gas. The currents of different ionic species extracted from the plasma are strongly dependent on different operating parameters of the ion source. At some operational settings of the ion source, the undesired ionic species extracted from the plasma may form a significant fraction of the total beam current and will mainly contribute towards the poor efficiency of beam transport in the LEBT line. Therefore, it is required to identify the operating parameters of the ion source, at which the maximum beam transmission of single ion species (mostly atomic) is obtained in the LEBT line for a given microwave power. In order to find out the optimum operating parameters of Microwave Ion Source at VECC, the extracted beam current and proton fraction were measured as a function of gas flow rate, microwave power and magnetic field profile of the ion source. Results of this measurement are described in Sec. 3.5.1.

The plasma density plays an important role in the performance of ion source. A higher value of plasma density leads to high beam current being extracted from the ion source. The widely used method to increase the electron density in the ion source is to place an insulator disc with a high secondary electron emission coefficient at the entry and exit of the plasma chamber [43, 44]. The supply of cold electrons from the insulator into the plasma helps to increase the rate of ionization of the injected gas atoms and molecules. In the Microwave Ion Source, a 5 mm thick BN plate is placed at the entry of the plasma chamber, whereas a 2 mm thick BN plate with an 8 mm diameter orifice is fixed on the plasma electrode. Moreover, the trace amount of water is also introduced into the plasma chamber to investigate its effect on the extracted beam current and proton fraction [45]. In order to quantify the effect of placing insulator and adding water into the plasma chamber on the performance of the ion source, the extracted beam current and proton fraction were measured as a function of microwave power. The results of this measurement are described in sub-Sec. 3.5.2.

It has been well established by studying the performance of Microwave Ion Sources operating at different laboratories that the diameter of the plasma chamber has a deep influence on the plasma density and atomic ion fraction [46]. In general, the ion source designers choose a smaller diameter plasma chamber, because this choice helps to obtain a high electric field in the plasma chamber resulting in a high extracted beam current from the ion source. However, due to the increased probability of wall recombination effects with smaller diameter plasma chamber, the atomic ion fraction is reduced. In order to understand the effect of these two competing plasma processes on the performance of the Microwave Ion Source, we performed experiments with plasma chamber having different diameters. In the experiment we inserted the aluminium cylinders in the plasma chamber and measured the extracted beam current and proton fraction. The results are described in sub-Sec. 3.5.3.

3.5.1 Optimization of the operating parameters of ion source

3.5.1.1 Variation of gas pressure

In order to perform the experiment described here, the ion source was initially conditioned for several hours in the presence of magnetic field, an extraction region pressure of ~ $4.0 \cdot 10^{-7}$ mbar, with extraction and suppressor electrode voltages set at 75 kV and -2 kV respectively. The drain currents of the extraction voltage power supply and suppressor voltage power supply was regularly monitored throughout the conditioning process. The hydrogen gas was then slowly injected into the plasma chamber by adjusting the leak valve and conditioning was continued till the pressure reached to ~ $1.1 \cdot 10^{-5}$ mbar in the extraction region. At this stage the drain current was stabilized to ~ 0.2 mA. Thereafter, the microwave power was slowly introduced into the plasma chamber; until stable plasma discharge was created in the chamber, which was indicated by the stable readout of beam current and drain current of extraction voltage power supply. At the same time, the reflected power was also monitored and kept below 5% with the help of a four stub automatic tuner at the maximum microwave power (400 W) raised during the experiment. Once the current readout of DCCT was stable within ± 0.1 mA, then the data acquisition of extracted beam current and proton fraction was performed as a function of microwave power in the range (100-350) W, at four different operating pressures in the extraction region. We have estimated the approximate proton fraction (η) by taking the ratio of beam current measured on water cooled faraday cup after selection by the slit to the total beam current (I_{DCCT}) measured by DCCT.

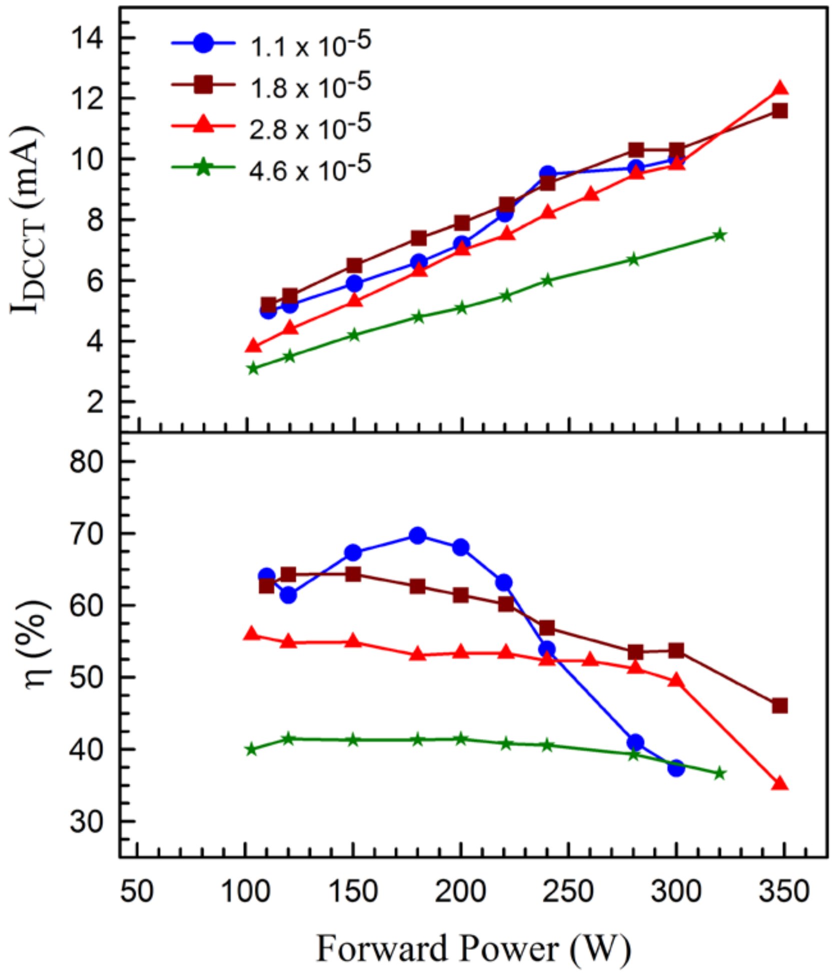

Figure 3.16: Variation of extracted beam current and proton fraction η as a function of microwave power at four different gas pressures (in mbar).

The measurement results of this experiment are shown in figure 3.16. It can be seen from this that the extracted beam current for a fixed amount of microwave power, is higher for low pressure settings as compared to high pressure settings. This phenomenon is related to the reduction of ionization rate with an increase in rate of gas flow. In the case of high pressure setting at fixed microwave power, the cold electron density is possibly increased in the ion source, which effectively brings down the average electron temperature in the plasma. Consequently, the ionization rate is reduced in the plasma, leading to a lower value of extracted beam current. Therefore, to increase the ionization rate at this high pressure setting a relatively high amount of microwave power is required to generate high density plasma with sufficient number of energetic electrons. A minor deviation from the observation reported here can be seen at a pressure setting of $1.1 \cdot 10^{-5}$ mbar. This could be attributed to insufficient gas flow to generate higher beam current as compared to the pressure setting of $1.8 \cdot 10^{-5}$ mbar, at a fixed value of microwave power.

A maximum beam current of 12 mA has been extracted from the ion source at a pressure setting of $2.8 \cdot 10^{-5}$ mbar as shown in figure 3.16. The extracted beam current for different pressure settings showed an increasing trend with an increment in the microwave power. In contrast to extracted beam current measurements, the proton fraction is found to be nearly constant upto a microwave power of ~ 250 W and drops with a further increase in the microwave power for operating pressures in the range of $1.1 \cdot 10^{-5}$ mbar to $4.6 \cdot 10^{-5}$ mbar. This phenomenon occurs probably due to a low operating pressure of $1.1 \cdot 10^{-5}$ mbar, for which the available gas atoms in the plasma chamber are significantly ionized at a microwave power of ~ 180 W and a maximum proton fraction of ~ 70% is reached. Above a microwave power level of 180 W there is a drop in η, which may be due to degassing from the walls of plasma chamber, leading to a possible contamination of the plasma. As the gas pressure was increased to $1.8 \cdot 10^{-5}$ mbar the proton fraction of ~ 64% at a similar microwave level of 180 W was recorded. This reduction occurs probably due to the cooling of energetic electrons responsible for the gas ionization, as explained earlier in this section. In this case, the change in proton fraction above microwave power of 200 W was relatively very less as compared to the previous pressure setting. The main factor responsible for this phenomenon was the comparatively higher gas pressure in the plasma chamber as compared to the previous case. This reasoning is also supported by measurements at the other two operating pressure levels of $2.8 \cdot 10^{-5}$ mbar and $4.6 \cdot 10^{-5}$ mbar.

3.5.1.2 Variation in drain current

In order to study the extraction system efficiency of Microwave Ion Source, the drain current of extraction and suppressor voltage power supplies were measured as a function of the extracted beam current at different operating pressure levels. The measurement was performed at similar values of extraction voltage and suppressor voltage as mentioned earlier in this section. A parameter η_{ex} is defined as the ratio of extracted beam current measured by DCCT to the extraction voltage power supply drain current. This parameter is taken as a measure for the extraction system efficiency. The variation of η_{ex} with forward power at different pressure settings are plotted in figure 3.17. It can be readily seen from the figure 3.17 that at an applied microwave power of 300 W, η_{ex} is above 80 % for different pressure settings, except in the case of $4.6 \cdot 10^{-5}$ mbar, where η_{ex} is 77 %.

Another important characteristic of Microwave Ion Source, which can be observed here is that η_{ex} increases with the increase in extracted beam current. The change in η_{ex} is ~ 10 % for different pressure settings, except at $1.1 \cdot 10^{-5}$ mbar, in which the change is limited to ~ 4 %.

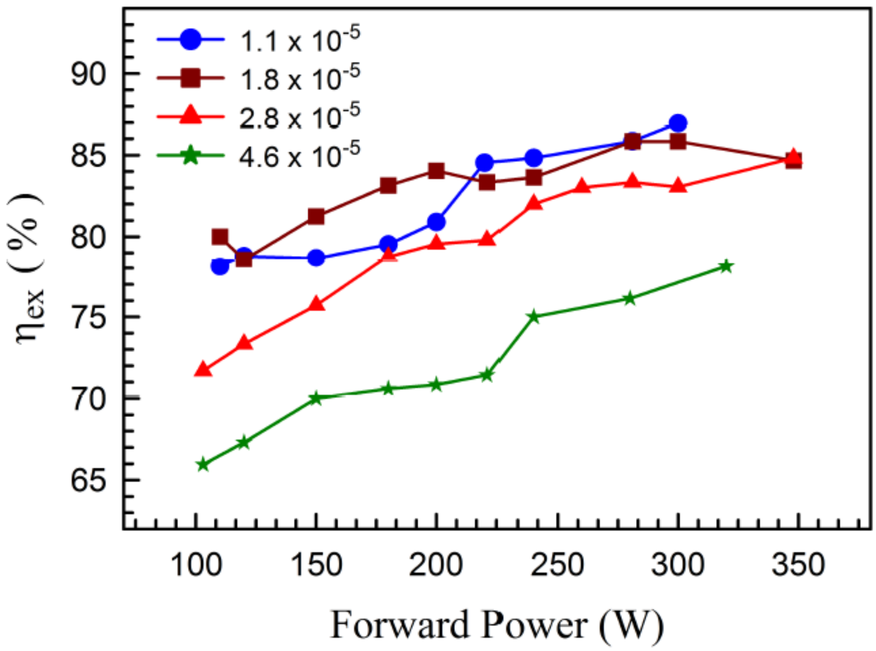

Figure 3.17: Variation of extraction efficiency η_{ex} as a function of microwave power at four different gas pressures (in mbar).

The suppressor voltage power supply drain current at a particular pressure level was almost constant with the change in microwave power, however, a variation from 0.5 mA to 1.0 mA was recorded, at different gas pressure settings.

3.5.1.3 Variation in magnetic field

In this experiment, the effect of magnetic field profile on the extracted beam current was studied. The extracted beam current was recorded with a change in injection coil current (I_inj) from 97 A to 107 A at the fixed values of extraction coil current (I_ex), microwave power and gas pressure. The result of this measurement is shown in figure 3.18 (a). The previous experiment was repeated with a similar change in extraction coil current. This result is illustrated in figure 3.18 (b). Both the experiments were carried out at a pressure of $2.8 \cdot 10^{-5}$ mbar with an applied microwave power of 200 W. The reflected power was always maintained below 5% by the auto tuner during the experiments. The proton fraction was measured to be almost constant with the variation in injection and extraction coil currents.

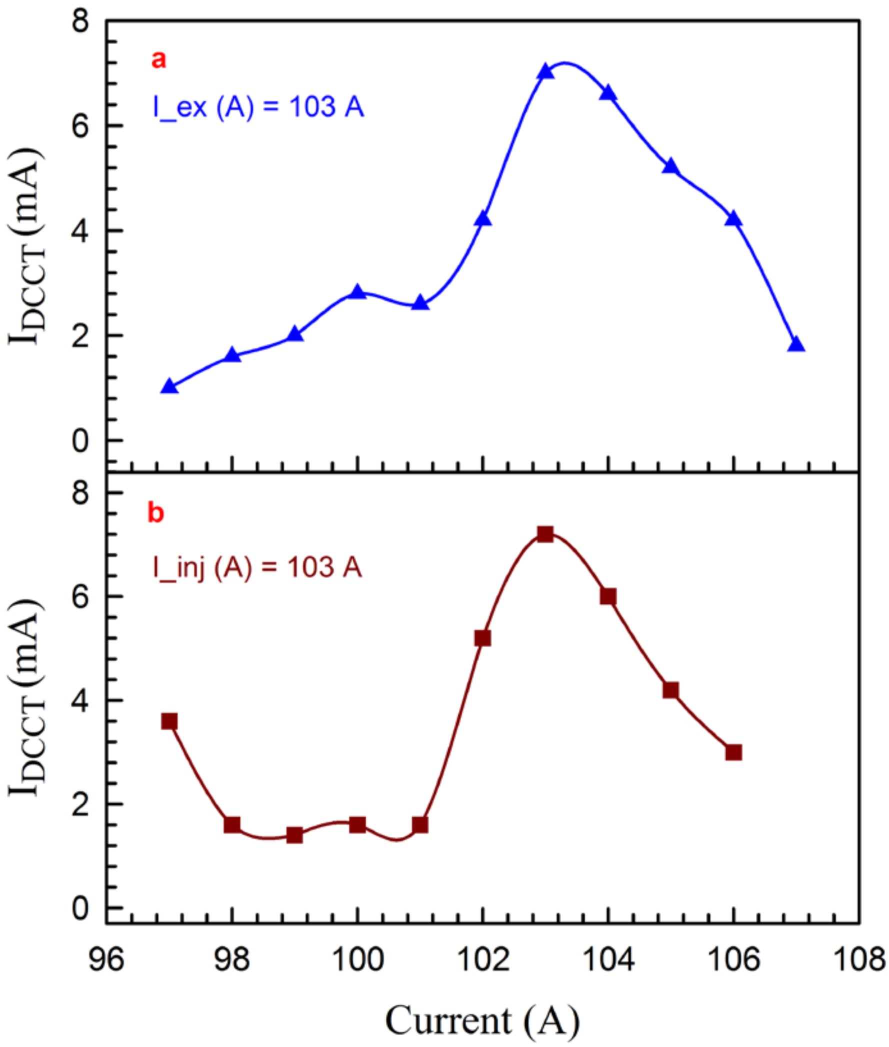

Figure 3.18: (a) Variation of extracted beam current with the change in I_inj. (b) Variation of extracted beam current with the change in I_ex.

It can be seen here, that extracted beam current is very sensitive to the change in coil currents. As shown in figure 3.18, the measured extracted beam current has a maximum value of ~ 7 mA, obtained near the resonance magnetic field. The beam current showed a similar trend with the change in both coil currents, away from the resonance value.

3.5.2 Effect of water addition

In order to study the effect of water introduction into the plasma chamber on the extracted beam current and proton fraction, we have introduced trace amount of water in the 90 mm diameter plasma chamber. The extracted beam current and proton fraction was recorded as a function of microwave power at a pressure of $1.1 \cdot 10^{-5}$ mbar in the extraction region. The measurement results are shown in figure 3.19. It can be seen from the plot that extracted beam current increases from 7 mA to 9 mA with the addition of water in the plasma chamber. It is quite evident from the graph that the extracted beam current tends to saturate in the range of forward power between 180 W to 200 W. The proton fraction shows an increasing trend at lower power levels and settles down to nearly same value as that obtained without the introduction of water in the plasma chamber. This probably happens due to the fast evaporation of water at higher power levels.

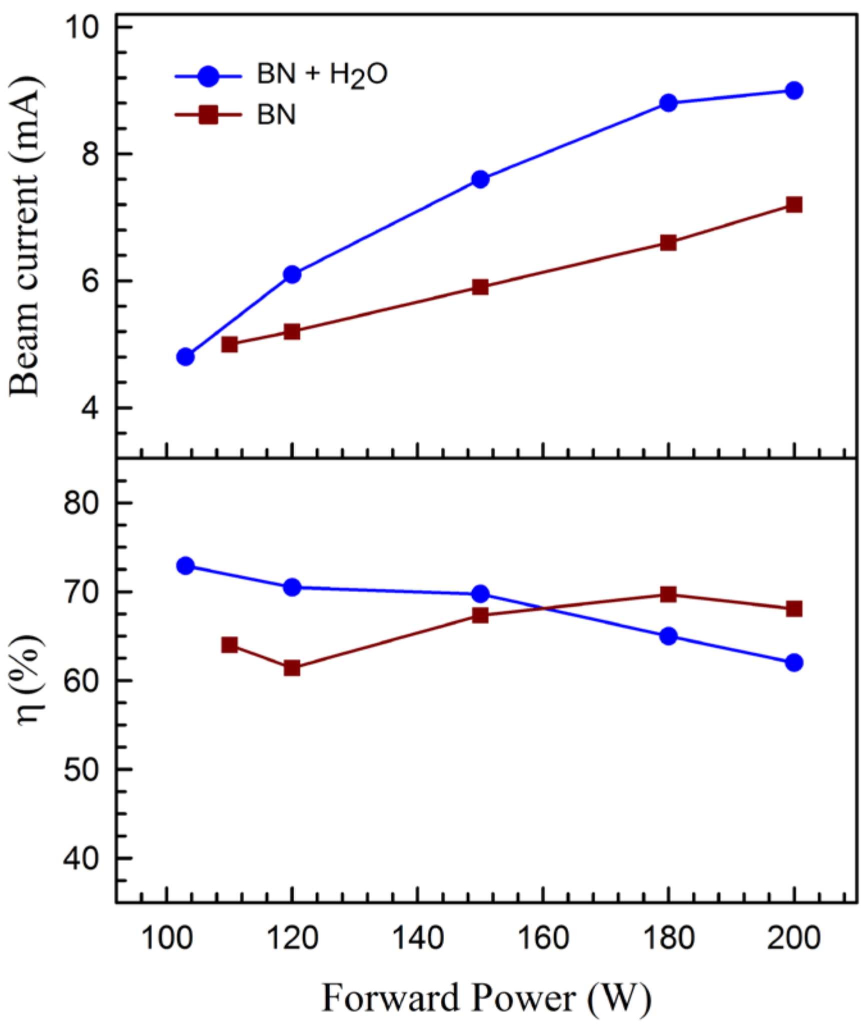

Figure 3.19: Variation of extracted beam current and proton fraction as a function of microwave power for the case of water addition in the 90 mm diameter plasma chamber.

As we could not maintain a constant supply of water vapours into the plasma chamber due to the experimental setup limitations, the proton fraction drops and reaches near to the proton fraction that was obtained without the addition of water into the plasma chamber.

3.5.3 Effect of different diameter plasma chamber

In order to study the influence of plasma chamber diameter on the performance of ion source, we have performed an experiment to measure the extracted beam current and proton fraction as a function of microwave power for the case of two different aluminium cylinders with an inner diameter of 35 mm and 45 mm inserted into the plasma chamber. Figure 3.20 shows the photograph of a 45 mm inner diameter aluminium liner inserted into the plasma chamber. In the experiment described here, a higher field is expected for both the aluminium cylinders as compared to the 90 mm plasma chamber. Therefore the ion source was operated at a relatively lower gas pressure of $5 \cdot 10^{-6}$ mbar in the extraction region, to obtain a high ionization efficiency of the hydrogen gas. All other parameters like magnetic field, extraction voltage and suppressor voltage were kept fixed, as described in the sub-section 3.5.1.1.

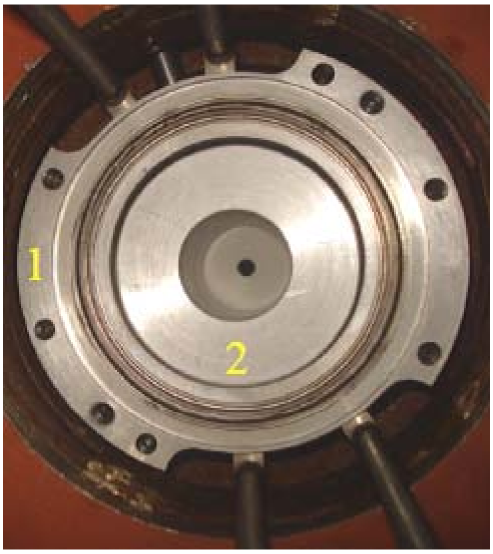

Figure 3.20: Photograph of aluminium liner inserted into the plasma chamber 1. Plasma chamber, 2. aluminium liner of 45 mm diameter.

Thereafter, the extracted beam current and proton fraction was recorded with a change in microwave power from 100 W to 300 W. Furthermore, the same experiment was performed again with the 35 mm inner diameter aluminium cylinder inserted into the plasma chamber. Results of the measurement are shown in figure 3.21. It can be seen from the plot, that extracted beam current for both aluminium cylinders is almost similar upto a microwave power of 200 W. However, for microwave power above 200 W, the extracted beam current for smaller diameter cylinder is more than the larger diameter cylinder. The variation in the behaviour of the two aluminium cylinders probably arises due to the fact that, for a fixed amount of applied microwave power, a relatively higher electric field is possibly setup in the smaller diameter cylinder.

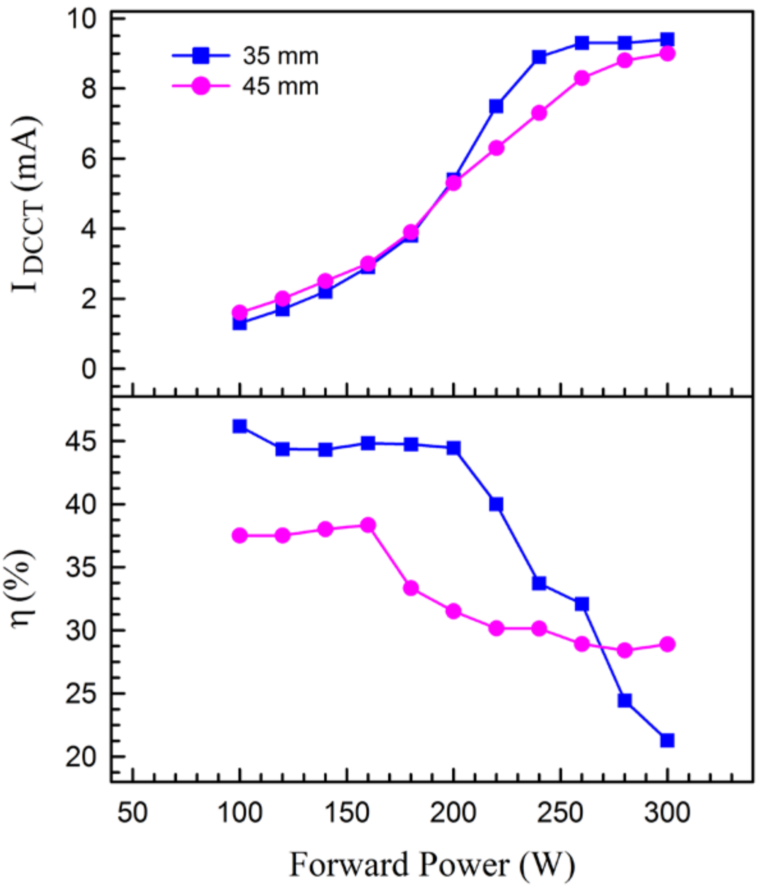

Figure 3.21: Variation of extracted beam current and proton fraction as a function of microwave power for the case of 35 mm and 45 mm inner diameter cylinders.

This higher electric field has a higher ionization probability and therefore, produces a higher amount of extracted beam current from the ion source. It can be observed in figure 3.21 that, for the case of smaller diameter cylinder, η remains nearly constant at ~ 45% upto a microwave power of 200 W and then falls rapidly as the microwave power is increased and reaches to 20% at a microwave power of 300 W. However, in the other case, proton fraction η is slightly lower ~ 37% at the low power level. It is easy to observe that fall of the proton fraction η is not so sharp with increase in microwave power as compared to the earlier case and it reaches only to ~ 28% at a power of 300 W. The variation of proton fraction with aluminium cylinder diameter possibly occurs due to the two different competing phenomenon taking place in the hydrogen plasma. The first one is related to the generation of higher electric field in the smaller diameter cylinder as compared to the other cylinder. As a consequence, high density plasma is generated, leading to a high proton fraction from the ion source. Whereas, the second phenomenon is associated with the increase in recombination rate of ions with the decrease in plasma chamber diameter as described in [46]. We believe that BN disc used in the plasma chamber reduces the recombination of ions to the wall. This is why, we are still able obtain a higher proton fraction with a 35 mm diameter aluminium cylinder as compared to the case of 45 mm diameter aluminium cylinder.

3.6 Summary

In this chapter, the 2.45 GHz Microwave Ion Source and its LEBT line have been described. The ion source has produced a beam current of 12 mA with a microwave power of 400 W at an extraction potential of 75 kV. The maximum proton fraction of ~ 70% has been obtained from the ion source after tuning different parameters of ion source such as magnetic field profile, gas flow, microwave power etc. It is observed that the extracted beam current and proton fraction for a microwave power upto 300W is comparatively higher for low gas flow settings. The experimental observation indicates that addition of water in the plasma chamber helps to increase the extracted beam current by ~ 30%. We have also performed experiments using plasma chamber of different diameter which are realized by inserting aluminium cylinder having inner diameter of 35 mm and 45 mm. The extracted beam current of ~ 10 mA is obtained in both the cases, however the plasma chamber of lower diameter yields a better proton fraction of ~ 45 % as compared to ~ 37 % , which is obtained with the larger diameter aluminium cylinder.

Chapter 4

Optimization of microwave coupling in ion source

4.1 Introduction

Microwave coupling to a plasma filled resonant cavity has been an issue of prime importance among the ion source designers, due to its deep impact on microwave ion source performance [47]. In the design of 2.45 GHz microwave ion sources, the plasma chamber radius and length dimensions are chosen to have TE_{111} resonant mode frequency at 2.45 GHz. The microwave coupling to the plasma chamber is a complex phenomenon which decides the energy transfer from the microwave generator to the plasma. The stored electric energy in the plasma chamber depends on square of the electric field set up in the plasma chamber. Thus, the coupling of microwave power to the plasma plays an important role in the production of ion beam and is, therefore, should be optimized to realize the electric field as high as possible in the plasma chamber for a given microwave power. This efficient microwave coupling produces high axial plasma density, which is one of the most crucial factors in ion source performance. Therefore, there is a huge interest in the ion source community to optimize the microwave coupling in ion sources for industrial and research applications [48-54].

The optimum coupling of the microwave power to the plasma requires a matching transformer to match the waveguide impedance with the equivalent plasma impedance. The design objective of this matching transformer is to realize a gradual impedance match between a high impedance waveguide operating in TE_{10} dominant mode and considerably low equivalent plasma impedance. At the same time the transformer is also required to enhance the electric field in the plasma chamber. As the equivalent plasma impedance is a complex dynamical quantity whose value changes as the different plasma parameters such as magnetic field, gas pressure, incident microwave power, etc. are changed, one also needs an online three or four-stub automatic tuner placed ahead of the matching transformer to minimize the reflected power under different operating conditions. Generally a double ridged multi-section binomial matching transformer is used for waveguide to equivalent plasma impedance matching. Though this type of matching transformer has been designed and operated in most of the 2.45 GHz microwave ion sources presently operating at different laboratories, but there is very little reported work on its detailed design, analysis and effect of its different dimensional parameters on the performance of the ion source.

In this chapter we present a study to improve the performance of 2.45 GHz microwave ion source described in Chapter 3. In Sec. 4.2, an analytical approach for the design and analysis of a multi-section binomial matching transformer is described. The optimization of the matching transformer in terms of microwave power transmission and electric field in the plasma chamber using full wave electromagnetic simulations are discussed in Sec. 4.3. In Sec. 4.4, we describe results of the experiments performed with the microwave ion source using two different ridged width matching transformers along with a WR 284 rectangular waveguide. Finally, in Sec. 4.5 the summary and conclusions of the research work described in this chapter are discussed.

4.2 Design and analysis of binomial matching transformer

In this section, we first describe an analytical approach to calculate the approximate physical dimensions of the various sections of the matching transformer and then an equivalent circuit model of the complete transformer using ABCD matrices of the different sections is described. Finally, the reflection and transmission characteristics of the complete transformer as obtained by cascading the ABCD matrices of different sections are discussed.

4.2.1 Analytical Approach

The main goal associated with the design of matching transformer is to adapt the waveguide impedance to the equivalent plasma impedance. This can be realized by using either a Chebyshev or a binomial matching transformer [55]. The latter one is most widely used matching transformer in the microwave ion sources worldwide, because it provides a maximally flat response in the pass band. The Chebyshev transformer provides a bandwidth much larger as compared to that of the binomial transformer, but it has finite pass band ripples. Such oscillations in the reflection coefficient are not desirable in the case of microwave ion sources as they affect the stability of the plasma [56]. Therefore, we have adopted a binomial matching transformer to gradually transform the WR 284 waveguide impedance Z_{VI} = 528 Ω (voltage-current definition of waveguide impedance) at a frequency of 2.45 GHz to the equivalent plasma impedance Z_L, which is around ~ 100 Ω as mentioned in the literature [57]. The matching transformer discussed here, is a double ridged waveguide [58] consisting of four quarter wavelength long ridge sections with constant width *s* placed opposite to each other on the top and bottom walls of the WR 284 rectangular waveguide. A sketch of the matching transformer with its dimensional parameters is shown in figure 4.1.

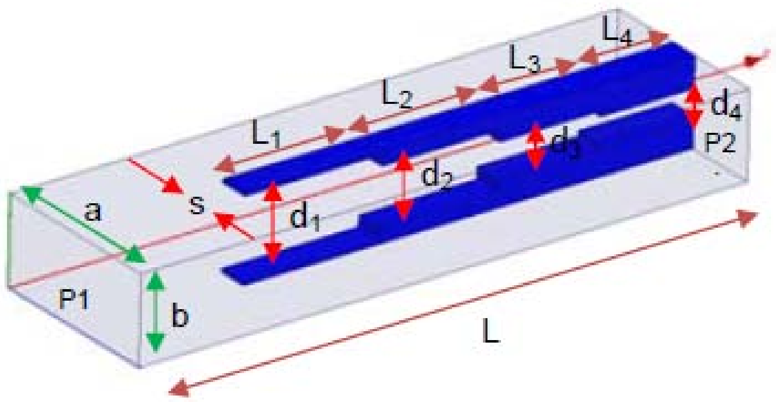

Figure 4.1: Schematic of the four section matching transformer with its dimensional parameters.

Here L_1, L_2, L_3 and L_4 represent the length of different sections and d_1, d_2, d_3 and d_4 represent the gap between the ridges of different sections in the transformer of total length L.

P1 and P2 are the input and output ports of the matching transformer whereas a and b are the usual longer and shorter sides of the WR 284 waveguide.

These impedances can be calculated using the well-known formula [59-61] given by

$$Z_{n+1} = \exp\left(\ln(Z_n) + 2^{-N} C_n^N \ln\left(\frac{Z_L}{Z_{VI}} \right) \right) \quad , \tag{4.1}$$

where n varies from 0 to $N-1$, N being the number of sections and C_n^N is the binomial coefficient. Using $Z_0 = Z_{VI} = 528\ \Omega$, $Z_L = 100\ \Omega$ and $N = 4$ for the present case, one can easily obtain the value of impedances required for the progressive transformation as $Z_1 = 476\ \Omega$, $Z_2 = 314\ \Omega$, $Z_3 = 168\ \Omega$ and $Z_4 = 111\ \Omega$. The approximate dimensions d_1, d_2, d_3 and d_4 of the corresponding sections can be obtained using the Marcuvitz's equivalent circuit formula [62] for a step change in the height of rectangular waveguide as:

$$\frac{Z_n}{Z_{n+1}} = \frac{d_n}{d_{n+1}} \quad . \tag{4.2}$$

Using $d_0 = b$ and plugging the value of impedances obtained from Eq. (4.1) into Eq. (4.2), it is straightforward to obtain the values of d_1, d_2, d_3 and d_4. These dimensions can give only initial guess and therefore, need further optimization to get the impedances of the different sections of the ridge close to the value of impedances obtained using Eq. (4.1) for progressive transformation. The impedance of a given section is given by

$$Z_0 = Z_{0\infty} \left(1 - (\lambda / \lambda_{cr})^2\right)^{-1/2} \quad , \tag{4.3}$$

where λ is the free space wavelength at 2.45 GHz and λ_{cr} is the cutoff wavelength of the respective section of the ridged waveguide. The value of λ_{cr} can be obtained using the closed form expression [63] given by

$$\lambda_{cr} = 2(a-s)\left[1+\frac{4}{\pi}\left[\left(1+0.2\left(\frac{b}{a-s}\right)^{0.5}\right)\frac{b}{a-s}\ln\left(\csc\left(\frac{\pi d}{2b}\right)\right)\right]+\left(2.45+0.2\frac{s}{a}\right)s\frac{b}{d(a-s)}\right]^{0.5}$$

(4.4)

and $Z_{0\infty}$ from,

$$Z_{0\infty} = \frac{120\pi^2(b/\lambda_{cr})}{\frac{b}{d}\sin\pi\frac{s}{b}\frac{b}{\lambda_{cr}}+\left[(2b/\lambda_{cr})\ln\csc\left(\frac{\pi d}{2b}\right)+\tan\frac{\pi}{2}\frac{b}{\lambda_{cr}}\left(\frac{a-s}{b}\right)\right]\cos\left(\pi\frac{s}{b}\frac{b}{\lambda_{cr}}\right)} \quad . \qquad (4.5)$$

Here d is the ridge gap. It is to be noted that expression given in Eq. (4.4) is valid only for the cases where $0 \le s/a \le 0.45$. Within this specified range, the cut-off wavelength λ_{cr} is almost independent of the ridged width s. Putting the ridge width s along with the already calculated dimensions d_1 to d_4 and utilizing Eqs. (4.3), (4.4) and (4.5), one can easily optimize the dimensions d_1 d_2, d_3,and d_4 to match the impedances Z_1 Z_2, Z_3 and Z_4 obtained using Eq. (4.1) for the progressive matching. The length of each section of the matching transformer which should be $\lambda_g/4$, λ_g being the guide wavelength of the respective section, can be calculated from

$$\lambda_g = \lambda\left(1-(\lambda/\lambda_{cr})^2\right)^{-1/2} \quad . \qquad (4.6)$$

In order to study the reflection and transmission characteristics, we first modeled the matching transformer with an equivalent circuit (shown in figure 4.2) and then used the well known transfer matrix technique in terms of standard ABCD parameters [64] for the analysis.

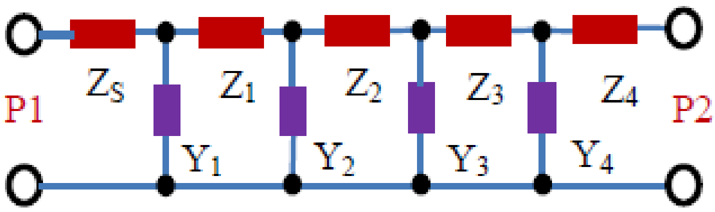

Figure 4.2: Equivalent circuit of the matching transformer.

The resultant matrix can be obtained by multiplying the matrices of the cascaded sections. Here each ridge section in the equivalent circuit is represented by a series quarter wavelength long transmission line of impedance Z and a step discontinuity between the two sections with a shunt admittance Y. The value of Y can be computed using the closed form expression [62].

$$Y = j\frac{2b}{Z\lambda_g}\ln\left(\csc\left(\frac{\pi d}{2b}\right)\right) \quad (4.7)$$

The transfer matrices **M** and **N** for the transmission line of length L ($L_1$to L_4)and admittance Y respectively can be represented as

$$\mathbf{M} = \begin{bmatrix} \cos(2\pi L/\lambda_g) & jZ\sin(2\pi L/\lambda_g) \\ \dfrac{j\sin(2\pi L/\lambda_g)}{Z} & \cos(2\pi L/\lambda_g) \end{bmatrix} \quad (4.8)$$

$$\mathbf{N} = \begin{bmatrix} 1 & 0 \\ Y & 1 \end{bmatrix} \quad (4.9)$$

The resultant transfer matrix **T** of the transformer is a cascaded product of **M** and **N** matrices belonging to different sections of the transformer and is given by ,

$$\mathbf{T} = \mathbf{N}_1\mathbf{M}_1\mathbf{N}_2\mathbf{M}_2\mathbf{N}_3\mathbf{M}_3\mathbf{N}_4\mathbf{M}_4 = \begin{bmatrix} A & B \\ C & D \end{bmatrix}. \quad (4.10)$$

The scattering parameters S_{11} and S_{21}, which provide the resultant reflection and transmission coefficients respectively, can be evaluated from [64],

$$S_{11} = \frac{AZ_L + B - CZ_SZ_L - DZ_S}{AZ_L + B + CZ_SZ_L + DZ_S} \quad (4.11)$$

$$S_{21} = \frac{2(Z_SZ_L)^{1/2}}{AZ_L + B + CZ_SZ_L + DZ_S} \quad (4.12)$$

4.3 Optimization with HFSS

As the dimensions L_1 - L_4 and d_1 - d_4 have deep impacts on the bandwidth and reflection and transmission coefficients of the transformer, the analytically estimated parameters of the transformer have been further optimized with respect to the reflection coefficient and production of electric field in the plasma chamber using ANSYS HFSS^{TM} electromagnetic simulation software [65]. We like to point out here that analytically estimated parameters of the transformer were used only for ridge widths between 6 mm to 30 mm in the code for further optimization. The transformers with ridge widths larger than 30 mm were directly optimized using the code. First a two port simulation of the matching transformer was setup in the driven modal solver of the software without the plasma chamber and the transformed impedance Z_{P2} at the port P2 was computed at 2.45 GHz for a number of ridge widths, ranging from 6 mm to 60 mm. In the next step, the matching transformer coupled to the plasma chamber was modeled in the same solver of the software and simulation was performed to calculate the distribution of electric field on the axis of plasma chamber as a function of ridge width.

Table 4.1: Parameters of the matching transformer for s = 24 mm.

Parameters	Section 1		Section 2		Section 3		Section 4	
	A	O	A	O	A	O	A	O
d (mm)	31.5	31.5	23.0	22.8	13.4	13.6	8.9	9.8
λ_{cr} (mm)	148	148	167	167	210	209	250	240
L (mm)	54.5	54.5	45.1	44.9	37.7	37.8	35.1	36.1
Z (ohm)	476	476	314	310	168	170	111	121

A: Analytic, O: Optimized

Table 4.1 shows the parameters of each section of the matching transformer for *s* = 24 mm obtained with the analytical calculations (A) and optimized (O) with the HFSS simulation code. It is easy to notice that analytically estimated parameters are very close to the optimized ones except for the ridge gap d_4 of the last section which has been optimized in the code to have electric field as high as possible in the plasma chamber. The variation of transformed impedance Z_{P2} and the magnitude of reflection and transmission coefficients $|S_{11}|$ and $|S_{21}|$ respectively for a transformer with *s* = 24 mm is shown in figure 4.3.

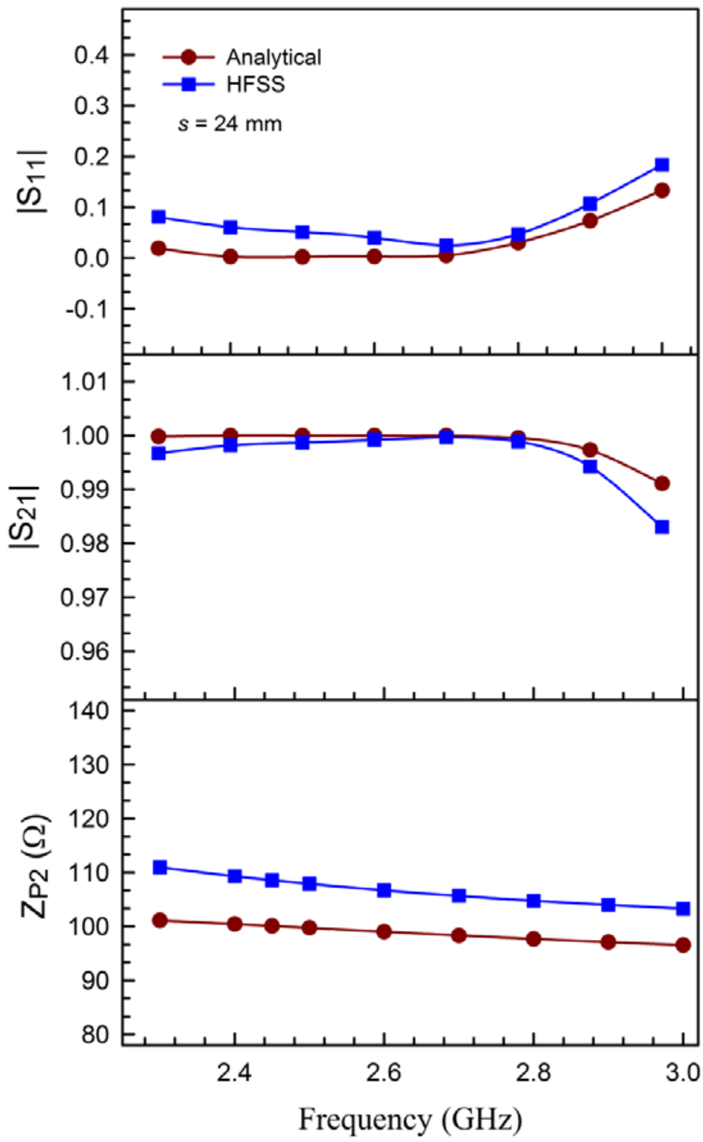

Figure 4.3: Comparison of $|S_{11}|$, $|S_{21}|$ and Z_{P2} obtained with analytical calculations and simulation performed with HFSS for matching transformer with ridge width *s* = 24 mm.

A comparison of results shows that analytical estimation is very close to the simulated values. The variations in $|S_{11}|$ (< 4%) and $|S_{21}|$ (0.2%) are very small in the vicinity of frequency band of 2.3 GHz -3.0 GHz. The matching transformer shows a flat response in this frequency band, as the variation in the transformed impedance with frequency is also very small (only 3%).

The variation magnitude of reflection coefficient $|S_{11}|$ and transmission coefficient $|S_{21}|$ of the matching transformer with frequency for different ridge widths is shown in figure 4.4. Simulation was performed with HFSS software without the plasma chamber. In the simulation all other parameters were kept at the design value.

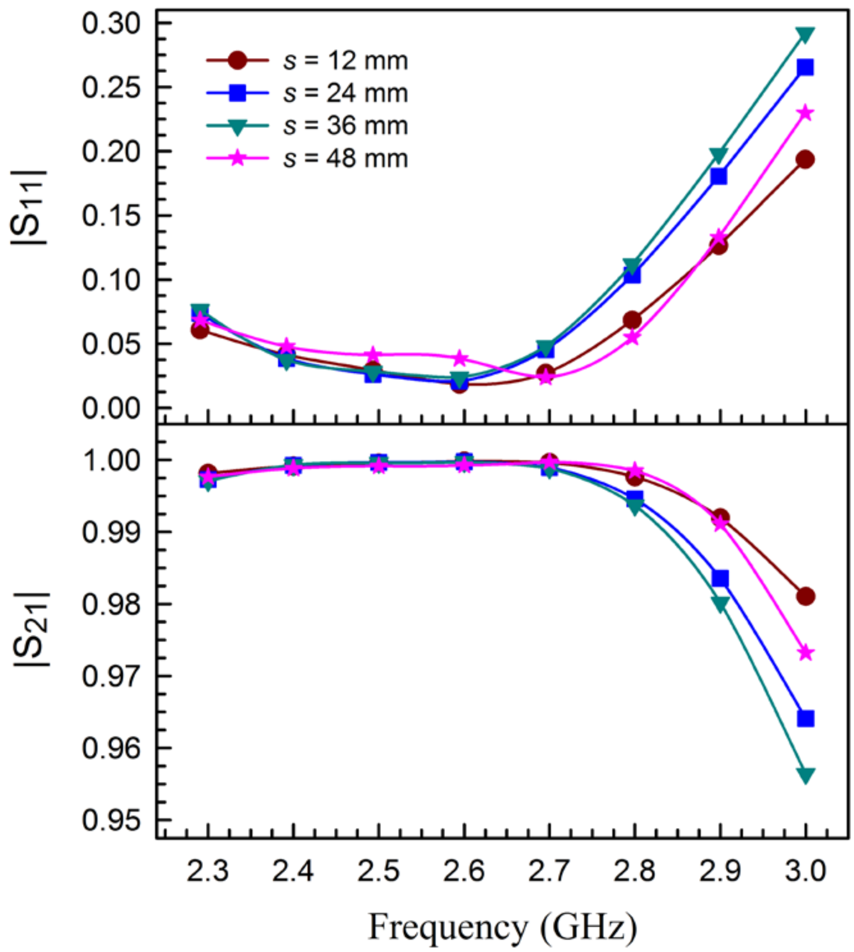

Figure 4.4: Plots of $|S_{11}|$ and $|S_{21}|$ versus frequency of matching transformer with different ridge widths.

As desired, the magnitude of S_{11} is very low and it varies less than 2% in the frequency band of interest, i.e. (2.4 GHz - 2.7 GHz). The $|S_{21}|$ is nearly unity with negligible variation in the frequency band of interest. The simulated and analytical results show a sharp change in $|S_{11}|$ and $|S_{21}|$ at frequencies above 2.8 GHz. It can be seen here that reflection and transmission coefficients are almost independent of the choice of the ridge width *s*.

We have also carried out sensitivity analysis of the reflection and transmission coefficients by varying the parameters of the matching transformer. Results of simulation are shown in figure 4.5.

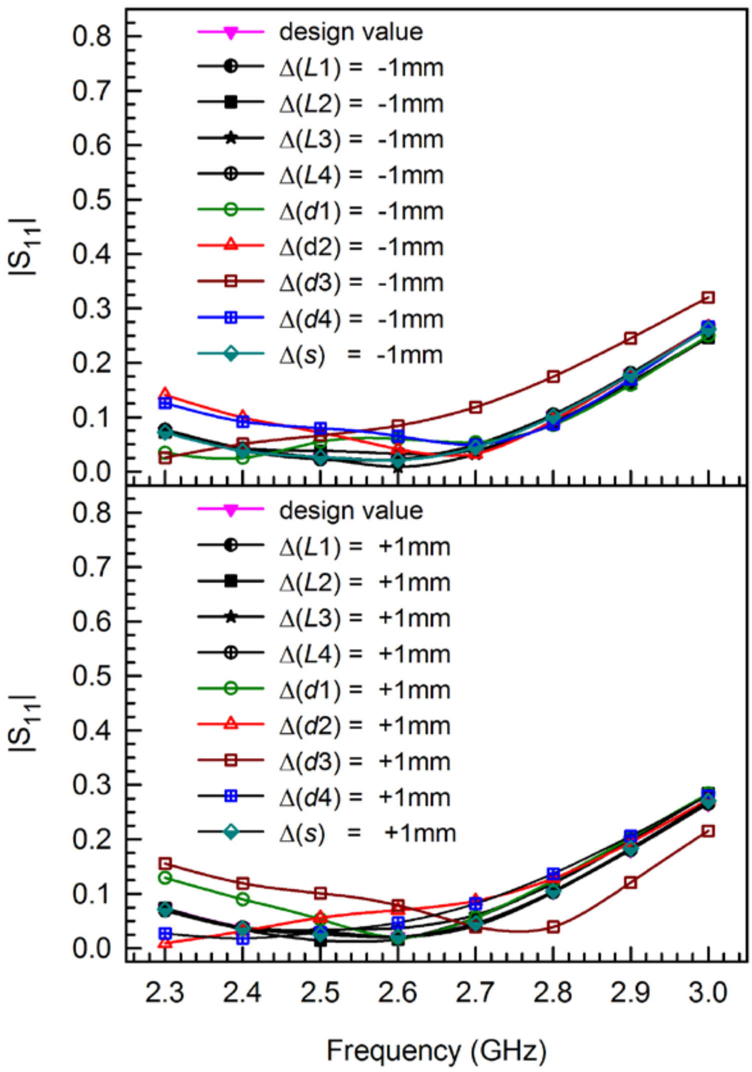

Figure 4.5: Variation of the reflection coefficient of the matching transformer with change in the dimension of different parameters by ±1 mm from the design value.

For this simulation, we have chosen the optimized design of the transformer with s = 24 mm and performed simulations by varying one parameter by ±1 mm from the design value and keeping all other parameters constant. We repeated the same procedure for all other parameters. It can be readily seen that the reflection characteristics of the matching transformer is almost unaffected by the variations of ± 1 mm in L_1, L_2, L_3, L_4 and s from the design value. We also observed a similar trend in the transmission characteristics of the matching transformer. However, the simulation result with a similar variation in the ridge gaps d_2, d_3 and d_4 from the design value shows noticeable change in the reflection and transmission coefficients. Results suggest that tolerances on the ridge widths d_2, d_3 and d_4 are very stringent as compared to the other geometrical parameters of the matching transformer.

Figure 4.6 illustrates a typical profile of the electric field produced in the plasma chamber by a matching transformer with s = 48 mm at an input microwave power of 500 W. The axial variation of the electric field in the plasma chamber for different ridge widths at 500 W of microwave power is shown in figure 4.7. A similar result has been also reported in [66]. However, we have provided an extended data of the simulated electric field as compared to [66].

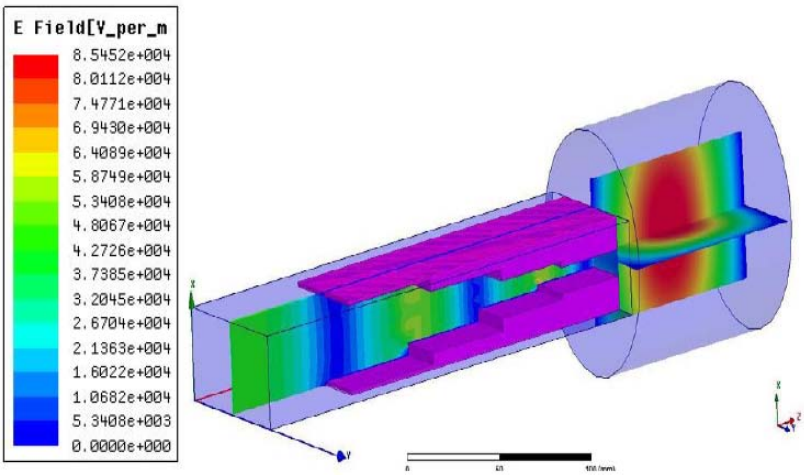

Figure 4.6: A typical electric field profile produced in the plasma chamber by an optimized matching transformer with ridge width s = 48 mm at an input microwave power of 500 W.

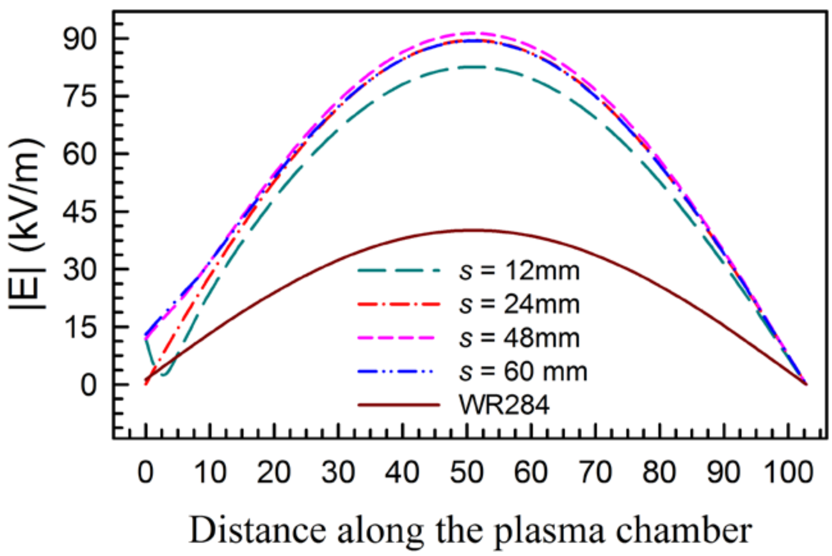

Figure 4.7: Axial variation of the electric field along the length of plasma chamber (in mm) for different ridge widths.

Simulation results show that the electric field in the plasma chamber increases as the ridge width *s* is increased, reaches to a maximum value in the vicinity of $s \sim 48$ mm and then decreases with further increase in the value of *s*. The decrease of the electric field for smaller ridge widths near the entry of the plasma chamber is mainly due to the fringe field effect which diminishes gradually as the value of *s* is increased. It is readily seen that matching transformer not only improves the electric field on the axis of plasma chamber throughout but also concentrates the field around the axis as compared to the electric field produced by WR 284 waveguide.

In figure 4.8, we have plotted the peak electric field E_{pk} at the centre of the plasma chamber and transformed impedance Z_{P2} (without plasma chamber) as a function of ridge width *s*. It is readily seen from the plot that the transformed impedance Z_{P2} at port P2 decreases with increase in the ridge width *s* whereas the peak electric field at the centre of plasma chamber increases with ridge width, reaches to a maximum value in the vicinity of (40-50) mm and then reduces as the ridge width is further increased.

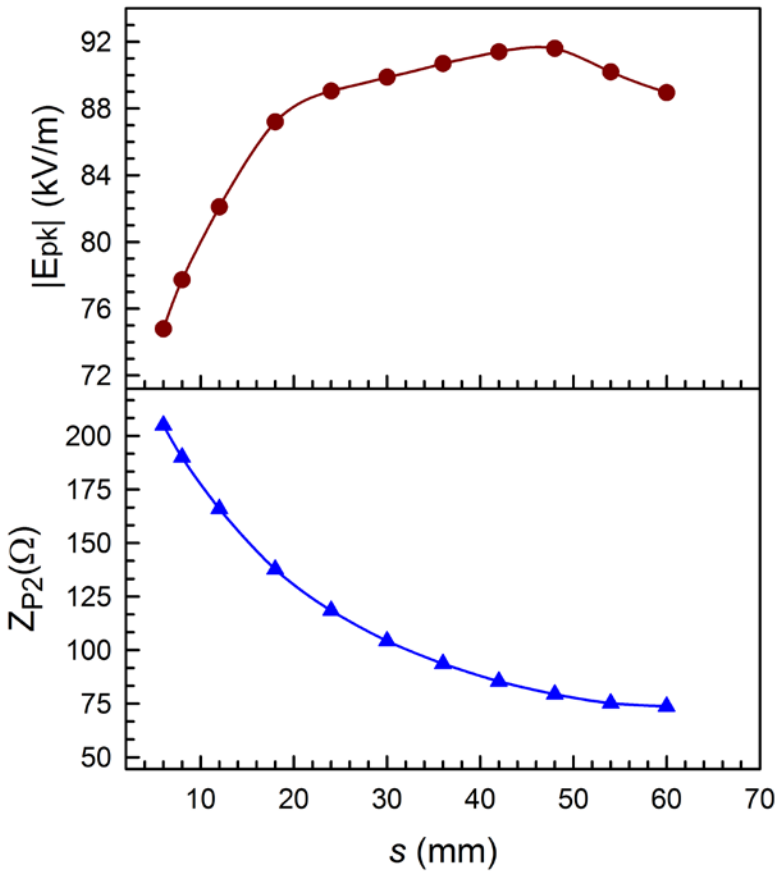

Figure 4.8: Variation of the peak electric field E_{pk} at the centre of the plasma chamber and transformed impedance Z_{P2} as a function of ridge width *s*.

As a high electric field on the axis of plasma chamber enhances the plasma density and helps in achieving higher extracted beam current, it is necessary to choose a matching transformer of ridge width in the range of (40-50) mm. However, with this choice of ridge width one gets a lower value for the transformed impedance Z_{P2} ~ (80-85) Ω, which is close to the typical equivalent plasma impedance of ~ 100 Ω.

4.4 Experimental Results

In order to characterize the matching transformer with respect to the reflection and transmission coefficients, we first fabricated two identical transformers with *s* = 24 mm and connected them back to back together with waveguide to coaxial adapters at the two ends. We then carried out two port measurements in the frequency range of (2.4-3.0) GHz using a network analyzer. Results shown in figure 4.9, indicate that the measured values of $|S_{11}|$ and $|S_{21}|$ are in close agreement with those obtained by simulation using HFSS code.

To judge the influence of matching transformers on the performance of ion source, we selected two transformers with ridge widths s = 48 mm and s = 24 mm. In the case of the first transformer (s = 48 mm) the simulated electric field at the centre of plasma chamber is ~ 91 kV/m at an input power of 500 W and the transformed impedance Z_{P2} is ~ 80 Ω, which is slightly less as compared to the typical equivalent plasma impedance of ~ 100 Ω. For the second transformer (s = 24 mm) the simulated electric field is ~ 89 kV/m slightly lower than the former transformer at the same input power but the transformed impedance Z_{P2} is ~ 108 Ω, which is comparatively close to the typical equivalent plasma impedance.

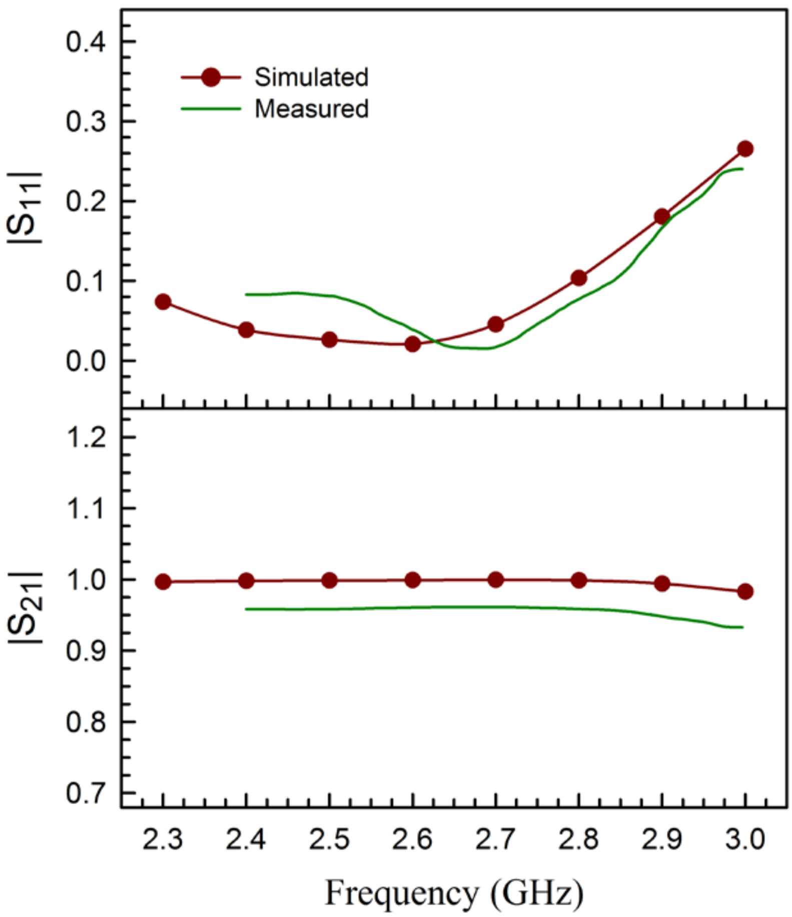

Figure 4.9: Comparison of measured and simulated $|S_{11}|$ and $|S_{21}|$ of the matching transformer with ridge width s = 24 mm.

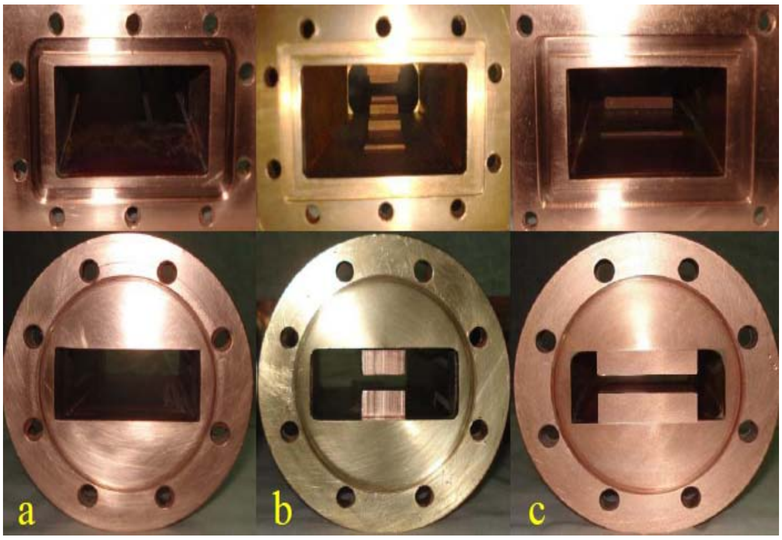

Figure 4.10: Photograph of Fabricated waveguide and matching transformer. (a) WR 284 waveguide (b) matching transformer with $s = 24$ mm (c) matching transformer with $s = 48$ mm.

These two transformers along with a WR 284 waveguide were fabricated (shown in figure 4.10), installed one by one with the ion source and experiments were performed by observing the extracted beam current and forward and reflected microwave powers.

During the whole experiment we did not change other parameters of the ion source. Typical values of source parameters used during the experiment are as follows. The gas flow was set at 0.6 sccm and the line pressure in the extraction zone was ~ 1.4×10^{-5} mbar. We used the optimized current setting of 100 A in each of the two solenoid coils of the ion source. For the centre to centre solenoid spacing (13.6 cm) used during the whole experiment, this current setting produces magnetic field of ~ 90 mT at the centre and ~ 87.5 mT at the two ends of the plasma chamber. In all the cases, proton beam was extracted at 75 kV and current was measured with DCCT as well as with the water cooled faraday cup by changing only microwave power in steps of 10 W. Results of experiment are shown in figure 4.11. In the case of WR 284 waveguide, the extracted beam current is only 1.6 mA at 100 W of forward power. At this value of forward power, a reflected power of ~ 12 W is recorded.

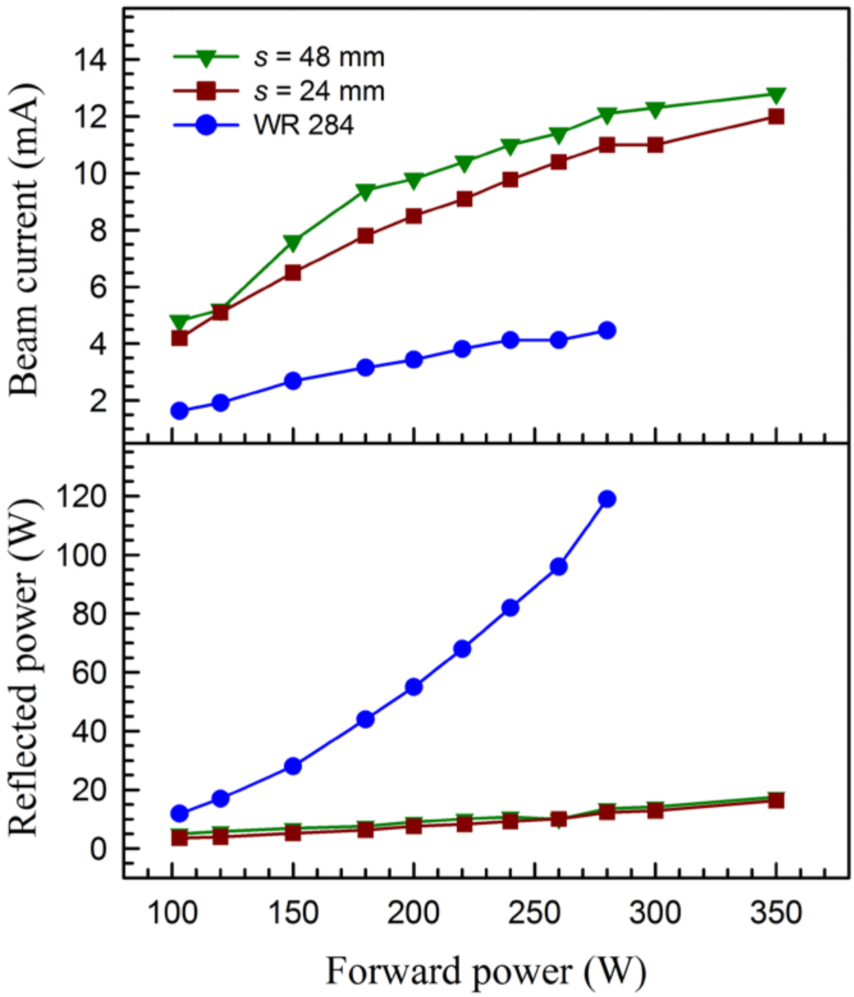

Figure 4.11: Measured extracted beam current (DCCT) and the reflected power as a function of input microwave power with different transformers.

With the increase in microwave power, the extracted beam current improves, however; at the same time we also observed a rapid increase in the reflected power, which reaches to 120 W. The extracted beam current in this case is small and only ~ 4.4 mA. This may be due to the generation of less electric field in the plasma chamber and mismatch of the WR 284 waveguide impedance to the plasma impedance.

It can be readily seen from the plots shown in figure 4.11 that the extracted beam current obtained with the transformers with ridge widths $s = 24$ mm (11 mA at 280 W) and $s = 48$ mm (12 mA at 280 W) are much higher than the current obtained with the WR 284 waveguide (4.4 mA at 280 W) at the same power level. As far as the reflected power is concerned, the performance of both the matching transformers is almost identical at all level of forward power ranging from 100 W to 350 W and is less than 5 % of the forward power. It is interesting to notice that transformer with $s = 48$ mm yields slightly more extracted beam current, which may be due to the higher electric field generated in the plasma chamber as all other parameters of the ion source are identical in both the cases. It is also expected that a transformer with large ridge width will be relatively more stable against the thermal load.

4.5 Summary

In this chapter, we have described an analytical method to design a waveguide matching transformer. Detailed simulations have been carried out to study its characteristics. 3D simulations with HFSS indicate that reflection and transmission coefficients of the matching transformer are more sensitive to the gap between the ridges of the last two sections as compared to the length and width of the ridges. The simulation results of good impedance match between plasma and waveguide has been confirmed by performing experiments using matching transformers with different ridge widths. A double ridged waveguide based matching transformer increases the extracted beam current from the ion source by a substantial amount as compared to the WR 284 waveguide under real plasma load conditions. Transformers with larger ridge widths seem to be advantageous in terms of producing high electric field and yielding more beam current output from the ion source.

Chapter 5

Space charge compensation and beam emittance measurements

5.1 Introduction

The intense beam of protons with beam current of several mA in the energy range of (20 – 100) keV is required in several high power proton accelerators [30,43,45,67]. In these accelerators, the low energy beam transport line transports and matches the beam to an upstream accelerator, typically a compact cyclotron or a Radio Frequency Quadrupole (RFQ). The transport of low energy intense beam over a long distance without any appreciable loss is difficult to achieve. This is due to the presence of nonlinear space charge force associated with a non-uniform beam distribution. The nonlinear force causes increase in the beam size, degradation of beam quality and formation of beam halos which finally lead to the beam loss.

In order to transport maximum beam current in the LEBT line, with a beam emittance within the acceptable limits of the upstream accelerator [68, 69], it is required to control the space charge forces. This can be realized by space charge compensation (SCC) of the ion beam. There are various methods to compensate the space charge associated with ion beam. However, each method has its own advantages and drawbacks. In one of the methods,a heavier gas (typically Ne, Ar, Kr, Xe etc.) is introduced into the beam-line which is ionized by the incoming beam [70]. The ejected electrons are trapped in the beam potential well, while the ionized ions are repelled in the transverse direction by the beam potential. [71-73]. This method is widely used for the space charge compensation of CW ion beams.

However, this method cannot be used to realize the space charge compensation of ion beams with sub-μs pulse duration, because of the time required to compensate the ion beam, which is typically in the order of tens of micro-seconds. Another method to achieve the space charge compensation is to inject cold electrons into the beam-line by means of an electron-emitting hot filament. In the process of space charge compensation the space charge associated with the beam is fully or partially neutralized.

Before injecting the beam into subsequent accelerating structure, it therefore, becomes necessary that high current beam from the ion source must be first characterized in terms of beam profile, emittance, etc. under the presence of appropriate gas in the beam-line. These diagnostics must be done through non-interceptive beam monitors to avoid excessive power dissipation imposed by the beam, in the case of interceptive diagnostic equipment. The non-interceptive monitors also provide true information about the beam quality degradation if any, which is generally lost in the case of interceptive diagnosis of the beam [74-75].

In this chapter, the space charge compensation and beam emittance measurements of 75 keV, 5mA proton beam are reported. This chapter is organized as follows: In Sec. 5.2 a brief description of the self fields of ion beams is described, while an overview of space charge compensation is described in Sec 5.3. In Sec. 5.4 the measurements of space charge compensation and beam emittance are reported. Results of simulation performed using KV beam envelope equation with different degree of space charge compensation in terms of rms equivalent sense and its comparison with the experimental data is discussed in Sec. 5.5. Finally, the chapter is concluded by the summary in Sec. 5.6.

5.2 Self fields of ion beams

The self fields of electric and magnetic types are generated by a charged particle beam. The self electric field is generated by the space charge associated with the beam, whereas the self magnetic field arises due to the motion of charged particle beam. Because of the coulomb repulsion between the charges of same sign in a beam, the self electric field are defocusing, whereas, the self magnetic fields are focussing. For a uniform charge density ion beam of radius *R*, beam current *I* and a constant velocity υ_b in the *z*- direction. The self electric field E_r is in the radial direction and at a distance *r*, it is given by :

$$E_r(r) = \frac{1}{2\pi\varepsilon_0 \upsilon_b} \frac{I\,r}{R^2} \quad , \text{for } r \le R \tag{5.1}$$

$$E_r(r) = \frac{1}{2\pi\varepsilon_0 \upsilon_b} \frac{I}{r} \quad , \text{for } r \ge R \tag{5.2}$$

By integrating Eq. (5.1) and Eq. (5.2), we obtain the electrostatic potential $\phi(r)$ with a boundary condition of $\phi(R_0) = 0$, where R_0 is the radius of the beam pipe.

$$\phi(r) = \frac{1}{4\pi\varepsilon_0} \frac{I}{\upsilon_z} \left(1 + 2\ln\frac{R_0}{R} - \frac{r^2}{R^2} \right), \text{for } r \le R \tag{5.3}$$

$$\phi(r) = \frac{1}{2\pi\varepsilon_0} \frac{I}{\upsilon_z} \ln\left(\frac{R_0}{r} \right), \text{for } R \le r \le R_0 \tag{5.4}$$

The self magnetic field associated with ion beam has an azimuthal component which can be found out using Ampere’s law and has a form:

$$B_\phi = \frac{\mu_0}{2\pi} \frac{I}{R^2} r \quad , \text{for} \quad 0 \le r \le R \tag{5.5}$$

$$B_\phi = \frac{\mu_0}{2\pi} \frac{I}{r}, \quad \text{for} \quad r \le R \tag{5.6}$$

Due to the electric and magnetic self fields of the beam a force $F_r = qE_r - q\upsilon_z B_\phi$ exerted on an ion moving with the beam. Using the ion beam self fields, the trajectory of a uniform beam in drift space can be expressed as:

$$\frac{d^2 r}{dz^2} = \frac{\omega_p^2}{2\beta^2 c^2} r \quad , \tag{5.7}$$

Where, ω_p is the generalized beam plasma frequency and is given as:

$$\omega_p^2 = \frac{QI}{\pi\varepsilon_0 m\beta c\gamma^3 R^2} \quad . \tag{5.8}$$

Here, Q is the ion charge state and *m* is the ion mass.

To integrate Eq. (5.7) a dimensionless parameter *K* is defined, which is commonly known as generalized perveance. It is given by:

$$K = \frac{2QI}{4\pi\varepsilon_0 m\beta^3\gamma^3 c^3} \quad . \tag{5.9}$$

The space charge is generally indicated by the generalized perveance *K* which does not change with beam diameter for a constant current and energy. It is important to note here that there is a net defocusing effect, as a result of defocusing self electric field and a focussing self magnetic field, which is generally negligible for a non-relativistic beam. The variation of beam radius along the direction of propagation of the beam in the drift space is obtained by beam envelope equation. It is given by:

$$\frac{d^2R}{dz^2} = \frac{\varepsilon^2}{R^3} + \frac{K}{R} \tag{5.10}$$

In Eq. (5.10), ε is the beam emittance and *R*(z) is the beam envelope radius varying as a function of *z*. A beam with *K* = 1 will diverge rapidly in the drift space, for example, the diameter of a parallel beam becomes double of its initial value after traversing a distance of ~ 0.7 times the initial beam diameter in the drift space. In order to understand the importance of K on beam transport, Eq. (5.9) can be reorganized as:

$$K = \frac{I}{I_0}\frac{2}{\beta^3\gamma^3} \tag{5.11}$$

With,

$$I_0 = \frac{4\pi\varepsilon_0 mc^3}{Q} \tag{5.12}$$

The characteristic current I_0 has a value of 17 kA for electrons and 31 (A/ Q) MA for ions.

The beam can be categorized as space charge dominated or emittance dominated based on the values of ε and K. It is worth pointing out here, that in the absence of (SCC) the value of K is always positive and less than or equal to 1.

5.3 Space charge compensation

Space charge associated with a beam of positive ions can be reduced with the introduction of electrons into the beam-line. The extent of space charge compensation of an ion beam is commonly estimated by a parameter known as the neutralization factor f. It is given by the ratio between positive ion and electron charge densities per unit volume. The effective generalized perveance in the case of space charge compensation is defined as:

$$K_{eff} = K\left(1-\gamma^2 f\right) \tag{5.13}$$

The parameter K_{eff} quantifies the effect of space-charge on the beam transport for a partially compensated beam. In the case of non-relativistic beam with full space charge compensation the neutralization factor f and γ are unity and as a result, the effective perveance K_{eff} becomes zero. Therefore, the space charge force does not contribute towards the radial expansion of the beam. The E_r and $\Phi(r)$ as defined by Eqs. (5.1- 5.4) gets modified with a factor $(1 - f)$ for the case of a non-relativistic space charge compensated beam. It is interesting to note that in the special case of $f = \gamma^{-2}$, K_{eff} is zero and as a result the radial force on the beam ions is also zero. This zero force condition is generally achieved for smaller values of f for electron beams as compared to ion beams.

5.4 Space charge compensation and beam profile measurement

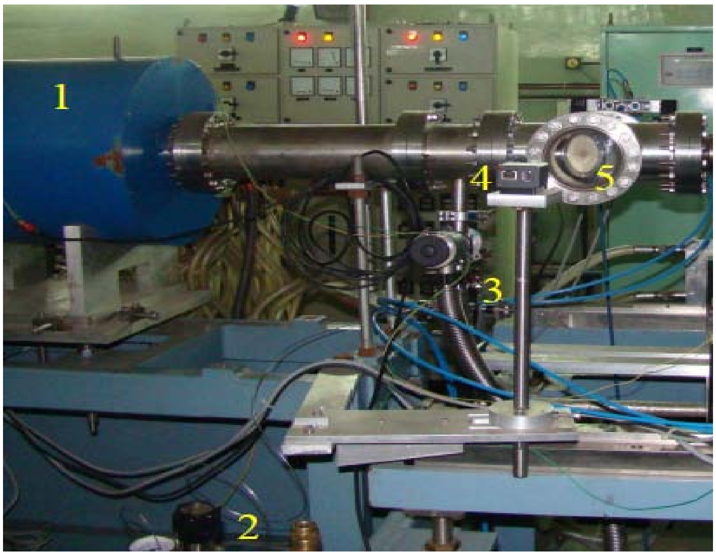

Figure 5.1: Photograph of the LEBT section where non-interceptive beam profile measurement was performed. 1. Solenoid magnet (S2), 2. Neon gas cylinder, 3. Gas dosing valve, 4. CCD camera, 5. Beam viewer installed in the diagnostic chamber.

The measurement of beam profile has been performed by introducing the controlled neon gas in the beam line and capturing the image of the beam induced fluorescence by means of a CCD camera together with a 25 mm focal length. The camera is positioned at a distance of ~ 30 cm from center of diagnostic chamber and located perpendicular to the axis of the beam in front of the view port. Before the beam profile measurement, the calibration the of the camera was done by acquiring several images of marked (5mm x 5mm) beam viewer disc located at the centre the diagnostic chamber. The resolution of this optical system (CCD camera with lens) is ~ 0.1 mm/ pixel. The background signal image without the beam is acquired at each measurement and it is subtracted from the beam signal image. A total set of 64 beam images were acquired for each value of solenoid current. The histogram of the captured image was obtained in MATLAB software. From this histogram the rms beam size was calculated for each measurement. Finally the mean value of all 64 measurements was obtained together with the standard deviation.

In addition to the measurement of beam profile through non-interceptive beam profile monitor we have also captured the beam spot on a beam viewer (water-cooled alumina plate) at different beam line pressures. The first measurement was done at a beam line pressure of $2.7 \cdot 10^{-5}$ mbar. Evidences of residual gas ionization at this pressure are given by the observation of a faint bluish violet profile which seems to be mainly due to the presence of the hydrogen and nitrogen gas in the beam-line. Subsequently the beam profiles with injection of neon gas at different leak rate were measured. With the introduction of neon gas we observed a pink fluorescence profile and found the rms beam size to decrease as the gas pressure was increased. Typical profiles of 75 keV, 5 mA proton beams at the beam-line pressures of $4.5 \cdot 10^{-5}$ mbar and $3.0 \cdot 10^{-4}$ mbar are shown in figure 5.2 (a) and 5.2 (b) respectively. The profile at $3.0 \cdot 10^{-4}$ mbar corresponds to the partially compensated condition, where we observed minimum beam size. With further introduction of neon gas, the core beam size shows increasing pattern with substantial reduction in the beam current, and it was very difficult to maintain the same experimental condition. Figure 5.2 (c) shows the typical beam spot on the water cooled alumina plate. The beam spot size measured on the water cooled alumina plate shows a core spot size ~ 1.5 times more than the rms size of the beam profile measured by capturing the image of beam induced fluorescence. The beam spot size measured using alumina plate does not reflect the true beam size due to charging of the alumina plate resulting into a larger size of the beam spot as compared to the actual one. In addition, the heating of the alumina plate by the high current ion beam also contributes in spreading the beam spot. However, the observation of beam spot on the alumina plate gives useful information about the shape of beam (round or distorted).

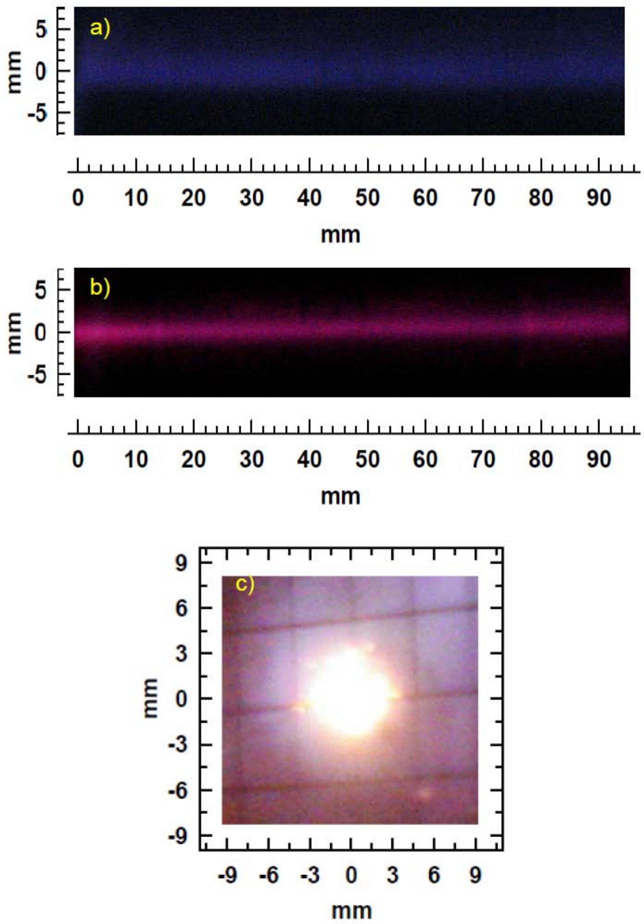

Figure 5.2: Beam induced fluorescence of 75 keV, 5 mA proton: (a) at $4.5 \cdot 10^{-5}$ mbar, (b) under neutralized conditions in the presence of Ne gas at $3.0 \cdot 10^{-4}$ mbar, and (c) a typical beam spot on water cooled gridded (5 mm × 5 mm) alumina plate.

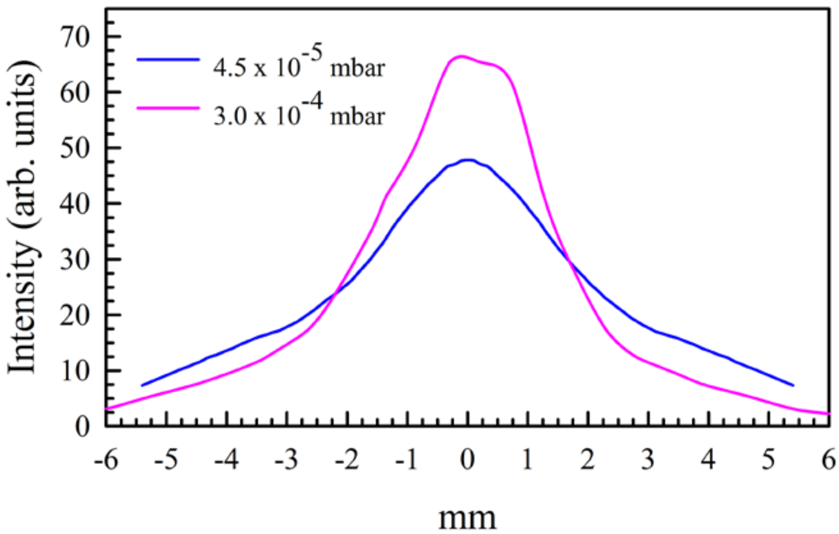

Figure 5.3: Analysed beam induced fluorescence profiles at two different gas pressures.

Figure 5.3 compares the analysed beam induced fluorescence profiles at two different values of gas pressures in the beam line. As listed in Table 5.1, the measured rms beam size at pressure of $2.7 \cdot 10^{-5}$ mbar is ~ 4.1 mm, which squeezes to 2.6 mm at the pressure of $3.0 \cdot 10^{-4}$ mbar after the introduction of Ne gas into the beam line. In the present measurement, we observed a reduction of ~ 34% in the rms beam size by utilizing the space charge neutralization with Ne gas. Table 5.1 presents the rms beam size measured using residual gas fluorescence monitor and beam viewer at different pressure in the presence of neon gas. During the measurement we did not change any parameter of the source and LEBT. Beam spots on beam viewer and profiles of beam induced fluorescence for three different values of gas pressure in the beam line are shown in figure 5.4 for comparison.

Table 5.1: Beam size at different gas pressures.

(RGF-Residual gas fluorescence, AP- Beam size on alumina plate)

Pressure (mbar)	Core size (mm) AP	rms size (full) (mm) RGF
2.7×10^{-5}	6.0	4.1 ± 0.369
4.5×10^{-5}	5.7	3.5 ± 0.122
6.0×10^{-5}	5.5	3.2 ± 0.068
7.5×10^{-5}	5.5	3.0 ± 0.044
9.0×10^{-5}	5.2	2.9 ± 0.033
1.5×10^{-4}	5.2	2.7 ± 0.031
3.0×10^{-4}	4.8	2.6 ± 0.030
5.0×10^{-4}	7.0	3.1 ± 0.032

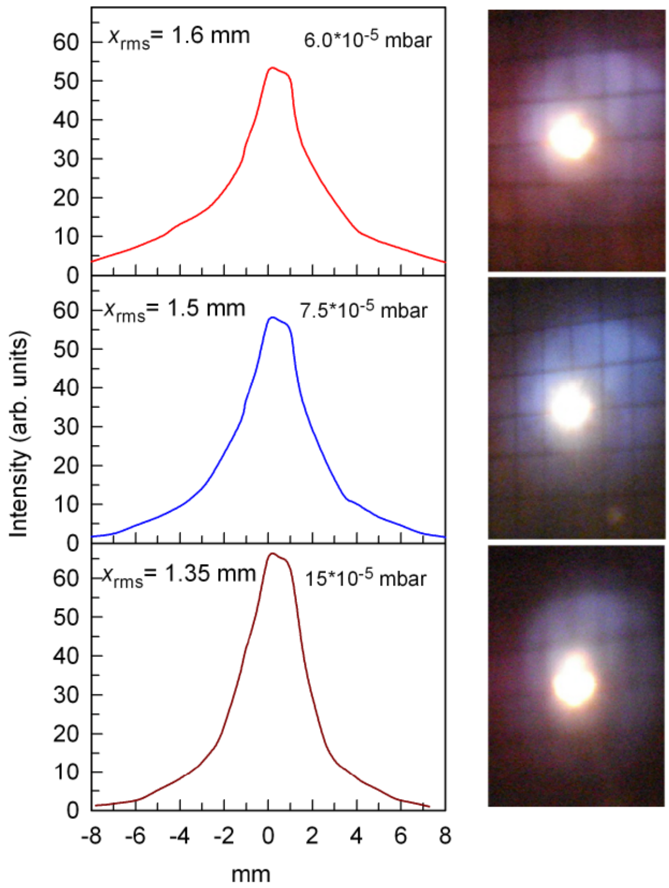

Figure 5.4: Profiles of the beam at different residual gas pressure measured with residual gas fluorescence monitor ($2x_{rms}$ represents the rms width of the profile) and the beam spot on the water cooled alumina beam viewer. The grid size is 5 mm $\times$ 5 mm.

5.5 Emittance Measurement

The rms emittance of the beam has been estimated using the well known solenoid scan method. In this method beam size is recorded at a suitable location downstream of solenoid as a function of the strength of solenoid magnet [76-78]. It is well known that this method cannot be used directly in the presence of space charge effect. The space charge contributes strongly to the beam size evolution along the drift from the scanning solenoid to the location of measurement. Thus one needs to fit the observed data using a transport code which handles the space charge effect to estimate the emittance. However, in the cases where the beam is partially neutralised, the strength of space charge force becomes negligible and beam becomes emittance dominated. In such cases the solenoid scan method can be easily utilised to estimate the emittance. Moreover, as the beam transport and matching will be done to the subsequent accelerator only with the space charge compensated beam, it is practical and more appropriate to know the beam emittance under space charge compensation for performing matching calculations.

In the present experiment we kept the beam line pressure at fixed value of $3.0 \cdot 10^{-4}$ mbar where we observed the beam size to a minimum value. The operating parameters of the ion source were following; microwave power = 400 W, extraction region gas pressure: $2.0 \cdot 10^{-5}$ mbar, current in injection and extraction coils = 103A in each, extraction voltage = 75 kV, current in solenoid-1 = 106 A, current in solenoid-2 = 110 A, beam line pressure with neon gas = $3.0 \cdot 10^{-4}$ mbar, drain current in HVPS = 13.6 mA, DCCT current = 12 mA, Faraday cup current = 5mA. We then measured the profiles using the CCD camera for several settings of current in the solenoid magnet S2. The range of current in the solenoid is chosen in such a way that beam size goes through the waist during the scan. As the extraction system as well as the entire beam transport system is radially symmetric, we have measured the emittance only in one plane. It is expected that it will be same in the other plane.

The analysis of the measured data has been performed using the well known sigma matrix method. If $\boldsymbol{\sigma}_0$ be the beam matrix at the entrance of solenoid magnet and $\boldsymbol{\sigma}$ be the beam matrix at the location of beam profile monitor, then

$$\boldsymbol{\sigma} = \mathbf{R}\,\boldsymbol{\sigma}_0\,\mathbf{R}^T \quad . \tag{5.11}$$

with

$$\boldsymbol{\sigma} = \begin{bmatrix} \sigma_{11} & \sigma_{12} \\ \sigma_{12} & \sigma_{22} \end{bmatrix} = \begin{bmatrix} < x^2 > & < xx' > \\ < xx' > & < x'^2 > \end{bmatrix}. \tag{5.12}$$

Here **R** is the transfer matrix from the entrance of the solenoid magnet to the location of beam profile monitor. The bracket <> represents the average taken over the whole beam distribution with position x and divergence x'. From Eq. (5.11) it is easy to get square of half rms width of the profile as

$$\sigma_{11} = \langle x^2 \rangle = \sigma_{011} R_{11}^2 + 2\sigma_{012} R_{11} R_{12} + \sigma_{022} R_{12}^2 \quad . \tag{5.13}$$

It is clear from Eq. (5.13) that one needs only three different values of σ_{11} to deduce the three unknowns of beam matrix $\boldsymbol{\sigma}_0$. To get rid of statistical errors, one generally needs many more points and fits the data with Eq. (5.13) to obtain the value of the elements of beam matrix $\boldsymbol{\sigma}_0$ and the value of rms emittance from

$$\varepsilon_{rms} = (\sigma_{011}\sigma_{022} - \sigma_{012}^2)^{1/2} \quad . \tag{5.14}$$

It is basically the square root of the determinant of the beam matrix $\boldsymbol{\sigma}_0$. The trace space area is $\pi\varepsilon_{rms}$. In the case of thin lens approximation for solenoid, the transfer matrix **R** for the present case is given by :

$$\mathbf{R} = \begin{pmatrix} 1 & L \\ 0 & 1 \end{pmatrix} \cdot \begin{pmatrix} 1 & 0 \\ -\dfrac{1}{f_{sol}} & 1 \end{pmatrix} \quad , \tag{5.15}$$

where L is the distance between the thin lens (~ middle of the solenoid) and the location of measurement. The term f_{sol} is the focal length of the solenoid under the thin lens approximation. It is given by

$$\frac{1}{f_{sol}} = \left(\frac{qB_0}{2mc\beta\gamma}\right)^2 l_e = k_0^2 l \quad , \tag{5.16}$$

Here, B_0 is the peak axial magnetic field, k_0 and l are the strength and effective length of the solenoid, q and m are the charge and mass of the particle under consideration, c is the speed of light and β and γ are the usual relativistic factors related with the velocity and energy of the particle.

In the case of hard edge solenoid of length l, the transfer matrix **R** is given by

$$\mathbf{R} = \begin{pmatrix} 1 & L \\ 0 & 1 \end{pmatrix} \cdot \begin{pmatrix} \cos k_0 l & \frac{1}{k_0} \sin k_0 l \\ -k_0 \sin k_0 l & \cos k_0 l \end{pmatrix} \quad . \tag{5.17}$$

Figure 5.4 shows the variation of $< x^2 >$ of the beam profile as a function of current in the solenoid magnet. Filled circles represent the measured data points. As expected, $< x^2 >$ has a parabolic dependence on the solenoid current. The full curves represent the least square fit to the measured data using Eq. (5.13). First we have analysed the data considering the solenoid magnet as a thin lens of focal length f_{sol} given by Eq. (5.16). The distance L is measured from the middle of the solenoid magnet as indicated in Figure 5.5 (a). In the second analysis solenoid is considered as a hard edge magnet by employ the **R** matrix given by Eq. (5.17). Result of least square fit is shown in Figure 5.5 (b). Here the distance L is measured from the end of the solenoid magnet of length l. The value of magnetic field B_0 used in the calculation is obtained from the measured axial field data at the centre of solenoid as a function of current I using a hall probe.

The errors in the parameters and correlations between them are also obtained from the fit to estimate the standard deviation of the emittance using the following formula [76-79].

$$\delta\varepsilon = \frac{1}{2\varepsilon_{rms}} \left(r_1^2 \delta r_2^2 + r_2^2 \delta r_1^2 + 4 r_3^2 \delta r_3^2 + \mathrm{cor}_1 + \mathrm{cor}_2 + \mathrm{cor}_2 \right) \quad . \tag{5.18}$$

with, $\mathrm{cor}_1 = -4 r_1 r_3 r_{32} \delta r_3 \delta r_2$, $\mathrm{cor}_2 = 2 r_1 r_2 r_{12} \delta r_1 \delta r_2$, $\mathrm{cor}_3 = -4 r_2 r_3 r_{13} \delta r_1 \delta r_3$.

where, $r_1 = \langle x^2 \rangle$, $r_2 = \langle x'^2 \rangle$, $r_3 = \langle x x' \rangle$ and r_{ij} are the coefficients of correlation.

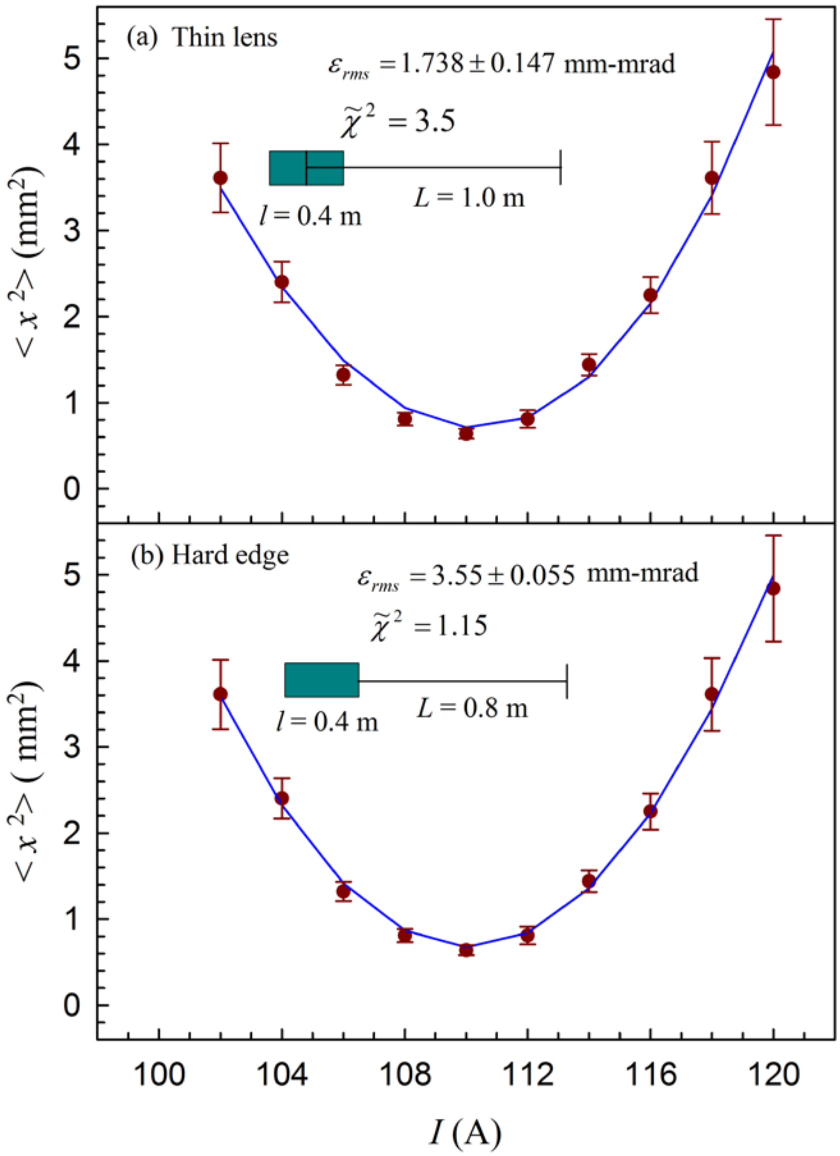

Figure 5.5: Variation of the measured $<x^2>$, square of half rms width of the beam profile as a function of the current in the solenoid magnet. The full curves represent the least square fit to the measured data. Here $\tilde{\chi}^2$ represents the reduced chi square value obtained from the fit.

We obtained the value of rms emittance $\varepsilon_{rms} = 1.738 \pm 0.147$ mm-mrad by using thin lens approximation and $\varepsilon_{rms} = 3.55 \pm 0.055$ mm-mrad considering solenoid as a hard edge magnet. It should be noted that calculation with thin lens approximation underestimates the rms emittance. This may be due to fact that the effective length of solenoid (40 cm) is not negligible as compared to the drift length of 80 cm.

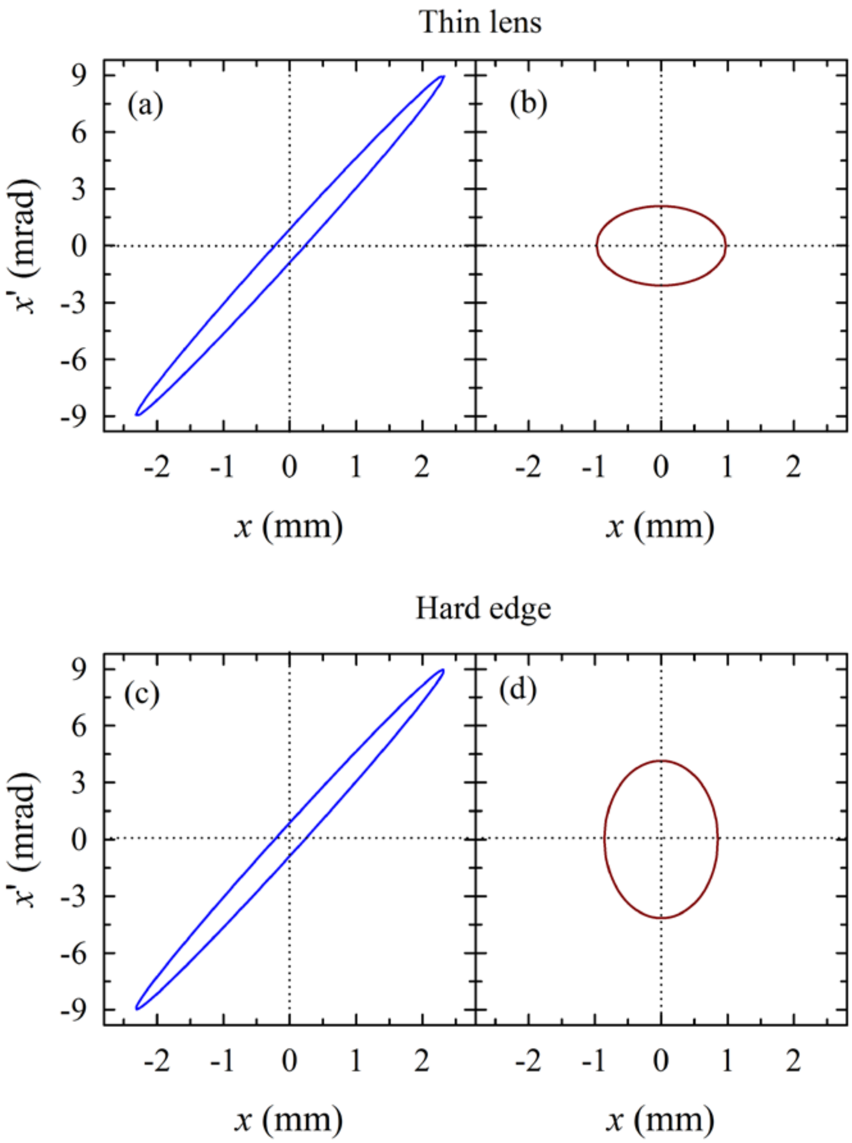

Figure 5.6: Orientation of the beam phase ellipses at the entry of the solenoid and at the profile monitor location for current setting corresponding to waist.

We like to point out here that the result with hard edge solenoid is more accurate and appropriate. This value corresponds to a normalized rms emittance $\varepsilon_{n\,rms} = \beta\gamma \cdot \varepsilon_{rms} = 0.046$ mm-mrad. Figure 5.6 (a) - 5.6 (d) show the orientation of the beam phase ellipses at the middle of the solenoid and at the location of profile monitor obtained from analysis of the data. Upright ellipses shown in Figure 5.6 (b) and 5.6 (d) correspond to the current setting in solenoid S2 for formation of waist at the location of measurement.

The normalized rms emittance $\varepsilon_{n\,rms}$ of the beam from the microwave ion source is estimated using the Eq. (2.23). For R_{ex} = 3.0 mm and B_{ex} = 87.5 mT, the estimated normalized rms emittances $\varepsilon_{n\,rms}$ (mm-mrad) of proton beam are 0.047, 0.058 and 0.076 at ion temperatures $k_B T_i$ (eV) equal to 0.5, 1.0 and 2.0 respectively. The experimentally measured value of the normalised rms emittance is very close to the first estimation and indicates that ion temperature in the plasma is ~ 0.5 eV.

5.6 Simulation

In order to have some information about the variation of beam size with solenoid current in the presence of space charge compensation we have performed transport simulation using envelope equation. It is well known that beam from the ion source differ from the uniform distribution and beam particle distribution undergoes an evolution from the source to the point of measurement. However, if one is not interested about the details of such evolution of distribution and concerned only about the evolution of envelope, then beam can be interpreted in rms equivalent sense in terms of equivalent Kapchinsky-Vladimirsky (KV) beam [80-82]. Thus, for any distribution an equivalent KV distribution can be defined and the envelope equation for the evolution of two times rms beam envelope i.e. $X = 2\left\langle x^2 \right\rangle^{1/2}$ for the axial symmetric beam can be written as:

$$X'' + k^2(s)X - \frac{2 \cdot I(1-f_e)}{I_0 \beta^3 \gamma^3 X} - \frac{\varepsilon^2}{X^3} = 0 \qquad (5.20)$$

.

Here prime means that derivative is taken with respect to s, the axial coordinate along the direction of beam propagation. In the simulation we have used hard edge approximation for the solenoid with effective length l = 40 cm and strength $k(s) = k_0$ (defined in Eq. (4.16)) in the solenoid and $k(s) = 0$ in the drift. I is the beam current, f is the neutralization factor and I_0 is the characteristic current. The quantity $\varepsilon = 4 \cdot \varepsilon_{rms}$, called the edge emittance, and is assumed to remain constant during the transport of beam.

Figure 5.7 shows the layout of LEBT with locations of slit, solenoids and viewing port where profile measurement was performed. The portion of the beam line used for study space charge compensation is marked with SCC region. The evolution of rms beam envelope at $f = 0.2$ and $f = 0.8$ with $\varepsilon_{rms} = 3.55$ mm-mrad and $I = 5$ mA is also shown for comparison. In the simulation solenoids S1 and S2 are adjusted to form first waist at the slit location and second waist at s = 302cm, the location of measurement.

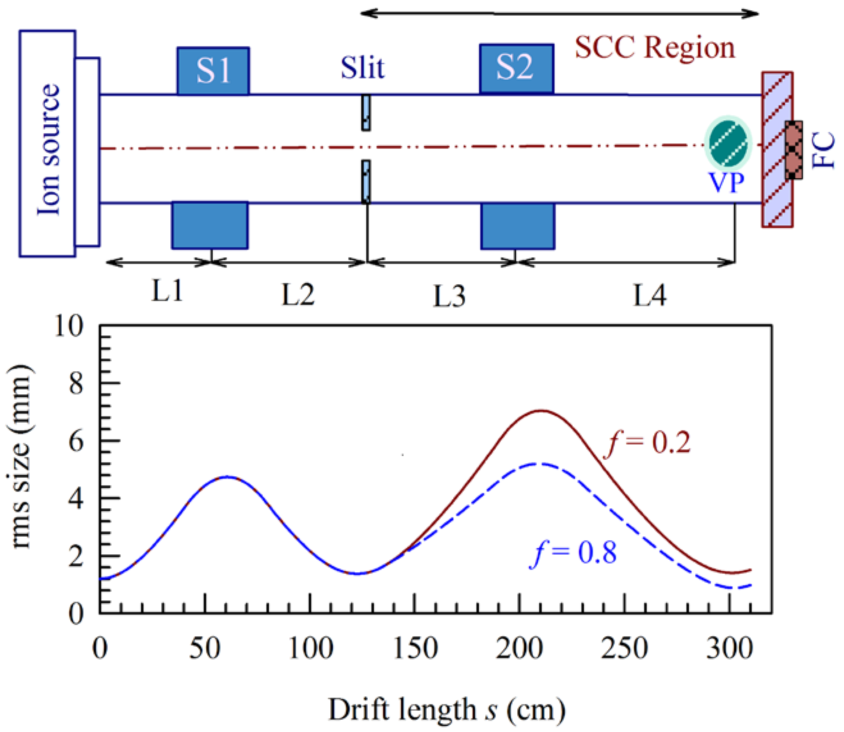

Figure 5.7: Schematic of LEBT indicating the space charge compensation (SCC) region, Viewing port (VP), Faraday cup (FC) and solenoids S1 and S2. Evolution of rms beam envelops at f= 0.2 and f = 0.8 are also shown.

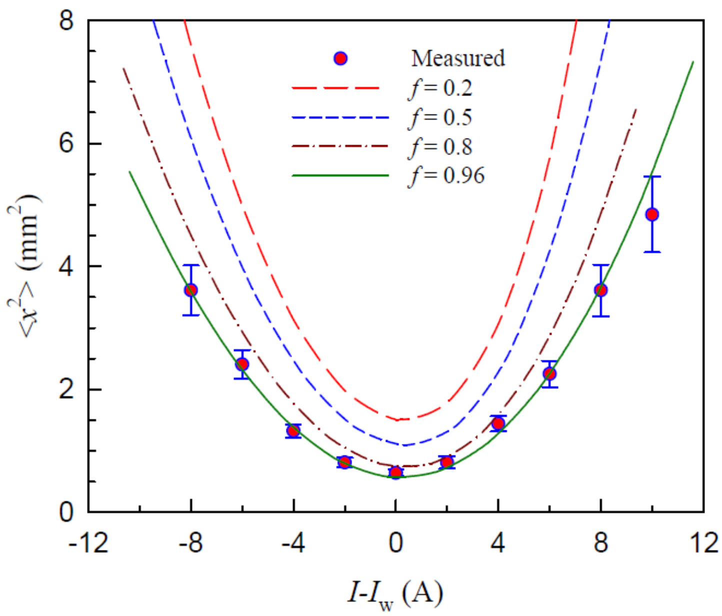

Figure 5.8: Variation of $<x^2>$ as a function of solenoid current for different f values.

Current in solenoid S1 is kept at the same value throughout while current in solenoid S2 is adjusted for different f to form waist at s = 302cm. In Figure 5.8 we have shown the simulated values of $<x^2>$ at s = 302 cm as a function of solenoid current for four different values of neutralization factor f. As the range of solenoid current changes with f, we shown the plots centred with respect to I_w, the current required in the solenoid to form waist at s = 302 cm for a given f. It is evident from the plot that all the curves are symmetric around the waist and widen as the effect of space charge reduces with increase in the neutralization factor. The curve with f = 0.96, which is obtained after performing simulations at several f values, is very close to the experimentally observed data. We like to point out here that at f = 0.96, the beam is highly emittance dominated in the region of interest i.e. the fourth term in Eq. (5.20) is very large as compared to third term. Thus simulation validates our experimental result of emittance measurement.

5.7 Summary

We have studied the space charge compensation using proton beam of 5 mA at 75 KeV, and measured its effect on the beam size using interceptive as well as non-interceptive methods. The beam spot size measured on the water cooled alumina plate shows a core spot size ~ 1.5 times more than the rms size of the beam measured by capturing the beam induced fluorescence using CCD camera. In this measurement we have observed a reduction of ~ 34% in the rms beam size by utilizing the space charge neutralization with neon gas. The background near the core is mostly due to neutrals and unwanted species. We have also measured the rms emittance of the beam under the neutralised condition using the solenoid scan method and analyzed the data using hard edge approximation of the solenoid. The measured rms emittance is very close to the estimation and indicates that ion temperature in the plasma ~ 0.5 eV. The simulation performed using rms equivalent KV beam validates our experimental result of emittance measurement.

Chapter 6

Conclusions and Future Works

6.1 Conclusion

In this thesis, theoretical and experimental studies related with the performance improvement of 2.45 GHz Microwave Ion Source and characterization of high current proton beam under space charge compensation regime is discussed.

A beam current up to 12 mA has been extracted with a microwave power of 400 W at an extraction potential of 75 kV. Proton fraction up to ~ 70% was generated at different settings of ion source operating parameters like, for instance, gas flow and microwave power. The measured variation of total extracted beam current and proton fraction with these two parameters has been explained by the reasoning that the electron temperature changes with a change in either of the parameters and thus affecting the rate of ionization in the plasma.

The performance of Microwave Ion Source has a direct linkage with the coupling of microwaves to the plasma. This fact motivated us to investigate the microwave coupling issues aimed to improve the performance of the ion source, in terms of minimum reflected power and enhancement of electric field in the centre of plasma chamber. We have formulated an analytical method to design a waveguide coupling transformer based on a double ridged waveguide. 3D simulations in HFSS software were carried out to study the transformer characteristics as a function of its different physical dimensions. Results of these simulations indicated that reflection and transmission characteristics of the transformer are more sensitive to the gap between the ridges of the last two sections as compared to the length and width of the ridges. The enhancement of electric field in the plasma chamber due to different ridged width transformer were also calculated and found to be more than two times in the case of transformers with ridged width in the range 24 mm- 48 mm as compared to the simple WR 284 waveguide. The results of the simulations are tested by comparing the measured reflected power and extracted beam current for WR 284 waveguide, 24 mm ridged width transformer and 48 mm ridged transformer. The result of measurements clearly indicates that the increase in the extracted beam current is due to the high electric field induced into the plasma chamber as a result of better microwave coupling provided by the two ridged waveguide transformers as compared to WR 284 waveguide.

We experimentally investigated the performance of ion source with the introduction of different diameter aluminium cylinder into the plasma chamber. We observed that plasma is formed in both the aluminium cylinders having inner diameter of 35 mm and 45 mm respectively. Almost similar beam currents have been extracted in the case of two cylinders. The extracted beam current reached upto ~ 10 mA with a microwave power of 300 W. However, a significant difference in the proton fraction corresponding to both the cylinders was observed. A proton fraction of ~ 45% was produced in the case of smaller cylinder, while the larger cylinder reached to ~ 37 %. The probable reason of this variation was linked to the dependence of ion recombination rate with the cylinder wall as well as to the generation of higher electric field in the smaller diameter aluminium cylinder.

It is well known that the space charge force associated with the high perveance beams is the main cause of beam-blow up and can also induce emittance growth under certain conditions. However, the deleterious effects of space charge can be counteracted by introducing space charge compensation into the beam-line. This fact motivated us to study the effects of space charge compensation on the proton beam and measure its rms beam emittance in the regime of space charge compensation.

In the first step, the rms beam size of 75 keV, 5 mA proton beam has been measured by a non-interceptive profile monitor at different beam line pressure, arising due to the Neon gas injection in the beam line. It is found that the introduction of space charge compensation by Neon gas injection in the beam line can reduce the rms beam size of 75 keV, 5 mA proton beam upto ~ 34 %. Furthermore, the normalized rms emittance of space charge compensated proton beam is obtained using the well known solenoid scan method. The value of the measured normalized rms emittance is ~ 0.05 mm-mrad, which is much below 0.2 mm-mrad as required for high current beam acceleration in a RFQ or a compact cyclotron.

6.2 Future works

The research work described in this thesis is of key importance in the performance improvement of 2.45 GHz Microwave Ion Sources and characterization of space charge compensated high current proton beams. However, some additional issues related to the performance improvement of 2.45 GHz Microwave Ion Sources and dynamics of space charge compensated high current ion beams are still required to be investigated.

In the operation of ion source we learned that in the event of a high voltage spark near the extraction region the majority of electronic components kept on the high voltage deck are tripped or failed leading to a beam interruption from the ion source. These sparks are generally triggered by the penning discharge taking place at a low value of residual magnetic field of (~ 100 - 200 G) in the region between suppressor electrode and ground electrode. In order to achieve high beam availability and reliability of the ion source the redesign of magnetic system will be taken up in the near future. The goal of the new design will be to achieve a low residual magnetic field (< 50 G) in the extraction region; the most preferred option to meet this requirement is to design a permanent magnet based magnetic system. In addition, most of the components of the ion source placed on the high voltage deck should be placed on ground potential. This requires a waveguide break to be introduced into the microwave line of the ion source able to operate at 100 kV and 500 W of microwave power.

The influence of nearly full space-charge compensation on the proton beam quality for a total current of 5 mA has been presented in Chapter 5. However, the effect of space-charge compensation on beam quality, at different beam currents and for different degree of space charge compensation at a single value of beam current are still not very well understood. Therefore a detailed study of the effects of space charge compensation on beam quality with respect to beam current, degree of space charge compensation, residual gas composition will be carried out in the near future.

Bibliography

[1] F. H. Bohn, K. Bongardt, F. Carsughi, A. Claver, K. Klausen, C. Desailly, P. Fabi, I. Gardner, C. Hake, Laclare, J.-L., S. Palanque, D. Richter, and H. Tietze-Jaensch, Technical Report, Vol III, ESS Council, 2002.

[2] A. Mosnier, *Proceedings of the Linear Accelerator Conference LINAC 2008*, Victoria, Canada, FR201, pp. 1114-1118,2008.

[3] J. Alonso et al., *arXiv:*1210.3679, 2012.

[4] J. Alonso et al., *JINST* **10**, T10003, 2015.

[5] J.-L. Biarrotte, A.C. Mueller, H. Klein, P. Pierini, D. Vandeplassche , *Proceedings of the Linear Accelerator Conference LINAC 2010*, Tsukuba, Japan, TUP020, pp. 440-442, 2010.

[6] P.K. Nema, P. Singh, P. Satyamurthy, S.B. Degweker, V.K. Handu, *Proceedings of International Topical Meeting on Nuclear Research Applications and Utilization of Accelerators*, Vienna, Austria, ADS/INT-03, 2009.

[7] R. Geller. *Electron Cyclotron Resonance Ion Sources and ECR Plasmas*. Institute of Physics Publishing, Bristol, UK, 1996.

[8] I. G. Brown, *The Physics and Technology of Ion Sources*, Wiley-WCH, 2nd edition, 2004.

[9] T. Thuillier, *Lecture Notes of JUAS*, Archamps, France, Jan-Mar 2015, https://indico.cern.ch/event/356897/contribution/212/attachments/709946/974546/particlesource_lecture_2015 - Add_On.pdf, accessed on: Nov, 2015.

[10] C.D. Child, *Phys. Rev.* (Ser. 1), **32**, 492, 1911.

[11] I. Langmuir and K.T. Compton, *Rev. Mod. Phys*. **3**, 251, 1931.

[12] S. R. Lawrie, D. C. Faircloth, A. P. Letchford, C. Gabor, and J. K. Pozimski, *Rev. Sci. Instrum.* **81**, 02A707, 2010.

[13] Claude Lejeune and Jean Aubert, *Emittance and Brightness: Definitions and Measurements*, *Advances in Electronics and Electron Physics*, Supplement 13A, Academic Press,1980.

[14] K. Floettmann, *Phys. Rev.ST Accel. Beams*. **6,** 034202, 2003.

[15] J. Buon, *Lecture Notes of CAS-CERN Accelerator School: 5th General Accelerator Physics Course*, Jyvaskyla, Finland, pp.89-116, Feb, 1992.

[16] M.A. Leitner, D.C. Wutte, and C.M. Lyneis, *Proceedings of Particle Accelerator Conference*, Chicago, USA, MOPB004, 2001.

[17] J.D. Lawson, *The Physics of Charge-Particle Beams*. Clarendon Press, Oxford, 1988.

[18] Jr. Stanley Humphries, *Principles of Charged Particle Acceleration*. John Wiley and sons, New York, 1999.

[19] B. Wolf, *Handbook of Ion Sources,* CRC Press, Boca Raton, 1995.

[20] L. Celona, *arXiv*:1411.0538v1, 2014.

[21] P.W. Schmor, *Proceedings of the 19th International Conference on Cyclotrons and Their Applications 2010*, Lanzhou, China, FRM2CIO01, 2010.

[22] A.J. Dempster, *Phys. Rev*. **11**, 316, 1918.

[23] L.R. Maxwell, *Rev. Sci. Instrum*. **2**, 129, 1931.

[24] F.M. Penning, *Physica* **IV** (2), 71–75, 1937.

[25] E.D. Donets, *AIP Conference. Proceedings*,**274**, 663, 1993.

[26] N. Sakudo, *Rev. Sci. Instrum*. **49**, 940, 1978.

[27] J. Ishikawa, Y. Takeiri and T. Takagi, *Rev. Sci. Instrum*. **55**, 449, 1984.

[28] Y. Cho , D. Kim, H.S. Kim, K.T. Seol and H.J. Kwon, *JKPS*, **63**, 11, 2013.

[29] Gas regulating valve, https://www.pfeiffervacuum.com/productPdfs/PFI39931.en.pdf, accessed on: Oct, 2015.

[30] T. Taylor, and John S.C. Wills, *Nucl. Instrum. Methods Phys. Res. A*.**309,** 37, 1991.

[31] T. Taylor, and J. F. Mouris, *Nucl. Instrum.Methods Phys. Res. A*.**336,** 1, 1993.

[32] E. Fagotti, A. Palmieri and X. Ren, *Rev. Sci. Instrum*. **79**, 02B306, 2008.

[33] P.Sing Babu, A. Goswami, and V. S. Pandit, *Phys. Plasmas* **20**, 083110, 2013.

[34] P. Forck, *Lecture Notes of JUAS*, Archamps, France, Jan-March 2011. http://www-bd.gsi.de/conf/juas/juas_script.pdf, accessed on: Oct, 2015.

[35] R.C. Weber, *AIP Conference Proceedings*, **333**, pp. 3–23, 1995

[36] R.C. Weber, *AIP Conference Proceedings*, **546,** 2000

[37] SeonYeong Noh , Se Duk Chang, Tae-Keun Yang Ji-Gwang Hwang, and Ga Ram Hahn, *Proceedings of IBIC2015*, Melbourne, Australia, TUPB043, 2015.

[38] A. Aryshev, T. Aumeyr, G.A. Blair, S.T. Boogert, G. Boorman, A. Bosco, L. Corner, A.E. Dabrowski, L. Deacon, B. Foster, A. Gillespie, E.B. Holzer, S. Jamison P. Karataev, T. Lefevre, K. Lekomtsev, M. Olvegard, S. Mallows, M. Micheler, L. Nevay, M. Sapinski, S. Smith, L. Soby, R. Walczak, C. Welsch, M. Wendt, Conceptual design report, CLIC Project,2015.

[39] K. Unser, *IEEE Trans. Nucl. Science*, Vol**NS-16**, No. 3, pp. 934-938, 1969.

[40] H. Appelo, M. Groenenboom, J. Lisser, *IEEE Trans. Nucl. Science*, Vol**NS-24**, No. 3, pp. 1810-1811, 1977.

[41] Bergoz Instrumentation, http://www.bergoz.com, accessed on: Nov, 2015.

[42] MATLAB software, http://www.mathworks.com, accessed on : Nov, 2015.

[43] O. Waldmann, and B. Ludevigt, *Rev. Sci. Instrum*. **82**, 113505, 2011.

[44] O.D. Cortázar, A. Megía-Macías, and A. Vizcaíno-de Julián, *Rev. Sci. Instrum*. **83**, 103302, 2012.

[45] C. Baumgarten, A. Barchetti, H. Einenkel, D. Goetz, and P. A. Schmelzbach, *Rev. Sci. Instrum*. **82**, 113505,2011.

[46] L. Celona et al., *Proceedings of the 20th International Conference on Cyclotrons and Their Applications 2013*, Vancouver (BC), Canada, TUPPT014, 2013.

[47] O.A. Popov, *High Density Plasma Sources Design, Physics and Performance*, p. 284. Noyes Publications, Park Ridge, NJ, 1995.

[48] C. Lyneis, J. Benitez, D. Leitner, J. Noland, M. Strohmeier, H. Koivisto, and O. Tarvainen. *Proceedings of ECRIS 2010*, Grenoble, France, p. 162-164, 2010.

[49] L. Celona, S. Gammino, G. Ciavola, F. Maimone, and D. Mascali, *Rev. Sci. Instrum*. **81**, 02A333, 2010.

[50] Shreya Nad, Yajun Gu and Jes Asmussen, *Rev. Sci. Instrum*. **86**, 074701, 2015.

[51] J.E. Stevens, J.L. Cecchi, Y.C. Huang, and R.L. Jarecki, Jr., *J. Vac. Sci. Technol*. **A 9**(3), 696-701, 1991.

[52] M. Cavenago and C. T. Iatrou, *Rev. Sci. Instrum*. **65**, 1122, 1994.

[53] C.L. Yee, A.W. Ali and W.M. Bollen, *J. Appl. Phys*. **54**, 1278, 1983.

[54] Amir Khan and Jes Asmussen, *Proceedings of the 27th IEEE International Conference on Plasma Science*, New Orleans, USA, 280, 2000.

[55] L. Celona, G. Ciavola, and S. Gammino, *Rev. Sci. Instrum*. **69** , 1113, 1998.

[56] S. Minomo, K. Kondo, Y. Yoshizako, Y. Ishida, and M. Taniguchi, *Rev. Sci. Instrum*. **63**, 2547, 1991.

[57] F. Consoli, L. Celona, G. Ciavola, S. Gammino, D. Mascali, S. Passarello, and F. Maimone, *33rd EPS Conference on Plasma Phys*, Rome, Vol. 30I, O-4.012, 2006.

[58] J. Helszajn, *Ridge Wavequides and Passive Microwave Components*, vol. 49 of IET Electromagnetic Waves. MPG Books Ltd., Bodmin, Cornwall, UK, 2000.

[59] D.M. Pozar, *Microwave Engineering*, 2nd Edition, John Wiley Sons, 1998.

[60] L. Young, *IRE Trans. Microwave Theory and Tech*. vol. **MTT-07**, 233, 1959.

[61] S.B. Cohn, *Proceedings of IRE*. vol. **35**, 783, 1947.

[62] N. Marcuvitz, *Waveguide Handbook*, vol. 10 of Massachusetts Institute of Technology Radiation Laboratory Series, McGraw-Hill, 1951.

[63] W.J.R. Hoefer, and M.L. Burton, *IEEE Trans. Microwave Theory and Tech*. vol. **MTT-30**, 2190, 1982.

[64] D.A. Frickery, *IEEE Trans. Microwave Theory and Tech*., vol. **MTT-42**, 205, 1994.

[65] ANSYS HFSS^{TM}, www.ansys.com/hfss, accessed on November 2015.

[66] F. Maimone, L. Celona, F. Ciavola, G. Consoli, S. Gammino, S. Barbarino, and L. Timino, Technical Report INFN/TC-07/04, Instituto Nazionale de Fisica Nucleare - Laboratori Nazionali del Sud, 2007.

[67] S. Gammino, L. Celona, G. Ciavola, F. Maimone, and D. Mascali, *Rev. Sci. Instrum*. **81**, 02B313, 2010.

[68] J. -M. Lagniel, P.-Y. Beauvais, D. Bogard*et al, Rev. Sci. Instrum*. **71**, 830, 2000.

[69] L. Celona, G. Ciavola, S. Gammino *et al.*, *Rev. Sci. Instrum*. **75**, 1423, 2004.

[70] R. Gobin, P.-Y. Beauvais, R. Ferdinand, P.-A. Leroy, L. Celona, G. Ciavola and S. Gammino, *Rev. Sci. Instrum*. **70**, 2652, 1999.

[71] Shixiang Peng, Pengnan Lu, Haitao Ren, Jie Zhao, Jia Chen, Yuan Xu, Zhiyu Guo, Jiaer Chen, Hongwei Zhao, and Liangting Sun, *Rev. Sci. Instrum*. **84**, 033304, 2013.

[72] A. Benismail, R. Duperrier, D. Uriot, and N. Pichoff, *Phys. Rev. ST Accel. Beams* **10**, 070101, 2007.

[73] N. Chauvin, O. Delferriere, R. Duperrier, R. Robib, P. A. P. Nghiem and D. Uriot, *Rev. Sci. Instrum*. **83**, 02B320, 2012.

[74] L. Weissman, *Rev.Sci.Instrum*, **85**, 02A710, 2014.

[75] S.M. Lund and B. Bukh, *Phys. Rev. ST Accel. Beams***7**, 064201, 2004.

[76] V.S. Pandit, P.R. Sarma, S. Bhattacharya and R. K. Bhandari, *Meas. Sci. Technol*. **8** 1085, 1997.

[77] K. Poorrezaei, R.B. Fiorito, R.A. Kishek, and B.L. Beaudoin, *Phys. Rev. ST Accel. Beams* **16**, 082801, 2013.

[78] Martin P. Stockli, *AIP Conference Proceedings* 868, pp. 25-62 , 2006.

[79] H. Zhao, Z Shen and Wei B, *Proceedings of 13th International Conference on Cyclotrons and their Applications*, Vancouver (BC), Canada, pp. 479. , 1992.

[80] F.J. Sacherer, *IEEE Trans. Nucl. Sci*. **NS-18**, 1105, 1971.

[81] M. Reiser, *Theory and Design of Charged Particle Beams*, John Wiley and Sons, New York, 1994.

[82] I. M. Kapchinsky, and V.V. Vladimirsky, *Proceedings of International Conference on High Energy Accelerators and Instrumentation*, Geneva, Switzerland, p. 274-288, 1959.